FLOW AND TRANSPORT STUDIES OF POROUS SYSTEMS BY MAGNETIC RESONANCE MICROSCOPY AND LATTICE BOLTZMANN SIMULATIONS

by

Tyler Ryan Brosten

A dissertation submitted in partial fulfillment
of the requirements for the degree

of

Doctor of Philosophy

in

Engineering

MONTANA STATE UNIVERSITY
Bozeman, Montana

January 2010

APPROVAL

of a dissertation submitted by

Tyler Ryan Brosten

This dissertation has been read by each member of the dissertation committee and has been found to be satisfactory regarding content, English usage, format, citation, bibliographic style, and consistency, and is ready for submission to the Division of Graduate Education.

Dr. Sarah L. Codd

Approved for the Department of Mechanical and Industrial Engineering

Dr. Chris Jenkins

Approved for the Division of Graduate Education

Dr. Carl A. Fox

STATEMENT OF PERMISSION TO USE

In presenting this dissertation in partial fulfillment of the requirements for a doctoral degree at Montana State University, I agree that the Library shall make it available to borrowers under rules of the Library. I further agree that copying of this dissertation is allowable only for scholarly purposes, csistent with "fair use" as prescribed in the U.S. Copyright Law. Requests for extensive copying or reproduction of this dissertation should be referred to ProQuest Information and Learning, 300 North Zeeb Road, Ann Arbor, Michigan 48106, to whom I have granted "the exclusive right to reproduce and distribute my dissertation in and from microform along with the non-exclusive right to reproduce and distribute my abstract in any format in whole or in part."

Tyler Ryan Brosten

January 2010

TABLE OF CONTENTS

TABLE OF CONTENTS-CONTINUED

TABLE OF CONTENTS-CONTINUED

LIST OF TABLES

Table Page

LIST OF FIGURES

LIST OF FIGURES-CONTINUED

Figure Page

LIST OF FIGURES-CONTINUED

Figure Page

LIST OF FIGURES-CONTINUED

Figure Page

LIST OF FIGURES-CONTINUED

Figure Page

LIST OF FIGURES-CONTINUED

Figure Page

ABSTRACT

Nuclear magnetic resonance experiments and Lattice-Boltzmann simulations are powerful techniques for studying pore scale dynamics in porous media. Several applications of these methods to the study of pore scale hydrodynamics and transport are discussed. Of special interest are concepts relating to pore structure characterization. In the first application it is shown that nuclear magnetic resonance measurements of pre-asymptotic transport dynamics in random open cell foams provide a characteristic structure length scale. These measurements and Lattice-Boltzmann simulations for a model foam structure demonstrate dynamical behavior similar to lower porosity consolidated granular porous media; suggesting a generalized approach to pore structure characterization. Normalizing the data by the characteristic length collapses data for different foam samples and mono-disperse packed beds. The non-equilibrium statistical mechanics theory of pre-asymptotic dispersion is used to model the hydrodynamic dispersive dynamics. In the second application transport of hard sphere colloidal particles under flow through an open cell foam is studied using nuclear magnetic resonance. The temporal dynamics of the colloidal particles and suspending fluid phase are obtained through spectral chemical resolution. The data is interpreted in the broader context of classic hydrodynamic dispersion theory and mechanisms of transport for each phase. In the third application pore scale hydrodynamics of flow over a model porous surface are investigated using three dimensional Lattice-Boltzmann simulations and nuclear magnetic resonance. The Lattice-Boltzmann and nuclear magnetic resonance data are used to interpret classic interfacial hydrodynamic boundary conditions. Finally, in the fourth application a study of magnetic resonance microscopy to novel tape cast porous ceramics is conducted.

INTRODUCTION

This thesis research studies flow and transport in several porous media systems using Magnetic Resonance Microscopy (MRM) experimental techniques and computational Lattice Boltzmann (LB) simulations. The media studied in this work are polymer cellular structures, tapered pore ceramics, and partially porous channels. Each of these media represent important classes of porous media that find application and occurrences in many technological and natural media; e.g. bones and filters in the case of cellular structures and river and sea-floor bottoms in the case of partially porous channels. For the former two structures, foam and tapered pore ceramics, the theme of research concerns structural characterization while questions regarding pore-scale hydrodynamics and transport will be addressed in the partially porous channel case. An additional set of results will be presented which experimentally probes the flow and transport of a hard sphere, Brownian particle colloidal suspension through the polymer cellular structure.

The practical challenges associated with experimentally observing three dimensional pore-scale transport in optically opaque porous media has historically regulated the experimental approach to classic bulk transport methods, e.g. breakthrough type curves. A significant advance over previous experimental methods is the application of nuclear magnetic resonance to the study transport processes. These developments have produced a set of techniques, known as pulsed gradient methods, which allow one to non-invasively probe the time correlation functions of single and multi-phase fluid transport in porous media. In parallel with these technological developments a computational technique based upon the discrete Boltzmann equation, the so-called Lattice Boltzmann method, allows for efficient simulation of fluid flow in domains

containing complex boundaries. These relatively new methods represent a powerful set of experimental and numerical tools which allow one to non-invasively observe fluid transport in porous media over a range of temporal and spatial scales. While these experimental and numerical techniques are quickly maturing, the significant advantages which they provide over previous approaches to observing transport in porous media affords an extensive list of potential practical applications. The majority of results contained within this thesis is orientated toward the practical application of MRM and LB simulations to addressing questions of scientific and engineering interest in porous media, rather than advancing the techniques themselves.

The following thesis is organized as follows, chapters one through three will provide an overview of the nuclear magnetic resonance phenomenon and experimental technique, the lattice Boltzmann method, and an overview of transport in porous media theory. Chapters four through six will discuss the experimental and numerical results from studies on the polymer cellular structures, tapered pore ceramics, and partially porous channels, respectively. Chapter four will also discuss results from the study of flow and transport of a colloidal suspension through the polymer cellular structures. Chapters four through six are organized in a manner similar to standalone research documents with an introduction and theory section, discussion of results, and conclusion section. Chapter seven will summarize the primary results of this work with concluding remarks.

MAGNETIC RESONANCE MICROSCOPY

Magnetic resonance microscopy is a suite of experimental methods which manipulate and observe the nuclear magnetic resonance phenomenon. These techniques allow for a range of information to be collected from a sample including chemical [1-3], spatial [4], and dynamic [5, 6]; to name but a few. Nuclear magnetic resonance is an encompassing term which refers to the intrinsic magnetic moment behavior of a nucleus's protons in the presence of electromagnetic fields. The scope and complexity of this phenomenon, which is inherently quantum mechanical, is too large to provide a comprehensive discussion in this work, the reader is referred elsewhere for a more detailed quantum mechanical oriented discussion [7]. The following will instead focus upon the semi-classical ensemble average or macroscopic behavior of the nuclear magnetic resonance phenomenon.

Fundamental Concepts of Magnetic Resonance Microscopy

Spin and the Zeeman Interaction

Atomic nuclei are known to possess an intrinsic property known as spin or spin quantum number. The discrete value of spin, I, which can be either integer or half integer values, quantifies the number of energy or basis states available to atomic nuclei. The number of energy states available to a nucleus is governed by the relation $2I+1$; which produces a range of states from $-I, -I+1,\ldots,I-1,I$. This work is concerned strictly with spin $I = ½$ nuclei so that only two energy states are available, the so-called spin-up and spin-down states. Furthermore, the following discussion will focus generally upon a spin system in the liquid state. In addition to the property of spin, atomic nuclei also possess an intrinsic magnetic dipole moment, $\boldsymbol{\mu}$. In the

presence of a large external magnetic field the dipole moment of a spin ½ nuclei can occupy, e.g. align with, the two available energy states according to the Boltzmann probability distribution [8]

$$N_{-}/N_{+} = \exp\left(-\gamma \hbar B_o / kT\right) \qquad (2.1).$$

Where N_- and N_+ are the populations of an ensemble of spins in the lower, spin down, and upper spin up states, γ is the gyromagnetic ratio, B_o is the magnitude of an applied magnetic field, $\hbar$ is Planck's constant, k is the Boltzmann constant, and T is the temperature. The numeric disparity of spin populations in Eqn. (2.1) governs the polarization which develops for a population of spins in the presence of an applied magnetic field.

The interaction energy of spins in the presence of an applied magnetic field is given by the Zeeman Hamiltonian [6]

$$H = -\gamma \hbar I_z B_o \qquad (2.2).$$

Where I_z is an operator for the angular momentum acting in the direction of the applied magnetic field, typically along the z-axis. It is important to note the energy separation for the spin states is independent of the spin quantum number. The Zeeman interaction given by Eqn. (2.2) can be interpreted as an applied torque to the magnetic dipole. Using the Schrödinger equation, the formal solution to the time evolution of the spin state given in Eqn. (2.2) produces an evolution operator, $U(t) = \exp(i\gamma B_o I_z t)$. This evolution operator is equivalent to rotation of the magnetic moment about the B_o axis at the rate

$$\omega_o = \gamma B_o \qquad (2.3).$$

Where ω_o is known as the Larmor frequency. For protons γ is equivalent to 2.675 x 10^8 rad s^{-1} T^{-1}. For an ensemble of spins N is typically on the order of Avogadro's number and as such the collective evolution of the spin population in the presence of an applied magnetic field can be treated as net polarization often written as **M**. In the presence of a static magnetic field the net polarization, **M**, is also a static magnetic field with a single component aligned parallel with the applied magnetic field. Nuclear magnetic resonance experiments use the ensemble polarization as the experimental observable. The two key phenomenon which make NMR experiments possible are the polarization given by the Boltzmann distribution, Eqn. (2.1), and magnetic moment precession given by the Larmor frequency, Eqn. (2.3).

The Torrey-Bloch Equation

In the presence of a large external magnetic field spin ½ nuclei develop a net magnetic polarization with an angular momentum given by **M**/γ. The net magnetization evolution is given by the semi-classical Torrey-Bloch equation [6, 9, 10] which relates the angular momentum of net magnetization to the torque created by the applied magnetic field

$$\dot{\mathbf{M}} = \gamma \mathbf{M} \times \mathbf{B} + v\mathbf{M} + \mathsf{R}\,\mathbf{M} \qquad (2.4).$$

In Eqn. (2.4) **B** is the applied magnetic field. The first term on the right hand side of Eqn. (2.4) is the rate of magnetization change due to the torque from the applied magnetic field. The operator v in Eqn. (2.4) represents convection-diffusion of the magnetization, this can be described in terms of classical transport theory because net magnetization is a conserved quantity [10]. The operator v is

$$v = \mathrm{D}_m \nabla^2 \text{ - } \mathbf{v} \cdot \nabla \qquad (2.5).$$

Where **v** is the local ensemble flow speed vector and D_m is the molecular diffusion coefficient. The operator R in Eqn. (2.4) generalizes relaxation and will be discussed later in the text. Additional terms can be added to Eqn. (2.4) to describe such phenomenon as radiation damping and dipolar field, the reader is referred to other works for a description of these important additions [1, 11].

Boundary conditions for Eqn. (2.4) vary according to the local electromagnetic environment at the domain surface. A general feature of the boundary conditions is that the phenomenological expression is one that describes a decoherence or loss of net magnetization at the domain boundary. This magnetization loss is governed by the electromagnetic coupling of the surface and near surface spins. Fluid molecules making up the domain must migrate very close to the surface via Brownian motion for this coupling to occur. An often used boundary condition for the local net magnetization is [12]

$$\dot{\mathbf{M}} = \mathrm{D_m}\nabla^2\mathbf{M} \qquad (2.6)$$

$$\mathbf{n}\cdot\nabla\mathbf{M} = -\frac{\mathrm{r}}{\mathrm{D_m}}\mathbf{M}\Big|_{\sum} \qquad (2.7).$$

Where r is the surface relaxivity (units of length/time) and **n** is the outward normal vector from the surface $\sum$. In this model the rate of magnetization loss at the surface is linearly proportional to the surface relaxivity and magnetization magnitude at the surface.

Excitation and the Rotating Frame of Reference

Nuclear magnetic resonance experiments are governed by the applied magnetic field, **B**, in Eqn. (2.4). The applied field is composed of a large stationary magnetic field (the polarizing

field), a time dependent radio-frequency "r.f." pulse and a spatially and temporally varying magnetic field

$$\mathbf{B} = \mathbf{B}_1(t) + \mathbf{G}(\mathbf{r},t) + B_o\mathbf{k} \qquad (2.8).$$

The unit vector **k** in Eqn. (2.8) is along the direction of the polarizing field, throughout this work it will be referred to as the longitudinal direction. In Eqn. (2.8) **G** is an applied magnetic field used in imaging and measurements of molecular dynamics; it will be neglected in this section. The radio frequency pulse in Eqn. (2.8), $\mathbf{B_1}$, is a linearly polarized field applied in the transverse plane. The solution to Eqn. (2.8), with null operators, and only the single field, $B_o\mathbf{k}$, is precession of **M** about **k** at the rate ω_o. The beginning of an NMR experiment is a state of thermal equilibrium in which the net magnetization is aligned with the longitudinal direction. The term excitation refers to perturbation of the net magnetization from thermal equilibrium via the application of $\mathbf{B_1}$ in Eqn. (2.8). This perturbation results in a temporally varying net magnetization; this is the observable in an NMR experiment. The following discussion will outline the excitation process using a semi-classical approach.

The linearly polarized field in Eqn. (2.8) can be decomposed into two circularly polarized counter-rotating fields [6]. One of these fields rotates with the same orientation as the polarized nuclear spins and therefore governs the spin interaction. The other field is negligible for a spin Hamiltonian dominated by the polarizing field, e.g. $|\mathbf{B_1}| << B_o$. The circularly polarized field is

$$\mathbf{B_1} = B_1 e^{i\omega t} \qquad (2.9).$$

Where B_1 is the half amplitude of the linearly polarized magnetic field. The resonance phenomenon occurs for $\omega = \omega_o$. For this special case the apparent applied magnetization, as viewed from a frame of reference moving with the rotating net magnetization, is entirely due to

the applied magnetization given by Eqn. (2.9). With the initial condition that defines thermal equilibrium $\mathbf{M} = M_o\mathbf{k}$, the solution to Eqn. (2.4) is [6]

$$\mathbf{M}/M_o = \left(\sin\gamma|\mathbf{B_1}|t\right)e^{i\omega_o t} + \cos\gamma|\mathbf{B_1}|t\,\mathbf{k} \qquad (2.10).$$

For the case of resonance the effect of applying the field $\mathbf{B_1}$ is to rotate the net magnetization into the transverse plane at the rate $|\mathbf{B_1}|\gamma t$, at the same time the field rotates around the longitudinal axis at the rate ω_o. The net magnetization is thus perturbed from thermal equilibrium, this defines excitation. Equation (2.10) is for the case of resonance, a discussion of off-resonance behavior is given in the next section. Rotation of the net magnetization around the longitudinal axis provides a mechanism for signal detection, as will be discussed later in the text. During the excitation process the applied magnetic field, $\mathbf{B_1}$, dominates the local electromagnetic environment. The spins are thus decoupled from another and their surrounding environment and as a result the spin phases are all equivalent. After the field is removed the local electromagnetic environment acts to return the system to thermal equilibrium and "de-phase" the spin population, e.g. increase the system entropy. These processes are known as relaxation.

Relaxation

Relaxation is an encompassing term for the electromagnetic pairing of individual spins and with the surrounding environment. These effects act on individual nuclei dipoles, however for the many-body problem, e.g. a fluid, a stochastic or continuum treatment of relaxation is necessary [13, 14]. The broad range of mechanisms altering the local electromagnetic environment of nuclei contributes to two subcategorizes of up-scaled relaxation: transverse and longitudinal relaxation. Transverse relaxation refers to effects that act to dephase the net

magnetization in the transverse plane while longitudinal relaxation refers to effects which act to return the spin system to thermal equilibrium. These will be summarized in the following narrow discussion of dipolar relaxation, for a more comprehensive discussion of relaxation the reader is referred to other work [6, 15].

Transverse Relaxation: The molecules of a fluid are constantly in rotational and translational motion. This motion leads to a local time varying electromagnetic environment or equivalently a varying spin system Hamiltonian. For spin ½ nuclei the dominant mechanism of spin coupling is the dipolar interaction whereby spins interact locally through their dipolar moments [6, 8]. This interaction is quantified by the spectral density function

$$J(\omega) = \int_{-\infty}^{\infty} h(0)h(t)e^{i\omega t}\,dt \qquad (2.11).$$

Where J is the spectral density function and h is the local magnetic field along a Cartesian direction. The original theory of relaxation developed by Bloembergen, Purcell, and Pound relates the spectral density function evaluated at multiples of the Larmor frequency and spatial components to phenomenological constants governing relaxation [6, 14, 16]. There are two limits of motion for the interaction of dipoles given by Eqn. (2.11). In the fast motion limit the characteristic time scale of decay for the correlation function in Eqn. (2.11), τ_c, is significantly greater than the 'precession period in the dipolar field' [13]; e.g. $\tau_c^{-1} >> \omega_o$. In this limit and when the sequence of interactions given by Eqn. (2.11) forms a random process, e.g. $h(0)h(t)$ decays exponentially with time, then the decay of transverse magnetization is written as

$$(\dot{\mathbf{M}}\cdot\mathbf{i})\mathbf{i} + (\dot{\mathbf{M}}\cdot\mathbf{j})\mathbf{j} = -[(\mathbf{M}\cdot\mathbf{i})\mathbf{i} + (\mathbf{M}\cdot\mathbf{j})\mathbf{j}]/T_2 \quad (2.12).$$

Where T_2 is the transverse relaxation time constant. The decay of magnetization given by Eqn. (2.12) thus forms an exponential process in time; this is the classical description of transverse relaxation or 'spin-spin' relaxation.

In addition to dipolar interactions of individual nuclei there are other mechanisms which contribute to the spin system T_2 value. A simple representation of these mechanisms is [8]

$$\frac{1}{T_2} = \left(\frac{1}{T_2}\right)_S + \frac{1}{T_2^*} + \left(\frac{1}{T_2}\right)_B \qquad (2.13).$$

Where $(1/T_2)_S$ is the contribution from interaction of dipoles with the domain surface, $1/T_2^*$ is the contribution from diffusion within local magnetic field homogeneities, and $\left(1/T_2\right)_B$ is the bulk contribution from molecular tumbling. The diffusion contribution in Eqn. (2.13) is a reversible magnetization decay, as will be shown later in the text. The other mechanisms are irreversible magnetization losses. By its very nature Eqn. (2.13) suggests multi-exponential decay. The single exponential nature of magnetization decay given by Eqns. (2.12) and (2.13) is only valid when a single mechanism dominates. Equation (2.13) is only meant to illustrate the potential for various mechanisms which contribute to transverse relaxation. A generalized form of relaxation using a distribution of relaxation times must be used to model multi-exponential dynamics.

Longitudinal Relaxation: Excitation can be interpreted as perturbing the spin system from thermal equilibrium with the surrounding environment. Longitudinal relaxation refers to the exchange of energy between the spin system and the surrounding environment following excitation: 'spin-lattice relaxation'. From a continuum perspective this exchange of energy acts to return the net magnetic vector to the longitudinal axis. On a quantum level the energy

exchange is a stimulated transition of the spin ½ nuclei between the spin-up and spin-down states. These transitions release energy in the form of photons. The theoretical treatment of longitudinal relaxation is handled by the Bloembergen, Purcell, and Pound theory and alternatively by the density matrix formalism. Equivalent to transverse relaxation, in the fast motion limit decay of longitudinal relaxation can be written as

$$\dot{\mathbf{M}}\cdot\mathbf{k} = \left(\mathrm{M_o} - \mathbf{M}\cdot\mathbf{k}\right)/\mathrm{T_1} \qquad (2.14).$$

Where T_1 is the longitudinal relaxation constant. Similar to T_2 a number of effects, such as surface boundary effects, contribute to the value of T_1. In the fast motion limit the longitudinal and transverse relaxation have unique values with $T_1 > T_2$. For liquids the dominant mechanism of relaxation is a result of thermal motion, therefore both relaxation constants are sensitive to the sample temperature. Furthermore, the relaxation values are governed in part by the strength of dipolar interacts or energy separation of the spin states and therefore are sensitive to the polarizing field strength. This concludes the discussion of relaxation. An introductory treatment was presented for the fast motion limit of liquids and spin ½ nuclei. In conclusion we may now write the operator in Eqn. (2.4) as

$$\mathrm{R} = -\left[\left(\mathbf{i}\cdot/\mathrm{T_2}\right)\mathbf{i} + \left(\mathbf{j}\cdot/\mathrm{T_2}\right)\mathbf{j} - \mathrm{M_o}\left(\mathbf{k}\cdot/\mathrm{T_1}\right)\mathbf{k}\right] \qquad (2.15).$$

Signal Detection

Precession of the net magnetic vector about the longitudinal axis is the mechanism through which information is collected about the spin system. Through Faraday's law this rotating magnetic field will induce an oscillatory electric current in a surrounding conductive coil which has the symmetry axis transverse to the polarizing field. The signal collected in this

way is a bulk transverse signal arising from the superposition of all net magnetic vectors within the sample [6]

$$\mathbf{M}_{+} = \mathrm{M}_{o} \int_{-\infty}^{\infty} \mathrm{P}(\omega) \mathrm{e}^{\mathbf{i}\omega\mathbf{t}} \exp^{-t/T_2} \mathrm{d}\omega \qquad (2.16).$$

Where $\mathbf{M}_{+}$ is the total complex magnetization in the transverse plane per unit volume and $P(\omega)$ is the probability distribution of frequencies within the sample. Equation (2.16) is a Fourier relationship for $P(\omega)$ and therefore upon inverse Fourier transform of the complex signal yields the amplitude and phase of the frequency distribution in the sample. The distribution of frequencies can contain a variety of information about the sample including chemical, structural, and molecular dynamics. An important point concerning Eqn. (2.16) is that the temporal electromagnetic environment which causes transverse relaxation is also responsible for a "broadening" of the signal frequency distribution; *e.g.* the frequency distribution $P(\omega)$ appears broader than the single Larmor frequency distribution: $P(\omega) = \delta(\omega-\omega_o)$. For relaxation dynamics governed by a single exponential, as suggested by Eqn. (2.16), broadening of the frequency distribution is Lorentzian [13]. Spatial manipulation of the frequency ω by application of **G** in Eqn. (2.8) is the basis for imaging and molecular dynamic measurements in NMR. These techniques are discussed in the next section.

Experimental Methods

The governing equation of the net magnetic vector evolution given by Eqn. (2.4) is an indication of the potential bulk NMR signal information content. Experimental methods in NMR encode sample information through application of r.f. and magnetic field gradient time

sequences and then extract the desired information from the observed bulk signal. These techniques are roughly grouped into two categories: chemical NMR and imaging and transport measurements. Chemical NMR methods utilize free spin precession and relaxation dynamics to extract chemical information at an atomic and molecular scale. Before measuring free spin precession chemical NMR methods apply a series of r.f. and gradient pulses to prepare the signal with the desired information. Imaging and transport measurements apply a series of r.f. and magnetic field gradient pulses to encode the NMR signal with spatial and/or molecular dynamic information for the purpose of observing phenomenon occurring on the continuum scale. The following discussion outlines imaging and transport measurements. The methods of spin echo, selective excitation, imaging, transport, and relaxation are reviewed.

The Spin Echo

In the previous section discussing signal relaxation T_2^* was said to be reversible. The technique used to exploit this reversibility is known as the spin echo [17]. In the presence of macroscopic magnetic field homogeneities $P(\omega)$ in Eqn. (2.16) is a broadened distribution relative to the intrinsic chemical line width

$$\omega = \omega_o + \gamma\left(\mathbf{G} + \mathbf{G}^*\right)\cdot\mathbf{r} \qquad (2.17)$$

$$P(\omega) = \frac{1}{V}\int_V \rho(\mathbf{r})\,\omega(\mathbf{r})\,d\mathbf{r} \qquad (2.18).$$

Where **G*** in Eqn. (2.17) is the magnetic field homogeneity, V in Eqn. (2.18) is the sample volume and ρ is the spin density at **r**. Over a time τ the phase acquired by a differential element of net magnetic vector due to the magnetic field homogeneity will be

$$\phi^*(t,\mathbf{r}) = \gamma t \mathbf{G}^* \cdot \mathbf{r} \qquad (2.19).$$

The decrease in bulk signal amplitude from this homogeneity is given by

$$\left|\mathbf{M}^*\right\|_\tau = \left|\mathbf{M}_+^*\right|\left(1 - \int_0^\tau \int_{-\infty}^{\infty} P(\phi^*)\cos(\phi^*)\,d\phi^*\,dt\right) \qquad (2.20)$$

Where $P(\phi^*)$ is the probability of phase, ϕ^*, in volume V after time τ. If one is able to 'invert' the relative precession of net magnetic vectors at time τ then the amplitude modulation from the magnetic field homogeneity at time 2τ will be null

$$\left|\mathbf{M}^*\right\|_{2\tau} = \left|\mathbf{M}^*\right\|_t - \left|\mathbf{M}_+^*\right|\left(1 - \int_{-\infty}^{\infty} \int_{\tau}^{2\tau} P(\phi^*)\cos(\phi^*)\,d\phi^*\,dt\right) = 0 \,(2.21).$$

The inversion of relative precession from magnetic field homogeneity forms the basis of spin echoes. In this technique the relative precession of the net magnetic vectors in a magnetic homogeneity field is inverted by applying a $\mathbf{B_1}$ field which rotates the net magnetic vector 180° about the rotating frame axis. This sequence is written schematically as

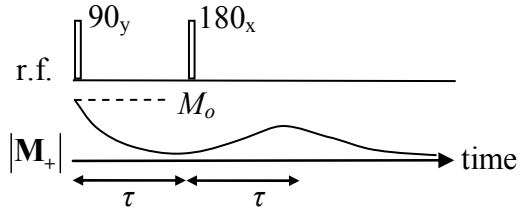

Figure 1: The spin echo pulse sequence schematic

With the application of a 180° single valued r.f. pulse, shifted in phase 90° from the initial excitation pulse, at time τ the transverse signal amplitude returns to nearly its initial amplitude

after time 2τ. There is a non-zero component of signal attenuation at time 2τ from irreversible relaxation and molecular diffusion within the magnetic field homogeneities. A variation of the spin echo sequence is the stimulated echo sequence [18] shown schematically in Figure 2.

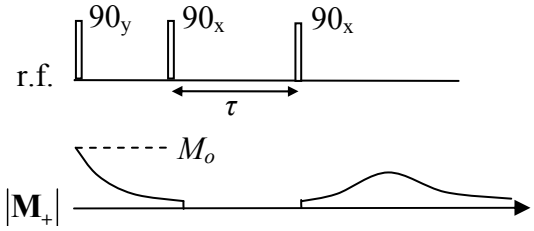

Figure 2: The stimulated echo pulse sequence schematic

In the stimulated echo sequence the sample magnetization is rotated into the longitudinal axis and stored for a time τ. Because transverse relaxation does not occur during the storage time, this sequence can greatly extend the observation time of experiments.

Selective Excitation

In the previous section it was shown how application of an oscillatory r.f. pulse at the Larmor frequency will rotate the net magnetic vector into the transverse plane at the rate $|\mathbf{B_1}|\gamma t$. Often within a sample there exists a range of Larmor frequencies due to unintentional magnetic field homogeneities, the chemical environment, or applied magnetic fields. For the off-resonance case in which $\omega \neq \omega_o$, where ω_o is the frequency of the $\mathbf{B_1}$ field, the applied magnetic field relative to the net magnetic vector will have an additional component along the longitudinal axis with a magnitude $\Delta\omega/\gamma$; where $\Delta\omega$ is the frequency difference between the local Larmor frequency and $\mathbf{B_1}$. Therefore, in the off-resonance case the local net magnetic vector is partially rotated into the transverse plane and contributes less to the bulk NMR signal magnitude relative

to a local magnetic vector in resonance. For local Larmor frequencies within the bandwidth of the single frequency r.f. pulse, $1/T$ where T is the r.f. pulse duration, the apparent applied net magnetic field is entirely along the transverse plane. The ability to adjust the pulse duration of the single valued r.f. pulse allows one to control the range of frequencies rotated into the transverse plane. This process of 'selecting' the range of frequencies rotated into the transverse plane is termed selective excitation [19]. The term *hard pulse* refers to the use of a single valued r.f. pulse magnitude and *soft pulse* refers to the use of a temporally varying r.f. pulse magnitude sometimes in conjunction with an applied magnetic field.

Formal solution to the transverse magnetization evolution for the off-resonance case with small tip angles is [20, 21]

$$\mathbf{M}_{+}(\mathbf{r},t) = i\gamma M_o e^{-iT\Delta\omega(\mathbf{r})} \int_{-T}^{T} \mathbf{B_1}(t) e^{it\Delta\omega(\mathbf{r})}\, dt \qquad (2.22)$$

Equation (2.22) is an important relationship because it demonstrates how the range of excited frequencies is given by the frequency distribution of the $\mathbf{B_1}$ pulse. One can design the desired frequency distribution by 'shaping' the temporal r.f. pulse function; e.g. if one requires a square or hat function of frequencies, then the r.f. pulse must be a sinc-function in time.

The ability to control the frequency offset, $\Delta\omega$, by applying magnetic field gradients allows one to excite a spatial region within a sample, termed *slice selection* [4, 22]. For a linear magnetic field gradient, $\mathbf{G}$ in Eqn. (2.17) and the offset frequency become

$$\mathbf{G} = G_x \mathbf{i} + G_y \mathbf{j} + G_z \mathbf{k} \qquad (2.23)$$

$$\Delta\omega(\mathbf{r}) = \gamma \mathbf{G}\cdot\mathbf{r} = \omega\big|_{\mathbf{G}^*=0} - \omega_o \mathbf{k} \qquad (2.24).$$

Inspection of Eqn. (2.22) shows that application of the linear magnetic field gradient given by Eqn. (2.23) over time $2T$ dephases the local signal relative to Larmor precession by an angle $T\Delta\omega$. This reversible dephasing can be recovered by application of a negative gradient of equal amplitude for a time T. For a single gradient component along the longitudinal axis the pulse sequence schematic used to excite a hat function of frequencies and recover the reversible dephasing is shown schematically in Figure 3. The slice direction in Figure 3 is equivalent to the longitudinal axis.

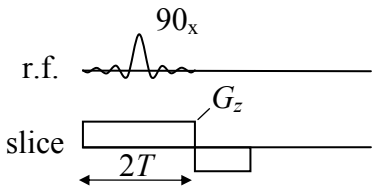

Figure 3: The slice selection pulse sequence schematic

The one dimensional slice selection sequence shown in Figure 3 is a common *preparation* of the signal for imaging and other post-preparation measurements. In most chemical NMR and some dynamic measurements one typically uses a hard pulse for signal preparation.

Imaging Methods

Imaging refers to measurement of the continuum spin density distribution, $\rho(\mathbf{r})$; where ρ is the number of discrete spins within a differential volume element of arbitrary units. In Eqn. (2.16) it was shown that the bulk NMR signal and the distribution of frequencies making up that signal share a Fourier relationship. Furthermore in Eqn. (2.24) it was shown that one can control the spatial distribution of frequencies by application of a magnetic field gradient. Therefore,

following preparation and during a linear one-dimensional magnetic field gradient the bulk signal can be written as

$$\mathbf{S}(t) = \int_V \rho(\mathbf{r}) e^{i\gamma \mathbf{G}\cdot\mathbf{r}t}\, d\mathbf{r} \qquad (2.25)$$

$$\mathbf{S}(\mathbf{k}) = \int_V \rho(\mathbf{r}) e^{i2\pi\gamma \mathbf{k}\cdot\mathbf{r}}\, d\mathbf{r} \qquad (2.26).$$

The three dimensional spatial frequency variable is $\mathbf{k} = (2\pi)^{-1}\gamma\mathbf{G}t$ [4, 22, 23]. Relaxation is neglected in Eqns. (2.25) and (2.26) because it is assumed the time scale of relaxation, *e.g.* T_2, is significantly less than the duration of **G**. Equation (2.26) is a Fourier relationship between the spin density $\rho(\mathbf{r})$ and the bulk signal. Therefore, one can determine the spin density or sample 'image' upon inverse Fourier transform of the bulk signal obtained as a function of **k**. The two-dimensional acquisition of the signal is conveniently represented by a '**k**-space' raster as shown in Figure 4. The **k**-space raster is a complex valued and discrete data set.

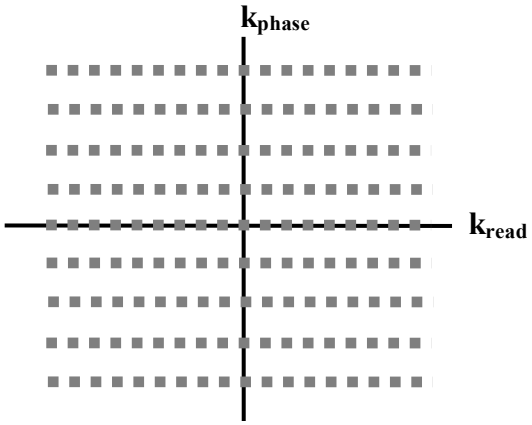

Figure 4: Two dimensional **k**-space raster with discrete acquisition points

The vast array of two dimensional spin density imaging sequences accomplish the task of filling out the amplitudes of the complex **k**-space raster shown in Figure 4. The methodology can vary greatly depending upon the desired acquisition speed, accuracy or signal to noise ratio, and hardware limitations. The raster in Figure 4 is shown in discrete points because of the digital nature of the sampling that occurs during signal acquisition, this will be discussed later in the practical considerations section below.

A common two dimensional imaging method is the spin warp imaging technique [24] shown in Figure 5.

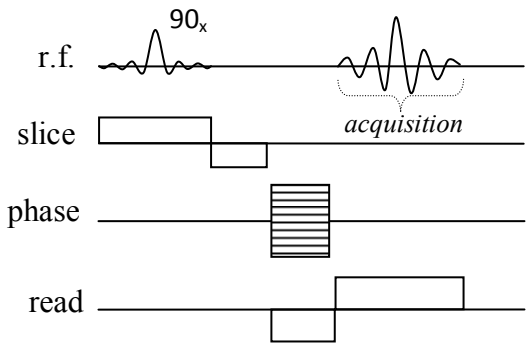

Figure 5: Two dimensional spin-warp imaging sequence schematic with slice preparation

In the spin-warp sequence signal acquisition occurs during the application of the read direction gradient. The phase encoding gradient is stepped in discrete intervals. The spin-warp sequence fills the **k**-space raster as shown in Figure 6.

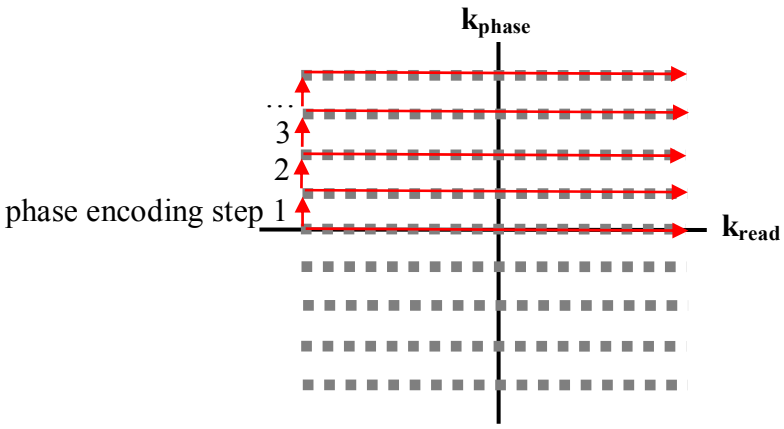

Figure 6: Spin-warp imaging **k**-space acquisition

The spin-warp imaging sequence will be used throughout this work in various two-dimensional images. This concludes a brief discussion of imaging. A basic treatment is given by the introduction of the Fourier relationship between the spin density, $\rho(\mathbf{r})$, and bulk transverse NMR signal during applied linear magnetic field gradients.

Relaxation Methods

Relaxation methods measure the magnetization decay rates in the transverse and longitudinal directions, *e.g.* T_1 and T_2. These decay rates provide chemical and structural sample information. The following discussion outlines classic approaches to measuring the longitudinal and transverse relaxation rates. As mentioned in the relaxation theory section while the net magnetization is aligned with the longitudinal axis, signal attenuation is due entirely to longitudinal relaxation. This principle forms the basis of the inversion recovery sequence [25] used to measure the longitudinal relaxation rate, shown in Figure 7.

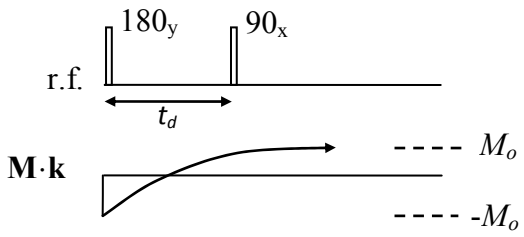

Figure 7: Inversion recovery sequence schematic

In the inversion recovery sequence magnetization is initially stored along the negative longitudinal axis. After a period of time, t_d, magnetization is rotated into the transverse plane and the signal amplitude is measured. Decay of signal amplitude following the 90º pulse in Figure 7 will occur according to the generalized relationship[26]

$$\left|\mathbf{M}_{+}\right| = \mathrm{M_o}\left[1 - 2\int_0^{\infty} \mathrm{P}\left(\mathrm{T_i}\right) e^{-\mathrm{t}/\mathrm{T_I}}\, \mathrm{dT_I}\right] \qquad (2.27).$$

Where $P(T_i)$ is the probability distribution of longitudinal relaxation rates. The expression is a Laplace relationship between the signal and relaxation distribution, therefore inverse Laplace transform of the NMR signal will yield the distribution of decay rates. For the single relaxation rate given by Eqn. (2.14) the relaxation distribution is $P(T_i) = \delta(T_i - T_1)$. The transverse relaxation rate is measured by the CPMG (Carr, Purcell, Meiboom, Gill) sequence [27], see Figure 8.

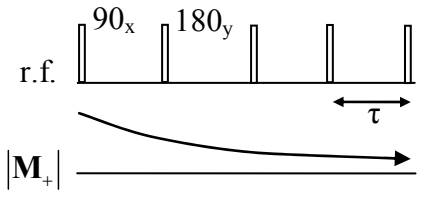

Figure 8: CPMG sequence schematic

In the CPMG sequence the net magnetization is rotated in the transverse plane and then recorded at increments of τ. The series of 180º pulses are used to marginalize reversible relaxation loss. The transverse signal amplitude decay is

$$\left|\mathbf{M}_{+}\right| = \mathrm{M}_{\mathrm{o}} \int_{0}^{\infty} \mathrm{P}\left(\mathrm{T}_{2}\right) e^{-\mathrm{t}/\mathrm{T}_{2}} \, \mathrm{d}\mathrm{T}_{2} \qquad (2.28).$$

Where the decay rate is generalized by a probability distribution. Inverse Laplace transform of Eqn. (2.28) yields the distribution of decay rates, $P(T_2)$.

In this section two methods were introduced to measure the longitudinal and transverse relaxation rates. There are many variants to these methods including coupling with imaging sequences and expansion into two dimensional domains [28, 29].

Transport Measurement Techniques – the Pulsed Gradient Method

Before introducing NMR transport measurements a brief discussion of stochastic variables appearing in the measurements is necessary. The translational motion of an individual molecule in a population is characterized by the time dependent position vector, $\boldsymbol{r}_i(t)$. For an ensemble of molecules it is not practical to resolve the position vector for every molecule. Instead, quantitative analysis of molecular dynamics typically reverts to course grained stochastic particle tracking variables. Amongst these variables, the van-Hove self correlation function [30], P(**r**|**r**′,t), is the probability distribution of molecular displacement from **r** to **r**′ in the time *t*. The average propagator is given by a volumetric average of the van-Hove self correlation function

$$\overline{P_s}(\mathbf{R},t)=\int_V P_s(\mathbf{r}\,|\,\mathbf{r}+\mathbf{R})\rho(\mathbf{r})\,d\mathbf{r} \qquad (2.29).$$

The value of NMR transport measurements lies in the ability to directly measure the average propagator [5, 6] given by Eqn. (2.29) and also higher order correlation functions [29].

In the imaging section it was shown that application of a linear magnetic field gradient spatially localizes evolution of the net magnetic vector phase. This spatial localization of the magnetization phase is the basis of NMR transport measurements. The standard narrow pulse bipolar gradient method encodes the NMR signal with spatial displacement information by applying two short gradient pulses of opposite sense separated by an observation time of Δ, see Figure 9.

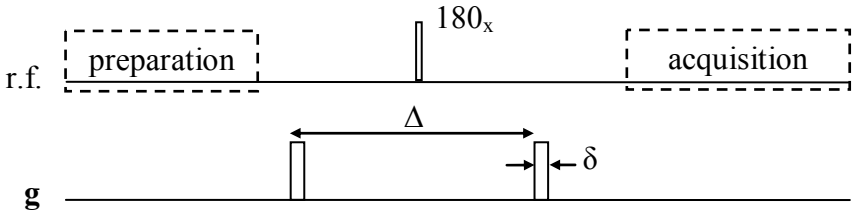

Figure 9: The pulse gradient spin echo (PGSE) sequence schematic

The boxes in Figure 9 denote arbitrary preparation or acquisition modules; e.g. hard or soft pulse preparation, spatial or spectral signal acquisition. For the case of spectral acquisition, the signal at the acquisition point is given by

$$\mathbf{S}(\mathbf{q})=\left\langle e^{i2\pi\mathbf{q}\cdot\mathbf{R}}\right\rangle=\int \overline{P_s}(\mathbf{R},\Delta)e^{i2\pi\mathbf{q}\cdot\mathbf{R}}\,d\mathbf{R} \qquad (2.30).$$

Where the displacement frequency variable is $\mathbf{q} = \gamma\delta\mathbf{g}(2\pi)^{-1}$. The NMR signal and average propagator in Eqn. (2.30) share a Fourier relationship and therefore inverse Fourier transform of the signal acquired as a function of the displacement frequency variable yields the average

propagator. From the formalism of stochastic processes [31], Eqn. (2.30) demonstrates the signal to be the characteristic function of the displacement variable **R**. A low **q** cumulant expansion [32] of Eqn. (2.30) therefore relates the moments of the volume average propagator to the magnitude and phase of the signal

$$\ln\left\langle e^{i2\pi\mathbf{q}\cdot\mathbf{R}}\right\rangle = \sum_{j=1}^{\infty}\frac{\left(i2\pi\mathbf{q}\right)^{j}}{j!}\mathbf{X}_{j} \qquad (2.31).$$

Where $\mathbf{X}_j$ is the j^{th} displacement cumulant of the average propagator. To fourth order the phase and magnitude of the signal are given by [33]: $\phi = \langle\zeta\rangle 2\pi\mathbf{q} - 1/6\,\gamma^3\left(2\pi\mathbf{q}\right)^3$ and $\ln|\mathbf{S}| = -1/2\,\sigma^2\left(2\pi\mathbf{q}\right)^2$. Where $\langle\zeta\rangle$, σ^2, and γ^3 are the first, second, and third moments of the average propagator. At low **q** the first moment governs phase modulation. The average velocity of the molecular ensemble over time Δ is given by <**v**> = $\langle\boldsymbol{\zeta}\rangle/\Delta$. A course grained version of the Eularian velocity field can be measured by a low **q** acquisition of the PGSE signal coupled with addition of an imaging module to the sequence given in Figure 9. An effective dispersion coefficient of the ensemble dynamics is given by **D** = $\boldsymbol{\sigma}^2/(\Delta-\delta/3)$. The δ/3 correction is the finite pulse correction of the PGSE origin due to Stejskal and Tanner [5].

Acquisition of the PGSE signal in the spectral domain, e.g. free precession, allows one to allocate the dynamics to chemical species [34]. This methodology will be employed in chapter four to allocate multi-phase fluid dynamics. The observation time in the PGSE experiment is limited by transverse relaxation; typically less than fifty milliseconds for practical experiment times with liquid water in a 300 MHz field. To extend the limit of observation time the

stimulated echo can be used to allow observation times on the order of the longitudinal relaxation time, T_1, typically on the order of one second.

Among the many variations of the PGSE method this work will also employ the refocused PGSE sequence [35], see Figure 10. In this sequence a second pair of gradients (separated from the first pair by mixing time τ_m) are applied with opposite sense relative to the first pair.

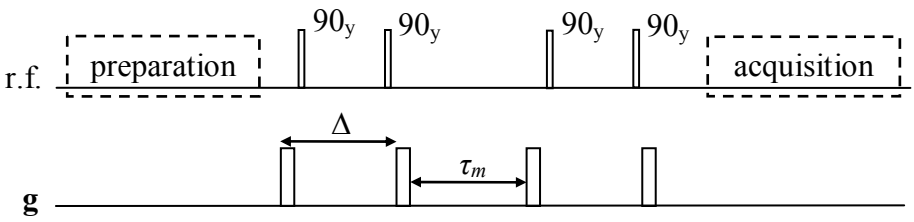

Figure 10: The refocused pulse gradient sequence with stimulated echo

During acquisition the NMR signal of the refocused gradient sequence is [35]

$$\mathbf{S}(\mathbf{q}) = \int\int\int\int \overline{P_s}(\mathbf{R_1}, \Delta)\overline{P_s}(\mathbf{R_1}|\mathbf{R_2}, \tau_m) e^{i2\pi\mathbf{q}\cdot(\mathbf{R_1}-\mathbf{R_2})}\, d\mathbf{R_1} d\mathbf{R_2} \quad (2.32).$$

Where the subscripts 1 and 2 refer to displacement occurring between the first and second gradient pairs. For stationary motion occurring over the entire experiment inspection of Eqn. (2.32) shows that there is a null net phase shift and hence zero average displacement for the refocused PGSE sequence. The ensemble magnetization phase is 'refocused' following application of the second gradient pair. The effective dispersion coefficient of the refocused PGSE experiment is [35]

$$\begin{aligned} D_{eff}(\Delta) &= (\Delta/6)\left[\left\langle \mathbf{v}(\mathbf{R})^2 \right\rangle - \left\langle \mathbf{v}(0)\mathbf{v}(\mathbf{R}) \right\rangle\right] \qquad \Delta \ll \tau_m \\ D_{eff}(2\Delta) &= D(2\Delta) - 1/\Delta \left\langle \mathbf{R}_1 \mathbf{R}_2 \right\rangle \qquad \Delta \gg \tau_m \end{aligned} \quad (2.33).$$

Two cases are given in Eqn. (2.33) for the observation time relative to the mixing time. In the first case **R** is the total displacement at the experiment end. In the second case *D* is the effective dispersion coefficient from the single PGSE experiment. A comparison of the single PGSE experiment and the second case of the refocused PGSE experiment therefore provides an indirect measurement of the displacement correlation $\langle \mathbf{R}_1 \mathbf{R}_2 \rangle$. The first case can provide a measurement of the velocity autocorrelation function [36].

Practical Considerations of MRM Experiments

An important aspect of NMR signal acquisition suggested in the imaging section above is the discrete nature of signal acquisition. For a Fourier acquisition modality the discrete signal can be written as [6, 37]

$$S(mT) = \frac{1}{N} \sum_{n=-N/2}^{N/2-1} M(n/NT) e^{-i2\pi mn/N} \qquad (2.34).$$

Where *T* is the data point time spacing and *N*-1 is the total number of discrete data points. In Eqn. (2.34) *S* is the NMR signal while *M* is the signal frequency distribution. With quadrature (complex) detection the maximum detectable frequency is $\pm 1/2T$ [37]. This discrete spacing sets the field of view in imaging, dynamic, and spectral measurements to $\pm 1/2T$. In a typical Fourier acquisition scheme one collects a number of data points in powers of 2 to allow rapid inversion by the fast Fourier transform [38].

Nuclear magnetic resonance experiments have an inherently low signal to noise ratio. For thermal polarization the signal to noise ratio is governed by the Boltzmann distribution and signal acquisition efficiency. To enhance the accuracy of experiments one often performs an equivalent set of experiments and then averages the signal over the set. The noise inherent to a

signal will appear in random phase throughout the set while the signal will be additive. The signal to noise ratio will then scale like $S/N \alpha \sqrt{N_{avgs}}$ [6].

This chapter has provided an overview of NMR theory and techniques used to measure spatial, chemical, and dynamic sample information. Dynamic and spatial information were shown to share a Fourier relationship with the bulk NMR signal while relaxation phenomenon shares a Laplace relationship. This chapter is meant to serve as a review; the reader is referred to the many descriptive texts cited throughout this work for a more comprehensive discussion of NMR theory and techniques.

THE LATTICE BOLTZMANN METHOD

The lattice Boltzmann method is a technique for simulating continuum hydrodynamics. The numerical technique had its theoretical beginnings in lattice gas (LG) automata which was quickly realized to be a variation of the discrete Boltzmann equation [39]

$$\frac{\partial f_i}{\partial t} + \mathbf{e}_i \cdot \nabla f_i = -\Omega_i + \mathbf{e}_i \cdot \mathbf{g}, \quad i = 1,...,b, \tag{3.1}$$

Where b is the number of discrete phase coordinates, f is the phase space probability distribution of particle streaming at velocity e, Ω is a relaxation operator governed by particle collision and **g** is a body force. A widely used model of Ω is the so-called BGK (Bhatnagar-Gross-Krook) approximation which assumes a single linear relaxation rate of the distribution functions to an equilibrium distribution

$$\Omega_i = \frac{1}{\omega}\left(f_i^{eq} - f_i\right) \tag{3.2}$$

The equilibrium distribution, f_i^{eq}, is chosen to recover the macroscopic Navier-Stokes equations. For small Mach numbers the distribution

$$f_i^{eq} = \rho \, \mathrm{w_i}\left[1 + 3\mathbf{e}_i \cdot \mathbf{u} + \frac{9}{2}\left(\mathbf{e}_i \cdot \mathbf{u}\right)^2 - \frac{3}{2}u^2\right] \tag{3.3}$$

recovers the Navier-Stokes equations to $O(u^2)$ [40]. Where $w_0 = 4/9$, $w_1 = w_3 = w_5 = w_7 = 1/9$, $w_2 = w_4 = w_6 = w_8 = 1/36$, and $\rho = \sum_i f_i$. The macroscopic velocity is given by $\rho \mathrm{u} = \sum_i f_i \mathrm{e}_i$. With the BGK approximation the first order upwind finite difference form of Eqn. (3.1) is

$$f_i\left(\mathbf{x}+\mathbf{e}_i\Delta x, t+\Delta t\right)=f_i\left(\mathbf{x},t\right)+\Omega_i\left(f\left(\mathbf{x},t\right)\right)+\mathbf{e}_i\cdot\mathbf{g} \qquad (3.4).$$

Where Δx and Δt are unit lattice spacing. The body force **g** models a macroscopic pressure gradient. The dynamic fluid viscosity is $v=\frac{2\omega-1}{6}\frac{\Delta x^2}{\Delta t}$. For a no-slip solid wall the boundary condition for Eqn. (3.1) is spectral f_i reflection (bounce-back) from the surface [41]; a first order boundary condition. Equation (3.4) and (3.2) coupled with the bounce back condition are used in the single phase hydrodynamic simulations in chapters 5 and 8. In these simulations symmetric boundary conditions coupled with the body force in Eqn. (3.4) model Newtonian fluid flow subject to a steady pressure gradient.

TRANSPORT IN POROUS MEDIA THEORY

Hydrodynamics

Fluid transport in porous media is a critical, often governing process for many biological, environmental and industrial systems. The vast implications of this phenomenon have motivated an extensive and comprehensive body of theory governing the hydrodynamics and transport of fluid in porous media. This thesis is concerned with steady Newtonian single-phase and Newtonian-colloid suspension dynamics in nonreactive, solid porous media lacking micro-porosity but having a fully open pore space. This system is composed of a solid media σ-phase and a saturating fluid β-phase, see Figure 11. The following discussion of transport in porous media theory is meant to serve as an introductory overview and reference guide for the results section of this thesis.

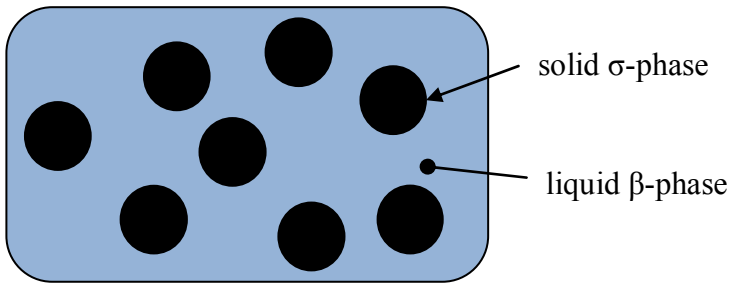

Figure 11: Porous media schematic

Single Phase Newtonian Hydrodynamics

Hydrodynamics in porous media are governed by scale dependent equations. At the lowest microscopic scale the Navier-Stokes equations govern the pore space Eularian velocity field in pressure driven flow. In steady flow of Newtonian fluid viscous hydrodynamics forces

typically are significantly greater than inertial forces so that the pore Reynolds number is much less than one: $\langle v_{\parallel} \rangle l / D_m \ll 1$ where l is the characteristic pore size, $\langle v_{\parallel} \rangle$ is the mean flow direction velocity and D_m is the molecular diffusion coefficient. In the low Reynolds number regime, termed Stokes flow, the pore-scale single-phase Eularian velocity field is governed by [42, 43]

$$\nabla \cdot \mathbf{v}_\beta = 0 \qquad (4.1)$$

$$\nabla p_\beta = \mu_\beta \nabla^2 \mathbf{v}_\beta + \mathbf{f}_\beta \qquad (4.2).$$

Where **v** is the local fluid velocity vector, p is the scalar fluid pressure, and **f** is a body force acting on the fluid. For solid, nonreactive surfaces the fluid-solid boundary condition for Eqn. (4.2) is $\mathbf{v}_\beta = 0$. Solving Eqns. (4.1) and (4.2) in the complex domain of a realistic porous media is an impractical task. Therefore, these equations are scaled up to a macroscopic description of hydrodynamics using the method of volume averaging [43]

$$\nabla \cdot \langle \mathbf{v}_\beta \rangle = 0 \qquad (4.3)$$

$$\langle \mathbf{v}_\beta \rangle = \frac{\mathbf{K}_\beta}{\mu_\beta} \cdot \left[\nabla \langle p_\beta \rangle^\beta - \rho_\beta \mathbf{g} \right] \qquad (4.4).$$

Equation (4.4) is the generalized form of Darcy's law resulting from averaging Eqn. (4.2) over the intrinsic phase average or liquid-phase volume. The averaging volume is assumed to be significantly greater than the pore size but less than the system size. During the averaging procedure a closure problem for variation of the local unknowns about their mean, Gray's decomposition: $\tilde{\mathbf{v}}_\beta = \mathbf{v}_\beta - \langle \mathbf{v}_\beta \rangle^\beta$, is necessary. Solution of the closure problem relates the

fluctuating unknowns to the permeability tensor, $\mathbf{K}_\beta$, in Eqn. (4.4). Equations (4.1) and (4.2) are a linear set of differential equations which can be cast into a single differential equation whose solution is independent of flow velocity and viscosity [44]. The flow profile of a Newtonian fluid in a porous media is therefore independent of viscosity and flow velocity in the Stokes regime. This linearity has important implications for the dynamics of transport in porous media as will be shown later in this thesis. An alternative form of Eqn. (4.4) exists to account for non-linear inertial effects; known as the Forchheimer equation [45]. Other forms have been developed to model two-phase macroscopic hydrodynamics [46].

Hydrodynamic Boundary Conditions

Equation (4.4) is irrotational, $\nabla\times\langle\mathbf{v}_\beta\rangle=0$, and therefore is thus unable to describe a macroscopic velocity shear gradient. Such a macroscopic gradient will exist near a free fluid or no-flow interface in cross-flow, see Figure 12.

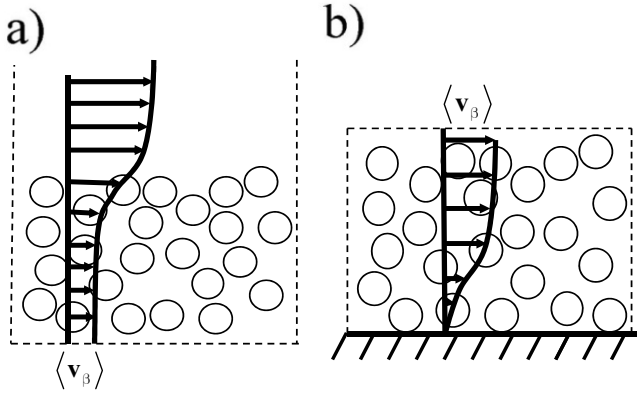

Figure 12: Two cases of macroscopic shear in porous media a) free surface in cross flow b) solid wall in cross flow

Equation (4.4) has been rigorously derived to account for macroscopic shear effects in porous media, the result is known as the Darcy-Brinkman equation [43]

$$\mu_{eff}\nabla^2\langle \mathbf{v}_\beta\rangle - \frac{\mu_\beta}{\mathbf{K}_\beta}\langle \mathbf{v}_\beta\rangle = \nabla\langle p_\beta\rangle^\beta \qquad (4.5).$$

The value of the Brinkman or effective viscosity, μ_{eff}, and even validity of the Brinkman correction in Eqn. (4.5) remains debatable [47, 48]. The brinkman viscosity is typically evaluated outside of the divergence operator, in which case following the analysis of Ochoa and Whitaker [43] $\mu_{eff} = \mu/\phi$, where μ is the fluid viscosity and ϕ is the porosity. However, Sahraoui and Kaviany [49] have shown the Darcy-Brinkman equation requires use of a variable effective viscosity to correctly model macroscopic shear and therefore the effective viscosity must be evaluated inside the divergence operator.

Case a) in Figure 12 requires additional considerations to model the hydrodynamic boundary layer. The broad occurrence of this physical scenario has promoted extensive inquiry into the correct form of the hydrodynamic boundary conditions [50-52]. The boundary conditions can be categorized by the scale of description; a macroscopic and mesoscopic scale, see Figure 13.

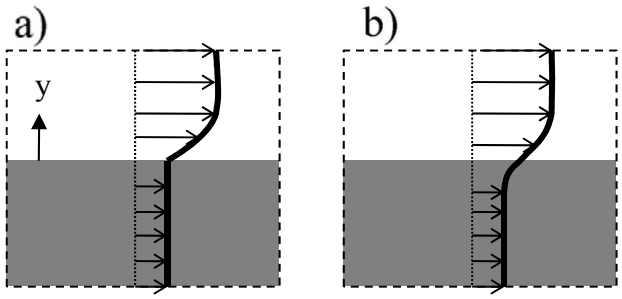

Figure 13: Two scales of porous media free surface cross-flow a) macroscopic b) mesoscopic

In Figure 13b) a single equation, valid over both domains, is assumed to govern the hydrodynamics [52]; *e.g.* Eqn. (4.5). This approach requires knowledge of the change in the

macroscopic quantities through the interface, *e.g.* **K** and ϕ. Of course knowledge of these quantities requires that interfacial morphology be resolved at the pore scale. For practical reasons this level of description is unfeasible and therefore the macroscopic approach in Figure 13a) is the more common method. In Figure 13a) the two domains are treated separate from another and an excess shear stress jump condition governs the free fluid velocity gradient at the interface. The first macroscopic boundary condition to appear in literature was a semi-empirical equation postulated by Beavers and Joseph [50]

$$\left.\frac{dv}{dy}\right|_{y=0} = \frac{\alpha}{\sqrt{K}}\left(v_s - \left\langle v\right\rangle\Big|_{y\to-\infty}\right) \qquad (4.6).$$

Where v_s is the free fluid velocity at the interface ($y = 0$) and α is an adjustable slip parameter. The value of α depends upon the interface location, $y = 0$, and therefore the value of α is not an intrinsic property of the interface. A closed form derivation was developed by Ochoa and Whitaker [52, 53] where the excess stress jump condition is derived from the volume averaged transport equation valid over the entire domain

$$\frac{1}{\phi}\left.\frac{d\left\langle v\right\rangle}{dy}\right|_{y=0^+} - \left.\frac{d\left\langle v\right\rangle}{dy}\right|_{y=0^-} = -\frac{\beta_1}{\sqrt{K}}\left\langle v\right\rangle\Big|_{y=0} \qquad (4.7).$$

Where β_1 is an adjustable parameter dependent on the chosen location of the interface, *e.g.* $y = 0$. Equations (4.6) and (4.7) are linear boundary conditions; therefore the interfacial excess shear stress scales linearly with flow velocity. While deriving Eqn. (4.7) Ochoa and Whitaker noted inertial effects may be important at a porous interface in cross flow, they stated: "*the curvature of the streamlines will be of the order of the pore or particle diameter and this may lead to non-*

zero values of the inertial terms, $\rho \mathbf{v} \cdot \nabla \mathbf{v}$" [52]. Equation (4.7) was modified by Ochoa and Whitaker to account for potential inertia effects [54]

$$\frac{\mu}{\phi}\frac{d\langle v\rangle}{dy}\bigg|_{y=0^+} - \mu\frac{d\langle v\rangle}{dy}\bigg|_{y=0^-} = \beta_1\frac{\mu}{\sqrt{K}}\langle v\rangle\big|_{y=0} + \beta_2\rho\langle v\rangle^2\big|_{y=0} \qquad (4.8).$$

Where β_2 modulates the inertial contribution to excess shear stress at the interface. To the author's knowledge the inertial term importance remains explored in literature. This may in part be due to the computational and experimental difficulty of investigating non-Stokesian flow at a porous interface. The importance of inertial effects at a porous interface is addressed in Chapter 8 using three dimensional pore scale LB simulations and NMR measurements.

Dispersion

Passive Scalar Transport in Porous Media

The pore scale transport of a passive scalar (*i.e.* temperature, mass, magnetization) in the convective velocity field within a porous media is modeled by the advection diffusion

$$\frac{\partial c}{\partial t} = D_m\nabla^2 c - \mathbf{v}\cdot\nabla c \qquad (4.9).$$

The following discussion is limited to mass transport. In Eqn. (4.7) c is the local mass concentration and D_m is the molecular diffusion coefficient. The subscript β has been removed from the fluid phase variables for simplicity. Equation (4.7) is an Eularian description of transport. An equivalent form is the Lagrangian frame which models movement of individual particles using the Langevin equation

$$d\mathbf{r} = dt\,\mathbf{v} + \sqrt{6D_m dt}\,\hat{\boldsymbol{\xi}} \qquad (4.10).$$

Equation (4.10) decomposes motion into deterministic and random components. In Eqn. (4.10) $d\mathbf{r}$ is the differential displacement over time dt of a passive particle in the convective field and $\hat{\xi}$ is a randomly oriented unit vector. The solution or Green's function of Eqn. (4.10) is the average of Eqn. (4.7) over all possible random trajectories integrated over a time Δ. This function is the probability of molecular displacement from $\mathbf{r}_1$ to $\mathbf{r}_2$ over time Δ: $\mathrm{P}\left(\mathbf{r}_1\middle|\mathbf{r}_2,\Delta\right)$. Solving Eqn. (4.7) at the pore scale or resolving $\mathrm{P}\left(\mathbf{r}_1\middle|\mathbf{r}_2,\Delta\right)$ in a porous media is a difficult task because of the convective profile complexity. Thus for practical purposes these equations are up scaled. The averaged form of Eqn. (4.7) is[44, 55]

$$\frac{\partial\langle \mathrm{c}\rangle}{\partial \mathrm{t}}+\nabla\bullet\left[\langle\mathbf{v}\rangle\langle \mathrm{c}\rangle-\mathrm{D}_{\mathrm{m}}\nabla\langle \mathrm{c}\rangle+\langle\mathbf{v}'\mathrm{c}'\rangle\right]=0 \qquad (4.11).$$

The volume averaged concentration and velocity vector are decomposed into a local variation about the mean using Reynolds or Gray's decomposition, $\mathbf{v}=\mathbf{v}'+\langle\mathbf{v}\rangle$. When pore scale velocities do not vary on a hierarchy of length scales and the volumetric average size is much greater than the largest length scale of velocity fluctuation, the closure solution for Eqn. (4.7) is [44, 56]

$$\frac{\partial\langle \mathrm{c}\rangle}{\partial \mathrm{t}}=\langle\mathbf{v}\rangle\bullet\nabla\langle \mathrm{c}\rangle-\mathbf{D}^{*}\nabla^{2}\langle \mathrm{c}\rangle \qquad (4.12).$$

The form of Eqn. (4.12) is equivalent to Eqn. (4.9) however the asymptotic dispersion coefficient, $\mathbf{D}^{*}$, is the result of molecular diffusion and spatial variations in flow velocity. In the long time limit the propagator of displacement $\mathbf{R}$ averaged over the starting position, $\overline{\mathrm{P}\left(\mathbf{R},\Delta\right)}$,

is the solution or Green's function of Eqn.(4.12). From the average propagator the asymptotic dispersion coefficient in Eqn. (4.12) is defined by the Einstein relation

$$\mathbf{D}^* = \frac{1}{2} lim_{t\to\infty} \frac{d\boldsymbol{\sigma}^2}{dt} \qquad (4.13).$$

Where $\boldsymbol{\sigma}^2$ is the variance or second moment of the average propagator: $\boldsymbol{\sigma}^2 = \int_{-\infty}^{\infty} |\mathbf{R}|^2 \overline{P(\mathbf{R},\Delta)} d\mathbf{R}$.

An alternative definition of the asymptotic dispersion coefficient is the Green-Kubo relation using the average autocorrelation function of tracer velocity

$$\mathbf{D}^* = \int_0^{\infty} \langle \mathbf{v}'(0)\, \mathbf{v}'(t) \rangle dt \qquad (4.14).$$

An asymptotic dispersion coefficient as defined by Eqns. (4.14) and (4.13) implies an exponential decaying velocity autocorrelation with time and therefore an average propagator that evolves in time according to a Gaussian function[31]. The time regime much shorter then that necessary to fulfill the long time limit in Eqn. (4.13) is known as preasymptotic dispersion. For real transport dynamics Eqns. (4.13) and (4.14) will produce slightly different values of the asymptotic dispersion coefficient because Eqn. (4.14) retains preasymptotic information while Eqn. (4.13) is temporally localized to the long time limit. In the preasymptotic regime or when the velocity profile fluctuates on a hierarchy of length scales the dispersion flux in Eqn. (4.12) is not proportional to the local concentration gradient[57]. In these anomalous dispersion examples Eqn. (4.13) is not valid and therefore the variance will grow in time either greater than linear (super-diffusive) or less than linear (sub-diffusive)[58]. A nonlocal approach is necessary to model transport in the case of anomalous dispersion. The effective dispersion coefficient is defined according to the nonlocal approach as[57]

$$\mathbf{D}^{\mathrm{NL}}\left(\mathbf{R},\tau\right)=\int \mathbf{v}'\left(\mathbf{r}\right)\mathbf{v}'\left(\mathbf{r}+\mathbf{R}\right)\mathrm{P}\left(\mathbf{r}\right)\mathrm{P}\left(\mathbf{r}\middle|\mathbf{r}+\mathbf{R},\tau\right)\mathrm{d}\mathbf{r}$$
$$\mathbf{D}^{*}=\int_{0}^{\infty}\int_{V}\mathbf{D}^{\mathrm{NL}}\left(\mathbf{R},\tau\right)\mathrm{d}\mathbf{R}\mathrm{d}\tau \tag{4.15}$$

The nonlocal dispersion tensor, $\boldsymbol{D}^{NL}$, is the velocity autocorrelation as a function of displacement **R** averaged over the initial position **r**. In the nonlocal approach, the asymptotic dispersion coefficient is the nonlocal dispersion tensor integrated over displacement and time. The generalized concentration flux is the convolution integral of the nonlocal dispersion tensor and concentration gradient integrated over past time and starting position.

Non-Equilibrium Statistical Mechanics of Preasymptotic Dispersion: This section is concerned with adopting results from nonequilibrium statistical mechanics which serve as a model of preasympototic dispersion in porous media. The governing equation of a self correlation function of motion (velocity autocorrelation function) $\psi\left(t\right)=\left\langle \mathbf{v}'\left(0\right)\mathbf{v}'\left(t\right)\right\rangle \big/ \left\langle \mathrm{v}_{o}{}^{2}\right\rangle$, is known as the memory function equation

$$\dot{\psi}=-\int_{0}^{t}K\left(t-t'\right)\psi\left(t'\right)dt' \tag{4.16}$$

In Eqn. (4.16) K is known as the memory function. Equation (4.16) is formally derived from the Liouville equation of motion and projection operator formalism [59]. Because of the generalized nature of the derivation, Eqn. (4.16) is applicable to any multibody system of dynamics; *e.g.* molecular hydrodynamics, turbulence, porous media, etc. It is through the memory function that a model of $\psi\left(t\right)$ is typically introduced and thus has significant practical as well as theoretical

value. At short times K is equal to the force autocorrelation function: $K(0) = \langle \mathbf{F} \rangle / m \langle \mathrm{v}_o^{\,2} \rangle = \langle \dot{\mathbf{v}}^2 \rangle / \langle \mathrm{v}_o^{\,2} \rangle$. The formal solution of Eqn. (4.16) in terms of the frequency moments of the velocity autocorrelation function is due to Mori [60], the result is

$$\tilde{\psi}(\mathrm{s}) = \frac{1}{\mathrm{s}+\ldots} \frac{\omega_{\mathrm{v}}^2}{\mathrm{s}+\ldots} \frac{\left(\omega_{\mathrm{v}}^4 / \omega_{\mathrm{v}}^2\right) - \omega_{\mathrm{v}}^2}{\mathrm{s}+\ldots} \cdots \tag{4.17}$$

This equation expresses the Laplace transform of the velocity autocorrelation function is terms of its frequency moments. It is easy to show that the short time behavior of the velocity autocorrelation function is given by the frequency sum rule

$$\psi(t) \underset{t \to 0}{=} 1 - t^2 \omega_v^2 + \mathrm{O}\left(t^4\right) \tag{4.18}$$

Where the second frequency moment is $\omega_v^2 = K(0) = \langle \dot{\mathbf{v}}^2 \rangle / \langle \mathbf{v}_o^{\,2} \rangle$; the restoring force of the dynamics. The form of Eqn. (4.17) provides a basis for models of K(t). Truncating Eqn. (4.17) to second order produces the exponential memory function model [61]

$$K(t) = \omega_v^2 \exp(-t/\tau) \tag{4.19}.$$

Equation (4.19) is used as a model of the dynamics in chapter 5, the resulting autocorrelation function is given by

$$\psi(t) = \exp(-t/2\tau) \left[\cos \bar{\omega} t + \left(\frac{1}{2\bar{\omega}\tau} \right) \sin \bar{\omega} t \right] \tag{4.20}.$$

Where the frequency of oscillation is governed by both the relaxation time and leading coefficient of the model; $\bar{\omega} = \sqrt{\left(\omega_v - 1/4\tau^2\right)}$. Examples of the effective diffusion coefficient

from the exponential memory function model are plotted in Figure 14 for several values of the relaxation time with $\omega_v = v_o = 1$.

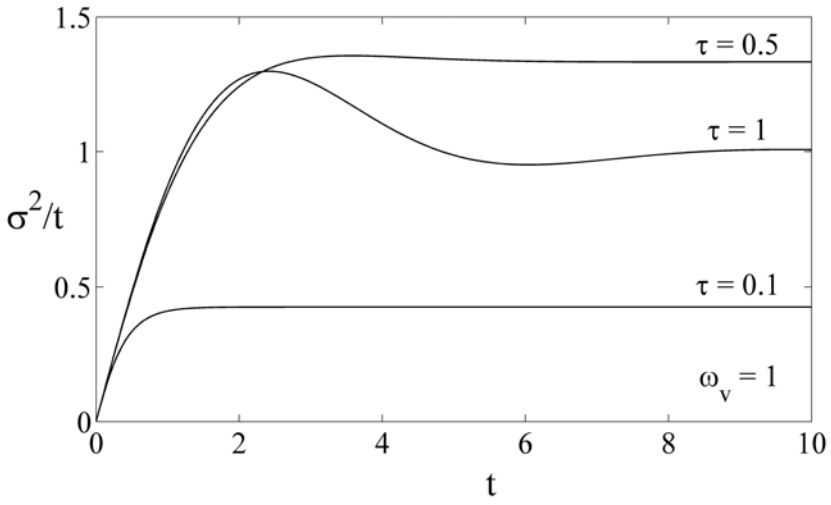

Figure 14: Effective diffusion coefficient of the exponential memory function model plotted for several values of the relaxation time with $\omega_v = v_o = 1$

At small values of the relaxation time coherence is lost in the dynamics and the dispersion coefficient rapidly asymptotes to a constant rate. As the relaxation time increases the effective diffusion coefficient develops a coherence pattern at regular beats similar to sinusoidal flow. In this domain *structural information* is apparent within the dynamic behavior. There are many other models for the memory function in the literature, the reader is referred to other work for discussion of these models [61].

Colloid Transport in Porous Media

Colloid transport in porous media refers to the transport of Brownian, rigid particles suspended in a fluid (assumed Newtonian). The first order advection diffusion equation has been used to model macroscopic transport of a passive scalar and colloidal particles.

$$\frac{\partial \langle c \rangle}{\partial t} + \mathbf{v} \cdot \nabla \langle c \rangle = \nabla \cdot \left[\mathbf{D}^* \cdot \nabla \langle c \rangle - k_{att} \langle c \rangle \right] \qquad (4.21).$$

Where $\langle c \rangle$ is the macro scale average concentration of the colloidal particles or liquid-phase and the reaction coefficient, k_{att}, accounts for deposition of colloidal particles on the porous structure surface. Dispersion of colloidal suspension in porous media, modeled by $\mathbf{D}^*$ in Eqn. (4.21), remains a mostly unexplored phenomenon. In order to calculate $\mathbf{D}^*$ and k_{att}, Eqn. (4.21) must be assumed to govern particle and liquid phase transport and then fit to breakthrough curves [62-64]. Models based on the *passive* random walk of individual particles have been used to investigate particle dispersion and particle deposition [65]. However, colloidal particle hydrodynamics and hence transport is governed in part by particle-particle collision, inertia, and forces induced by colloid-porous media interaction [66].

For a colloidal suspension the displacement dynamics are discretized by the two phases. Equation (4.21) makes a direct assumption about the existence of an asymptotic dispersion coefficient. However there appears to be no direct evidence demonstrating Eqn. (4.13) for either phase of real colloidal suspension transport dynamics in porous media. In chapter 6 the existence of Eqn. (4.13) as it applies to colloid suspension dynamics is investigated. The transient evolution of pore structure resulting from colloid filtration or deposition, suggested by

k_{att} in Eqn. (4.21), suggests non-Markoffian and hence anomalous transport dynamics. The results presented in chapter 6 apply to the stationary regime of colloid transport where $k_{att} = 0$. Further work beyond what is presented in this thesis is needed to explore suspension dynamics modulated by transient pore structure changes resulting from colloid deposition.

STUDY OF TRANSPORT IN CELLULAR MEDIA & STRUCTURE CHARACTERIZATION BY TRANSPORT DYNAMICS

Introduction

Solid cellular structures are an important class of technological and natural porous media. Many highly optimized naturally occurring materials (e.g. lightweight woods, sponges, cancellous bone, etc.) are cellular in nature[67, 68]. Some properties of cellular structures including low permeability and high solid phase surface area to fluid volume ratio have been recognized as attractive characteristics to optimize transport applications[69-71]. Despite the advantageous utility of cellular materials for transport applications there is limited published data on temporal and asymptotic dispersion dynamics. In this work, dispersion refers to transport of a passive scalar within a steady, non-reacting, Newtonian velocity field. A potential explanation for this literature gap is the absence of efficient structural characterization methods[72]. Consideration of cellular structures as porous media leads to the concept of a transport length scale [73, 74]. In the study of consolidated granular porous media the length scale is taken to be a characteristic pore size $l \sim \phi/(1-\phi)(V/S)$ based on the surface to volume ratio (S/V) and volume fraction ϕ, which derives from the concept of *hydraulic radius* in fluid mechanics. In highly porous solid foams, complications in structural simulation and modeling are posed by the solid phase forming a sample spanning cluster, which is not the case in lower porosity granular porous systems where phases become isolated as in percolation theory when $p < p_c$ [73, 75]. This suggests definition of a characteristic length scale governing transport in foams an open and important question. A component of this chapter is to present a direct characterization of the transport length scale in open cell solid random foam using pulsed

gradient spin echo nuclear magnetic resonance (PGSE NMR) measurements and Lattice-Boltzmann (LB) simulation of short time correlations inherent to the hydrodynamic dispersion molecular dynamics during pressure driven fluid flow. Dynamic PGSE NMR measurements have been found to provide length scale characterization due to pore structure sampling by molecular diffusion [76, 77] and advection [78, 79]. PGSE NMR measurement and LB simulation of scale-dependent hydrodynamic dispersion has been systematically applied to compacted granular media [79-85] but not to characterize transport in open-cell foams. NMR measurements [83, 85] and LB simulations [86] of hydrodynamic dispersion in random spherical bead packs demonstrate a correlated motion in the transverse direction perpendicular to the applied flow. This results in a negative lobe in the transverse velocity autocorrelation function (VACF), and equivalent preasymptotic maxima in the time dependent hydrodynamic dispersion coefficient, analogous to that observed in molecular dynamic simulations of dense fluids [87, 88]. In this work an equivalent phenomenon is shown to occur in open cell foams. This short time correlation provides a measurement of the characteristic structure length. Nonequilibrium statistical mechanics has been used to rigorously derive a theory of preasymptotic hydrodynamic dispersion for porous media with hierarchical structure [89] in the context of time correlation functions of dynamical variables [87, 88]. This formalism, which is outlined in the previsou chapter, is adopted as a theoretical framework and model of the preasymptotic correlations inherent to transverse dispersion in foam structures and other porous media.

This chapter is organized as follows. Section one is an introduction to the polymeric cellular structures, section two presents the PGSE NMR and LB dispersion data and the

nonequilibrium statistic mechanics model fit, section three interprets some of the stochastic dynamics in section two with an elementary toy model, and section four summarizes the data.

Polymer Cellular Structures

Solid cellular structures are composed of an interconnected network of solid thin struts or ligaments which merge at junctions to form polyhedral-like volumetric cells. The faces or windows of the volumetric cells can be either filled (closed cell) or unfilled (open cell) with the structure material. A number of image based techniques and methodologies exist for quantifying the structure of three dimensional foams [67, 70, 72, 90, 91]. Using three dimensional NMR and CT images, Montminy *et al*. found real open cell polymer foam structures to have highly disperse geometric statistics (*e.g.* strut length, intersection angles, etc.). Furthermore it was found that real polymer foam structures are primarily composed of irregular pentagonal windows and polyhedral-like volumes. Idealization of foam structures by some form of the polyhedral family of unit cells is a common interpretation of foam structures [67, 92-97]. Gibson and Ashby noted the Kelvin cell approximation, tetrakaidecahedron, closely resembles the polymer foam structure.

The NMR transport measurements in this work are limited to commercial open cell polymer foam, see Figure 15.

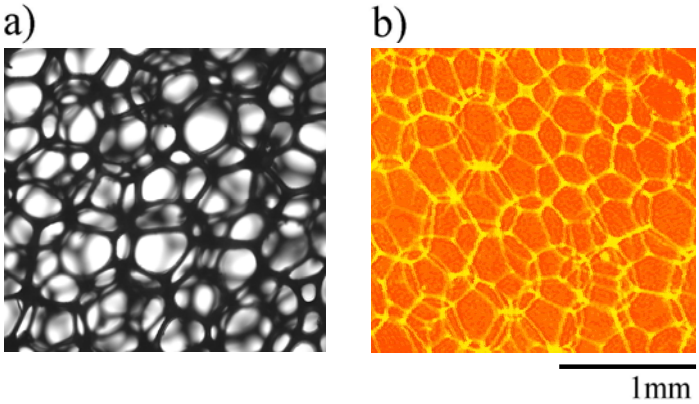

Figure 15**:** Images of 110 PPI Foamex open cell polyurethane foam a) optical b) MRI.

It is clear from the images in Figure 15 that the polymer foam structure is composed of a hetereogenous network of polyhedral-like volumetric cells. Incorporating *all solid structure statistics* from the images into a single length scale is obviously a challenging if not ill-posed problem. In this work 110PPI and 80PPI Foamex© polyeurthane foam are used in the NMR transport measurements and a digitized 50PPI Air Products© polyeurthane foam is used for the LB simulations. The 110PPI foam structure geometry was characterized through two dimensional images from an Olympus© Bx41 optical microscope interfaced with a Xli© CMOS digital camera, see Table 1. Also shown in Table 1 are statistics from the digitized polymer foam.

Table 1: Foam structure geometry statistics

Parameter	*110PPI foam*	*50PPI foam, Montminy et al. [72]*
Mean strut length	198 μm*	281 μm
Mean strut width	60 μm	-
Porosity	97%	93%
Window shape distribution		
quadrilaterals-	21%	24%
pentagons	62%	55%
hexagons	15%	19%
heptagons+	2%	1%

*A probabilistic technique applied to two dimensional images was used to measure the mean strut length, see Appendix A

The porosity of the 80PPI foam sample is 97%. The characteristic length of commercially available foam is reported by the manufacturer designated pores per unit length, *e.g*. PPI (pores per inch). Typically, this number reflects the mean hydraulic diameter of the windows. The definition and measurement of this number can vary [97] and does not account for all structure statistics [91].

Experimental Results and Discussion

Spatially Resolved Flow Velocity Images

The spatially resolved PGSE NMR experiment was used to measure two dimensional images of steady water flow through the 110PPI foam structure, see Figure 16. Image a) in Figure 16 is in the transverse plane parallel to the flow direction, image b) is in the axial plane, and image c) is in the transverse plane of the LB simulation coursed grained to a similar axial

resolution as image b). In plane resolution is 1.0 mm in images a) and b) and 1.9 mm in image c).

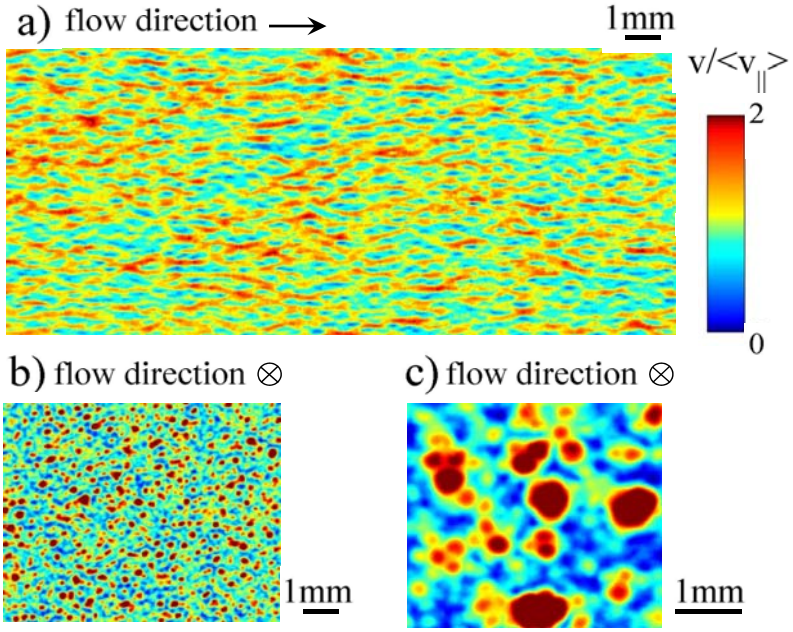

Figure 16**:** Two dimensional experimental NMR images at different orientations of the axial component of the microscopic velocity field within the 110PPI foam pore structure averaged over the slice thickness of 1.0 mm, 34 x 34 μm/pixel, Δ = 10 ms, $<v_{||}>$ = 0.95 mm/s

Image weighting in Figure 16 is the flow velocity magnitude in the direction of applied pressure gradient; this direction is referenced by the || subscript and the transverse direction by ⊥. Inspection of images b) and c) in Figure 16 demonstrates how the foam structure segregates the convective profile into a distribution of poisuelle-like channels. In the images there is heterogeneity in the convective profile on multiple length scales, which is an indication of the cellular structure heterogeneity. This heterogeneity is also evident in image a) of Figure 16. A close examination of image a) in Figure 16 suggests a remarkable homogeneity in the streamline bifurcations, which indicates a high degree of coherent oscillatory motion in the transverse

plane. Image b) in Figure 16 was quantified using the normalized spatial auto correlation function of the flow velocity fluctuating component: $\left\langle v_{\parallel}'(\mathbf{r})v_{\parallel}'(\mathbf{r}+\mathbf{R})\right\rangle / \left\langle v_{\parallel}'^{2}\right\rangle$, see Figure 17. The spatial correlation function shown in Figure 17 is averaged over two in-plane orthogonal coordinates of image b) in Figure 16.

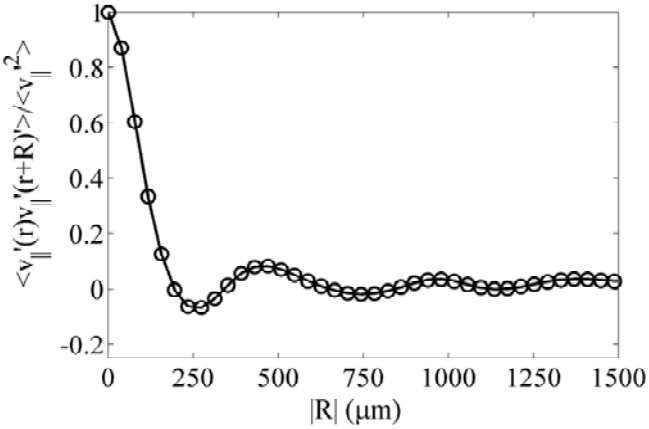

Figure 17: Spatial self correlation function of the fluctuation about the mean velocity from the in-plane experimental NMR flow velocity image b) in Figure 16

The curve shown in Figure 17 is characterized by a damped oscillation with a wavelength of approximately 500 μm. The oscillations shown in Figure 17 are the result of structure periodicity (the cells) which imparts a similar periodicity in the Eularian convective velocity field. This analysis suggests the characteristic length of the 110PPI structure to be on the order of 250 μm. The correlation function of Figure 17 agrees for two orthogonal directions at displacements of less than 250 μm. Another useful statistic is the probability distribution of flow velocities. Knowledge of the pore scale velocity probability distribution allows one to estimate the short time dynamics of dispersion through a convolution with molecular diffusion [reference needed]. Figure 18 shows a comparison of the probability distribution of normalized axial flow

velocities from two transverse plane NMR flow velocity images (the orientation of image b) in Figure 16) and the non-coarse grained flow velocity distribution from the LB simulation.

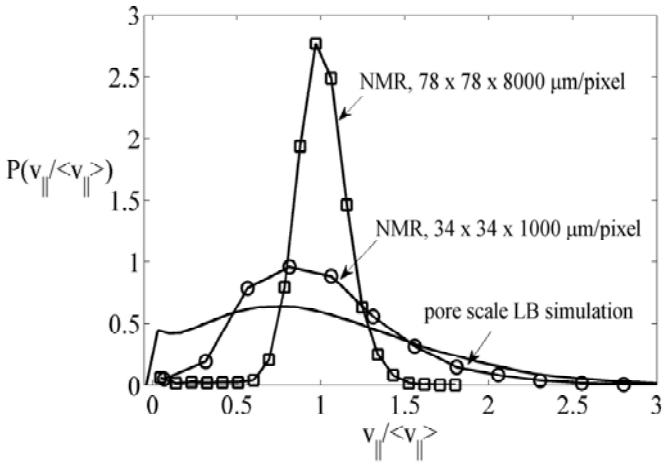

Figure 18: Probability distribution of the normalized axial flow velocity compared for two in-plane NMR images at different voxel resolutions and from the three dimensional pore scale lattice Boltzmann simulation

The experimental and numerical curves of Figure 18 differ due the variation in spatial coarse graining of the data sets. The non-coarse grained lattice Boltzmann curve is characterized by a small population at zero velocity and a large high speed population with a maximum at $v_{\|}/\langle v_{\|}\rangle \approx 0.8$. One might conceptualize the flowing population as the superposition of flow velocity populations from the distribution of tubular-like passages. The maximum pore scale flow velocity from the lattice Boltzmann simulation is $v_{max} \approx 4.5\langle v_{\|}\rangle$, for a packed bed of monodisperse spheres this relationship is $v_{max} \approx 10\langle v_{\|}\rangle$ [98], and for a circular tube $v_{max} = 1.5\langle v_{\|}\rangle$. The spatial coarse graining of the NMR experiment represents a loss of information in regard to the velocity probability distributions in Figure 18. In the limit of infinite voxel size the normalized velocity probability distribution is a delta function: $P\left(v_{\|}/\langle v_{\|}\rangle\right) = \delta\left(v_{\|}/\langle v_{\|}\rangle - 1\right)$. The

velocity probability distribution transition to a delta function is governed by the voxel size relative to the scale(s) in the velocity field heterogeneities. A comparison of the velocity probability distribution at different voxel sizes and slice thicknesses therefore gives an indication of the proper representative element volume (REV) size [99].

Temporal Dispersion Dynamics in Foam

The distributions of Figure 18 are an instantaneous Eularian observation of the convective velocity field and therefore have a limited description of transport. This section provides a systematic outline of dispersion dynamics in the foam structures using the NMR and LB measured spatially coursed grained probability of displacements or van-Hove self correlation function, $\overline{P(\mathbf{R},\Delta)}$, and its moments. Shown in Figure 19 and Figure 21 is the temporal evolution of the volume averaged propagator in the 110PPI foam for the longitudinal and transverse directions at a mean flow velocity of 3.4 mm/s. Also shown in Figure 19 is the temporal evolution of the volume averaged propagator from the LB simulation. The distributions shown in Figure 19 and Figure 21 are the magnitude of the Fourier transformed single PGSE signal which is obtained as a function of the displacement frequency variable **q** for fixed observation times.

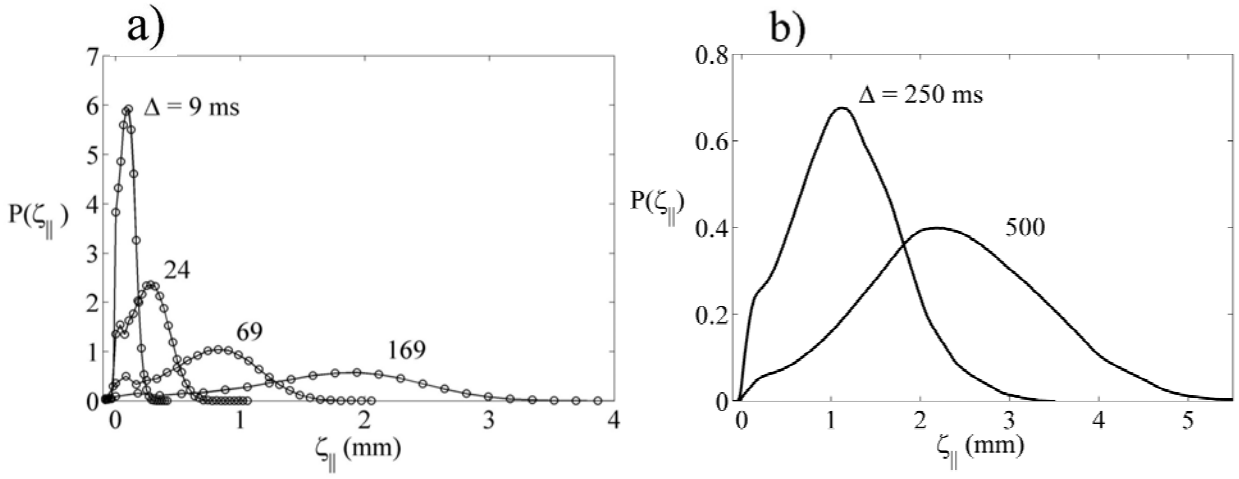

Figure 19: Temporal evolution of the axial displacement propagator a) NMR - 110 PPI foam $\langle v_{\|} \rangle$ = 3.4 mm/s b) LB – 50 PPI foam $\langle v_{\|} \rangle$ = 4.7 mm/s

The axial displacement propagators in Figure 19 are characterized by two distinct populations. The slow flowing population near $\zeta_{\|} = 0$ is distinct from the fast moving bulk population. The slow moving population represents fluid within the boundary layer very near the foam structure or regions of relatively high permeability (*e.g.* the sample outer surface boundary layer) or fluid trapped within stagnant or closed streamline features. The slow flow population in the foam data is not a true stagnant feature because it contains a net axial displacement. The axial displacement propagators in Figure 19 can also be viewed in the reciprocal *q*-space or Fourier domain, see Figure 20.

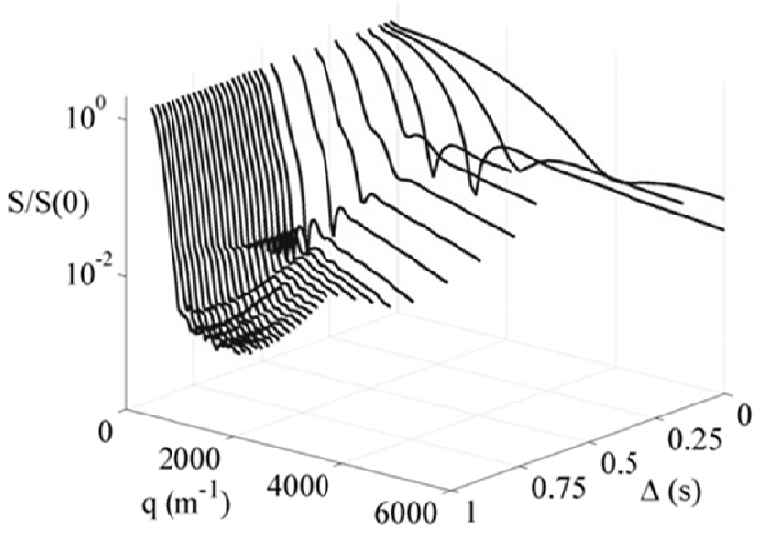

Figure 20: Axial displacement propagator signal magnitude q-space domain dynamics from Figure 19

Figure 20 reveals some interesting behavior. Initially, there is a single diffraction feature which moves toward $q = 0$. This feature results from spreading of the two populations in the displacement domain and scales like $q\Delta$. As the observation time increases additional diffraction features begin to appear in the q-space dynamics. These features could represent additional populations in the displacement dynamics which are too small to significantly impact the initial q-space dynamics.

At short times and in the high Peclet number limit the transverse displacement propagator is characterized by a propagator shape similar to a Lorentzian distribution. At higher observation times the pre-asymptotic transverse propagator transitions to a Gaussian. The distribution shape at the two limits of observation time is similar to a stochastic process resulting from a sequence of interactions governed by a Poisson distribution.

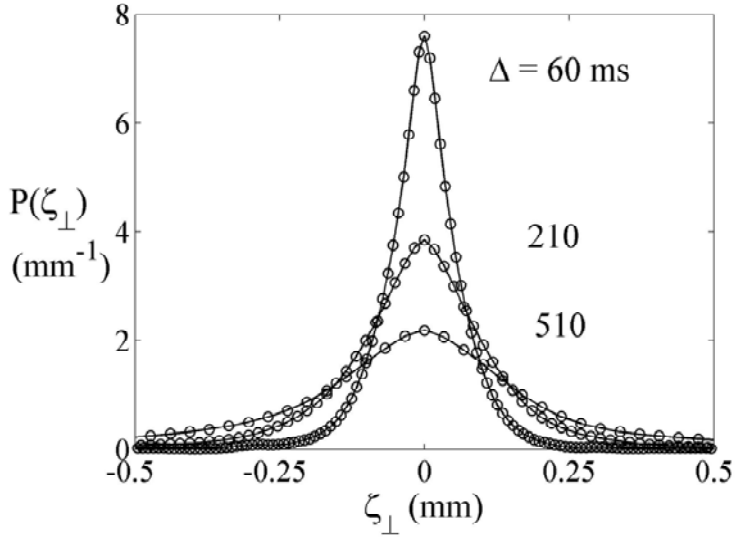

Figure 21: Temporal evolution of the transverse displacement propagator within the 110 PPI foam pore structure, $\langle v_{\parallel} \rangle$ = 3.4 mm/s

Using the low q cumulant expansion given in Eqn. (2.31) the transverse and axial variance temporal evolution was measured using the single pulse PGSE experiment; see Figure 22 and Figure 23. The error bars shown in the following figures are 95% confidence intervals of the data points.

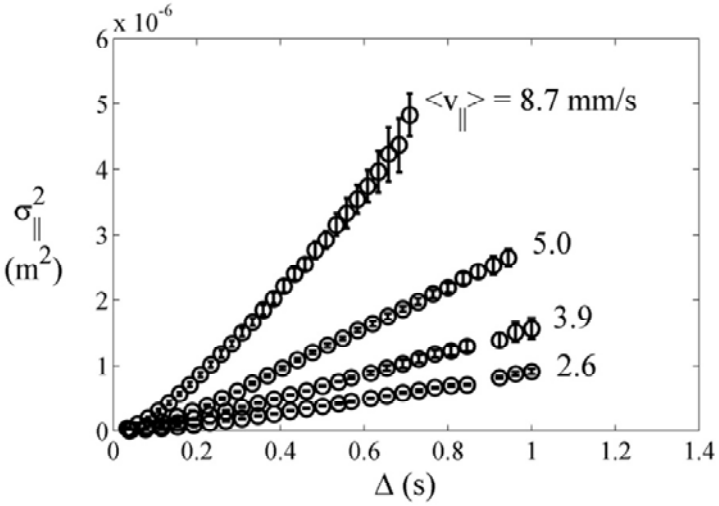

Figure 22: Temporal evolution of the axial displacement variance within the 110 PPI foam structure as a function of mean flow velocity

The linear growth of the axial variance at high observation time, $\Delta > 0.4$s in Figure 22 suggests the onset of asymptotic, stationary, Gaussian dynamics. This suggests the validity of Fick's law to modeling transport in the structure. Furthermore, it suggests that a REV for the structure exists. In the asymptotic regime the effective asymptotic dispersion coefficient is given by Eqn. . The asymptotic axial dispersion coefficient scaling with Peclet number is reported later in the text. At short times, $\Delta < 0.2$ s, and in the high Peclet number limit the axial variance grows ballistically: $\sigma_{\|}^2 = \left\langle v_{\|}'^2 \right\rangle t^2$.

The temporal evolution of the transverse variance at high Peclet number is characterized by approximately four time domains.

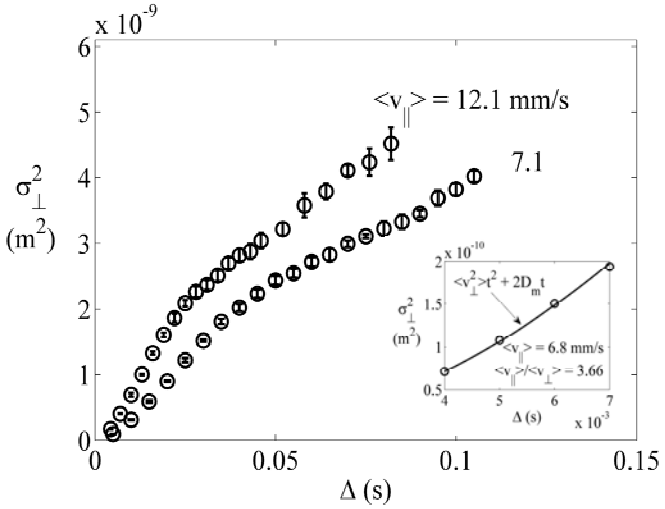

Figure 23: Temporal evolution of the transverse displacement variance for the 110 PPI foam for two mean flow velocities, inset: short time evolution of the transverse variance for a single mean flow velocity superimposed is a ballistic plus diffusive fit for the variance evolution; D_m = 2x10^{-9} m^2/s, $<|v_{\perp}|>$ = 1.8 mm/s

Initially the transverse variance evolves according to molecular diffusion. As the observation time is increased convective begins to dominate and ballistic growth of the variance occurs. The inset of Figure 23 shows the short time growth of the transverse variance for a single flow velocity and a fit of the data to a model superimposing ballistic and diffusive motion. Using this model the mean amplitude of the transverse flow velocity was found to be 1.8 mm/s when the mean flow velocity was 6.8 mm/s. The ratio of axial and transverse velocity, $\langle v_{\parallel} \rangle / \langle |v_{\perp}| \rangle = 3.78$ for the 110 PPI foam, is a fixed constant in the Stokes flow regime. For the simulated LB foam this constant was found to be $\langle v_{\parallel} \rangle / \langle |v_{\perp}| \rangle = 4.66$. As the observation time increases beyond the ballistic regime the variance growth experiences a transition regime due to recorrelation of tracer particles with their original transverse position. This recorrelation effect is a result of the oscillatory streamline motion around the structure of the cellular foam media; this effect will be further discussed below. The linear growth of the transverse variance at high observation times, e.g. $\Delta > 0.05$ s, signals the onset of asymptotic dispersion.

The transverse and axial variance can be converted to an effective time dependent dispersion coefficient through dividing the variance data points by the observation time. Shown in Figure 24 is the temporal evolution of the effective axial dispersion coefficient compared for the single and double PGSE experiments. The effective dispersion coefficient from the single PGSE experiment reflects the dynamics of the true volume averaged propagator variance. The double PGSE experiment refocuses coherent motion so that the evolution of the double PGSE dynamics shown in Figure 24 are governed by the stochastic or random dispersion dynamics.

The double PGSE data in Figure 24 is for the case of null mixing time; e.g. the dynamics given by Eqn. (2.33) b.

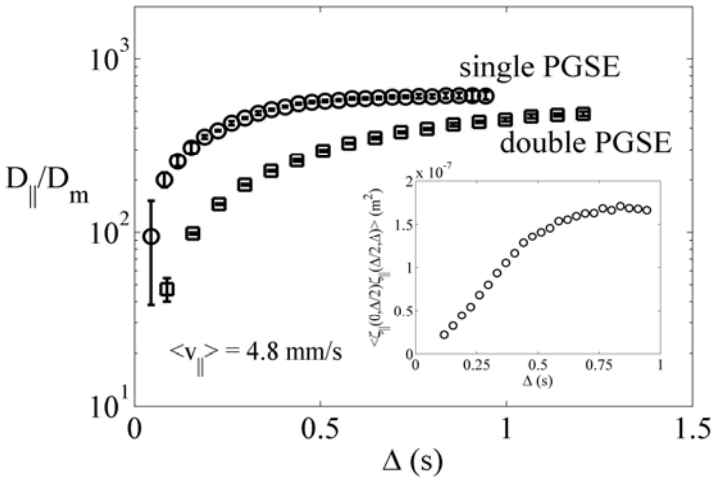

Figure 24: Comparison of the single and double PGSE effective axial dispersion coefficient for the 110 PPI foam as a function of observation time, D_m = 2x10^{-9}m^2/s, inset: axial displacement correlation function determined from a comparison of the single and double PGSE effective dispersion coefficient

A comparison of the single and double PGSE effective dispersion coefficient allows for calculation of the axial displacement correlation function as shown in the inset of Figure 24. If the effective dispersion coefficients of the single and double PGSE experiment asymptote to a fixed asymptotic dispersion coefficient (e.g. if the displacement of tracer particles are entirely uncorrelated between the two gradient encoding intervals of the double PGSE experiment) then displacement correlation function must grow slower than *t*. At high observation times this behavior is present in the inset of Figure 24 which further suggests the applicability of Fick's law to modeling transport in the structure.

The following discussion returns to the recorrelation dynamics of transverse dispersion in the foam structures. The problem of defining and accurately measuring a characteristic length in foams, which was posed in the introduction, is now addressed. The recorrelation regime of transverse dispersion can be interpreted using the time dependent effective dispersion coefficient ($D_\perp = \sigma^2/\Delta$), see Figure 25.

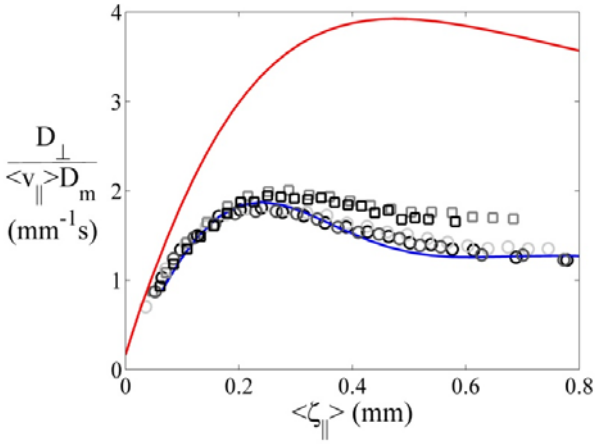

Figure 25: NMR measured and simulated hydrodynamic dispersion coefficient normalized by the molecular diffusion of the fluid and mean flow velocity as a function of displacement observation time Δ in terms of mean displacement length $<\zeta_\parallel> = <v_\parallel>\Delta$ at 3 flow rates for the 110 PPI foam (open circles) and the fit to the dynamics with the exponential memory function (blue line) and 2 flow rates for the 80 PPI foam (open squares) and 1 flow rate for the 50 PPI LB foam sample (red line)

The increase and plateauing decrease of the transverse dispersion coefficient shown in Figure 25 is a stochastic phenomenon known as *backscattering* [100] . The backscattering dynamics are a reflection of the oscillatory streamline waveform of the fluid navigating through the foam structure and hence a reflection of the structure itself. The oscillatory motion forces some fluid molecules to recorrelate nearly or completely to their original transverse position after flowing

some distance in the axial direction. The data collapse in Figure 25 is due to the linearity of transverse dispersion with flow velocity in the high Peclet number limit [101]. Transverse backscattering is known to occur in flow through mono-disperse packed beds [98, 102, 103]. In a study of 2D displacement correlation dynamics in monodisperse packed beds and a sandstone rock core, Stapf *et al*.[102] noted similar correlations suggest a measurement of the structure characteristic length. Also shown in Figure 25 is a model fit to the 110 PPI NMR data using the exponential memory function model in Eqn. (4.19) fit to the data using a nonlinear least squares routine. The model oscillates somewhat more strongly than the data however the general agreement is quite good over the range of observation time. The model fit values are given in Table 2.

Table 2: Exponential memory function model values for the 110PPI foam

$\langle v_{\parallel} \rangle$ (mm/s)	ω_v^2 (s^{-2})	τ (s^2)	ϖ_2 (s^{-1})
15	31807	0.0117	178
12.1	21308	0.0137	145
7.1	7714	0.0199	88
3.7	2309	0.0362	48

The maximum of the dispersion curves in Figure 25 occur at a fixed mean displacement of $l = \langle \zeta_{\parallel} \rangle \big|_{dD_{\perp}/d\Delta=0}$ with l = 250 μm for the 110PPI foam, l = 300μm for the 80PPI foam and l = 475μm for the 50PPI LB simulated foam. This fixed displacement is on the order of the streamlines primary axial oscillations half wavelength. For a foam structure one would expect this distance to be on the order of the intercellular spacing and indeed these lengths agree well with the quantity provided by the manufacturer in the units of pores per inch. This definition of length scale is *deterministic* and accounts for *all structure statistics*. Its accuracy is only limited

by the ability to resolve the curves in Figure 25. This is in contrast to *ad hoc* image analysis of foam structures where measurement accuracy contains inherent error because of the nondeterministic nature of pore size or length scale definition and subsequent measurement.

A primary role of characteristic length scale is to serve as a universal scaling parameter. If a set of foam structures are self similar, *e.g.* if the underlying geometry of the structures are invariant to physical dimension, then the length scaled defined above will serve as a universal scaling parameter. To demonstrate this it is instructive to plot a normalized version of Figure 25, see Figure 26.

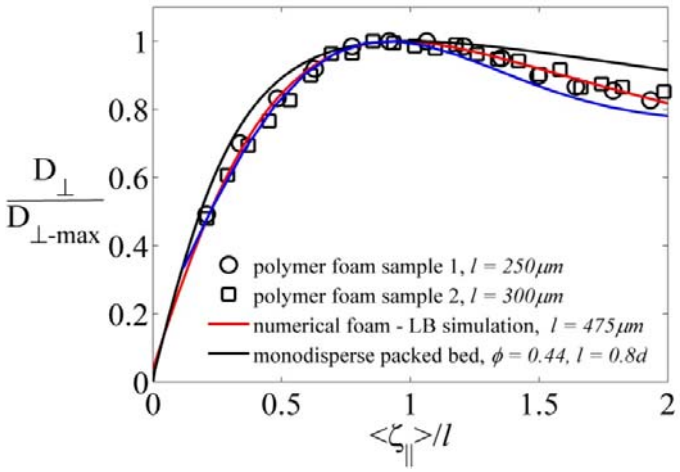

Figure 26: The transverse dispersion coefficient normalized by its maximum amplitude as a function of the axial displacement length scaled by the transport length scale l for LB simulation (red line), the NMR data for the 110 PPI (open circles), 80 PPI (open squares), the scaled memory function model (blue line) and LB simulation for a consolidated random sphere packing [24] (black line).

The three foam samples data collapse shown in Figure 26 suggests the underlying geometry of the structures to be invariant to physical dimension. The monodisperse packed bed dynamics

(black line) nearly agree with the foam dynamics at short times, suggesting the streamline paths of the packed bed are similar to the foam structure, an interesting if only coincidental similarity.

The recorrelation effect is confirmed by observing the normalized mean displacement dependence of the normalized transverse velocity autocorrelation function: VACF = $\langle v_\perp(0)v_\perp(t)\rangle / \langle {v_\perp}^2 \rangle$. Shown in Figure 27 is the VACF for the LB simulation and 110 PPI NMR data calculated from the second time derivative of the transverse variance in Figure 23. Also shown in Figure 23 is the exponential memory function model fit. The VACF curves shown in Figure 27 are for the high Peclet number limit.

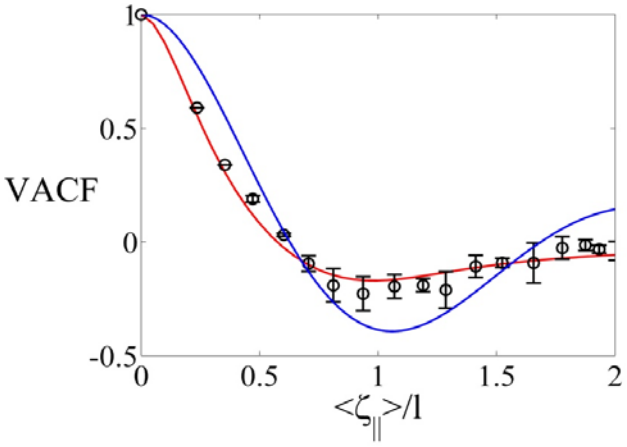

Figure 27: Transverse VACF as a function of normalized mean displacement for the LB simulated foam pore structure (red line), 110 PPI NMR data (open circles), and exponential memory function model with l = 250μm (blue line)

The negative lobe of the VACF in Figure 27 is a result of tracer particles having a transverse velocity orientation at time t opposite of their original transverse velocity orientation. The low point of the VACF corresponds to the high point of the diffusion coefficient curve. The model curve shown in Figure 27 (blue line) oscillates more strongly than the data. From the frequency

sum rules: $\mathrm{VACF}\big|_{t\to\infty} = 1\text{-}t^2\omega_v^2$, it is obvious from Figure 27 that the model fit underestimates the second frequency moment or restoring force, ω_v^2. Accessing this short time domain to accurately measure ω_v^2 is impractical with the single PGSE experiment; however with the frequency modulated PGSE NMR method [104], ω_v^2 can be measured directly as the second moment of the resulting VACF frequency distribution.

Physical Interpretation of the Dynamic Length Scale Using a Toy Model

To help interpret the physical meaning of the dynamic length scale defined above, this section presents an elementary toy model of backscattering dynamics. The dynamics discussed in this section result from particles moving at a fixed tangential velocity along a sinusoidal path, see Figure 28.

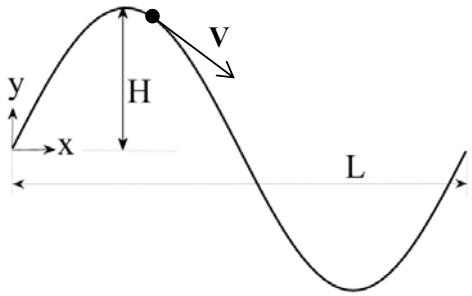

Figure 28: Sinusoidal path of the toy model

For the sinusoidal path the *y*-coordinate in terms of the *x*-coordinate is

$$y = H \sin(2\pi x/L) \qquad (4.22)$$

and the *y*-coordinate velocity in terms of the *x*-coordinate velocity is

$$v_y = v_x (2\pi H/L) \cos(2\pi x/L) \qquad (4.23).$$

The *x*-coordinate velocity in terms of *x* is

$$v_x^2 = V^2 \Big/ \left[1 + \left[(2\pi H/L)\cos(2\pi x/L)\right]^2\right] \quad (4.24).$$

The arc length between two *x*-points is

$$S_{1-2} = \int_{x_2}^{x_1} \sqrt{1+\left[(2\pi H/L)\cos(2\pi x/L)\right]^2}\,dx \quad (4.25).$$

Constant tangential flow velocity along the sinusoidal path requires that the time to travel an arc length *S* is $t = S/V$. Due to the analytical difficulty of solving Eqn. (4.25) for the *x*-coordinate in terms of time and starting position, the equations are solved numerically in MATLAB (see Appendix B) for the mean transverse variance, VACF, and effective diffusion coefficient as a function of mean displacement; see Figure 29.

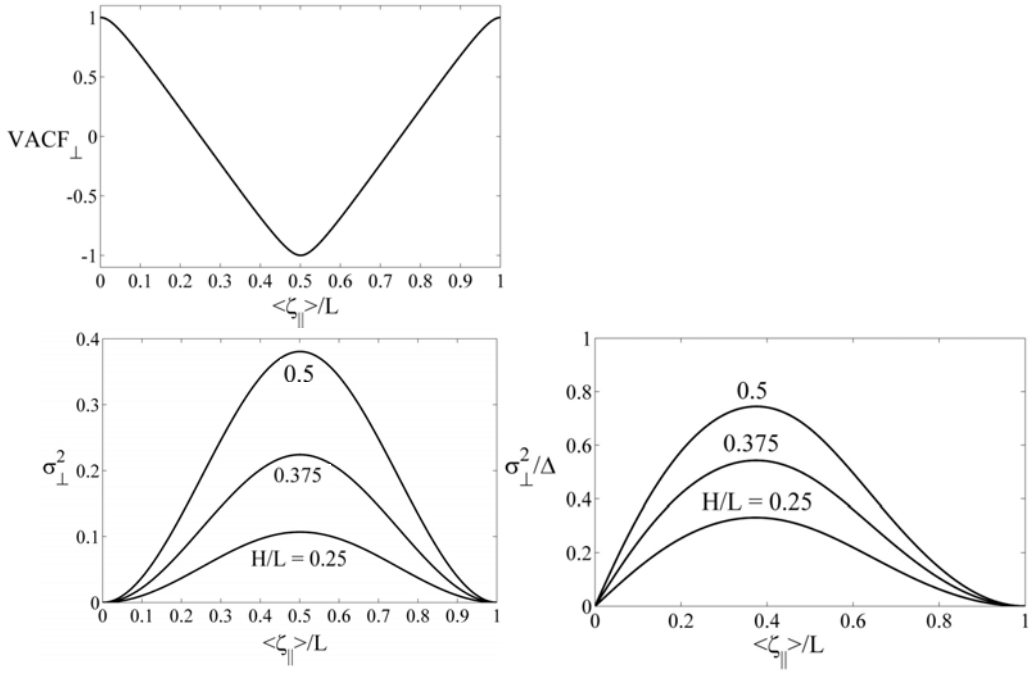

Figure 29: Transverse correlation functions of the sinusoidal toy model

The first critical point of the transverse variance and VACF occur at a mean displacement of exactly half the sinusoid wavelength: 0.5L. The diffusion coefficient critical point occurs at a mean displacement of 0.375L. This analysis tends to support the conjecture posed above in which it was stated that the diffusion coefficient maximum or VACF minimum occurs at a mean displacement of half the primary axial oscillation wavelength. This is an interesting fact because it suggests the ability to measure the physical dimensions of a streamline path by observing time-correlation dynamics. The streamline dimensions of flow in porous media are a reflection of the pore structure itself. Therefore this analysis suggests the opportunity to resolve a pore structure through the streamline path via the time correlation functions of transport. The total information content of the first order correlations, *e.g.* average VACF, and higher order correlations, *e.g.* non-local dispersion tensor, as they relate to the physical dimensions of a streamline path remains an unexplored concept.

Asymptotic Dispersion Dynamics

Definition of a characteristic length scale now allows for scaling of the asymptotic dispersion coefficients with Peclet number. Shown in Figure 30 are the scaling of the axial and transverse asymptotic dispersion coefficient with Peclet number for the 110PPI foam and 80PPI foam. The asymptotic coefficients are determined by measuring the linear slope of the long time limit variance.

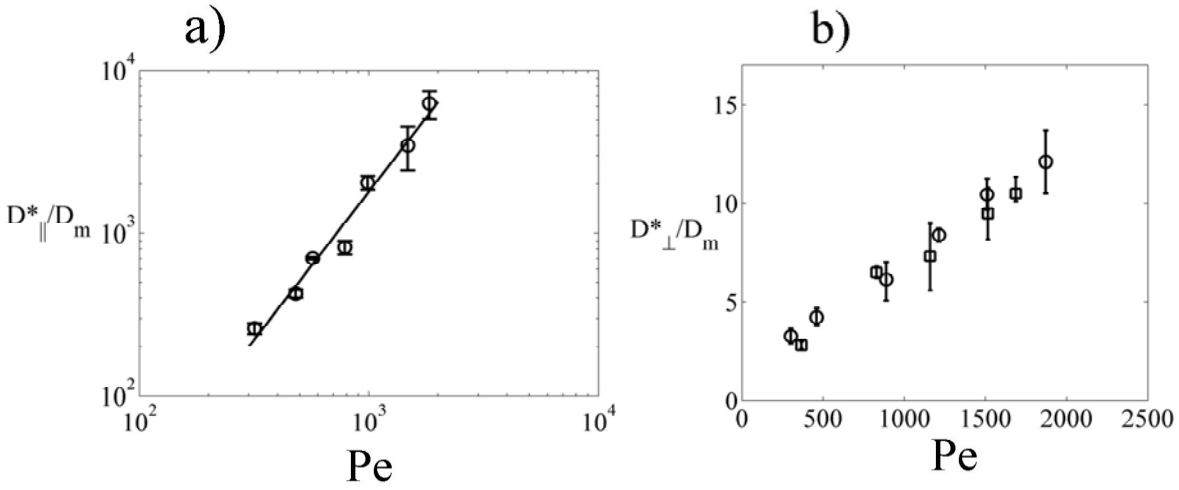

Figure 30: Asymptotic dispersion coefficient as a function of Peclet number (based upon the correlation length *l*) a) axial coefficient for the 110PPI foam b) transverse coefficient for the 110PPI (open circles) and 80PPI foam (open squares), $D_m = 2\text{x}10^{-9}$ m^2/s

As expected the asymptotic transverse dispersion coefficient scales linearly with Peclet number. For a given Peclet number the transverse coefficient of foam is significantly reduced compared to a monodisperse packed bed. A power law fit to the asymptotic axial dispersion coefficient of the form Pe^{α}, with $\alpha = 1.82$, is over-layed on the axial data in Figure 30. For pure diffusive mixing $\alpha = 2$ while for pure mechanical mixing $\alpha = 1$. Given the highly open nature of the 110PPI foam structure one might expect a power law exponent more similar to diffusive mixing. The reduced scaling of the transverse dispersion coefficient (compared to monodisperse packed beds) supports the observation of reduced mechanical mixing. For transport applications this result is significant because it can help to quantify the relative balance of permeability (or other statistics) and dispersion relative to alternative structures such as monodisperse packed beds.

Conclusion

This chapter presented a survey of experimental and numerical data analyzing dispersion in polymer cellular foam. The characteristic length scale of cellular foam structures was defined by a length scale inherent to the stochastic dynamics of transport within the open space of the structures. This efficient measurement of length scale is a significant improvement over previous *ad hoc* image analysis techniques in part because the definition and measurement coarse grains all structure statistics. The definition made in this work, $l = \left\langle \zeta_{\|} \right\rangle \Big|_{dD_{\perp}/d\Delta=0}$, agrees well with the PPI parameters provided by the manufacturer. It is important to note that the definition of length scale is in part an ill-posed concept; there are in fact many potential length scales that can act as a universal scaling parameter. Higher order correlations, such as the nonlocal dispersion coefficient […], can reveal similar length scales in transport dynamics. However for practical applications the simplest and most robust measurement method is often the most appealing. From this perspective the single PGSE measured dispersion coefficient is a highly attractive approach. When considering cellular structures for transport applications one must weigh the importance of mechanical mixing to the relative advantages (*e.g.* high permeability). The data in Figure 30 will help decide if foam structures are indeed the ideal structure for transport applications.

TRANSPORT OF COLLOIDAL PARTICLES IN AN OPEN CELL POLYMER FOAM POROUS MEDIA

Introduction

The flow and transport of a colloidal suspension through a porous material is an important process found within a broad range of disciplines, spanning geophysics, engineering, and medicine. The importance of colloid-related (*e.g.* microbe, radio-nuclide, etc.) transport in the subsurface has motivated much theoretical and experimental work focused upon understanding the mechanisms of colloid transport and deposition in porous media [105-107]. The practical challenges associated with experimentally observing the transport of colloids in opaque media have relegated past studies to classic breakthrough-type methods [63, 65, 108]. The purpose of this work is to present results from nuclear magnetic resonance (NMR) measurements of a moderate concentration (ϕ = 0.15), hard sphere (mean particle radius of R = 1.25μm), colloidal suspension transport through a high porosity open-cell polymer foam. The use of cellular foam as the porous media is motivated by the desire to prevent complete blockage of flow paths and also the ubiquity of the structures in technological and biological media *e.g.* sponges, trabecellular bones, filters[67]. The application of NMR in the study of colloid suspension transport in porous media allows for the non-invasive, phase-resolved observation of transport dynamics [66, 109] and therefore marks a significant advance in the experimental study of suspension transport in porous media.

Nuclear magnetic resonance has proven to be a valuable non-invasive tool for probing the spatial and temporal dynamics of single phase transport in porous media [110]. The

technique is an ideal experimental method in the sense that the liquid molecules of the advective velocity field within the pore space are the tracer particles. The measurements are therefore free of entrance effects and require no assumptions regarding the governing mass transport equation inherent to break through curve methods. The recent development of manufacturing core shell oil filled particles [111] has allowed for the separation of liquid and solid-phase dynamics in NMR measurements of colloidal suspensions [34, 109, 111, 112]. The proven application of NMR in the study of single phase transport in porous media coupled with the recent developments in NMR-active core shell colloidal suspensions have established all the experimental details necessary to directly probe the transport of colloidal suspensions in porous media.

The experimental observations in this work are limited to the long time limit of colloid transport; times much greater than the transient so-called "clean-bed removal" filtration phase [106]. As will be later demonstrated, in this "stationary" regime the interplay of colloid attachment and flow has equilibrated so that the solute and colloid dynamics are steady state. Colloidal particle dynamics in porous media are typically subcategorized into *transport* (*flow*) and *attachment* steps [63]. As a probe of these dynamics the value of NMR lies partially in the ability to discern the behavior of the subcategories through temporally resolved molecular displacement dynamics, *i.e*. the propagator of motion [30]. The temporal observation of coarse grained attachment dynamics provides an indication of the means through which the various chemical-colloidal-surface interactions [113, 114] impact attachment and is therefore useful for testing conceptual models. Analogously, the temporal observation of flow or transport dynamics provides a platform through which one can investigate the potential influence of non-Brownian

colloidal flow effects; *e.g.* colloid-colloid hydrodynamic interactions, inertia, and shear induced migration [115, 116]. The ability of NMR to discern the sub-categories of dynamics provides important information regarding the pore scale dynamics which generate the macro-scale transport behavior; information which is otherwise lost in the inherent coarse graining of classical methods.

Materials and Methods

Materials and Hardware

Polyurethane open-cell foam (Foamex, Inc.) was used as the porous media. The foam has a porosity of 97% and an approximate average pore size of 110PPI (pores per inch). The PPI designation given by the manufacturer is an approximate characterization of the pore structure. An 8x8x150mm rectangular column of foam was sealed at the four outer faces using adhesive backed PEEK tape and epoxy. The NMR transport experiments were conducted on a section of the foam sample 2/3 of the column length from the inlet.

The NMR experiments were conducted on a Bruker super-wide bore 300MHz magnet with a Micro2.5 magnetic field gradient probe containing a 15mm birdcage coil and networked to a Bruker Avance III spectrometer with gradient controls. The gradient set is capable of producing orthogonal magnetic field gradients up to 1.5T/m.

The transport experiments began by flushing the sample with de-ionized water (Millipore, Inc.) for about 12 hours at a mean flow velocity of 20 mm/s using a peristaltic pump (Masterflex, Inc.). Transport measurements of pure water flow from a Pharmacia P500 pump were then taken for comparative purposes. After the pure water measurements were finished the

sample was preequilibrated with the colloidal suspension through 6 hours of continuous up-flow at a mean flow velocity of 1 mm/s. During flow, the reservoir of colloidal suspension was slowly mixed using a magnetic stir bar to prevent aggregation or creaming. The flow of colloidal suspension was driven by a programmable syringe pump (KDS Scientific, Inc.) interfaced to a 50ml glass syringe (Hamilton, Inc.).

The core-shell oil particles were constructed using the method of Loxley and Vincent [111]. A short review of the technique follows. An oil-phase containing 3.0 g of poly(methyl-methacrylate) (PMMA) MW 350,000, 60 ml of dichloromethane, 3.8 ml of acetone and 5 ml of hexadecane was added drop-wise to 80 ml of a 2% wt. polyvinyl alcohol (PVA) solution while being stirred with a Heidolph Silent Crusher M homogenizer. To obtain the desired particle sizes a constant shear rate of 12,000 rpm was applied for a period of one hour following the oil-phase addition. The resulting emulsion was then added to 120mL of a 2% wt. PVA solution and the volatile solvent was allowed to evaporate overnight resulting in a PMMA shell encasing the oil, thus separating the oil and water phases. The microspheres are short range repulsive due to short chain PVA molecules which adhere to the surface and exhibit hard sphere behavior [117]. The resulting particle size distribution was estimated from light microscopy images of the suspension. A custom edge-detection image analysis program was used to extract the particle diameters from optical suspension images, see Figure 31. The results from light microscopy were corroborated by an equivalent analysis of Field Emission Microscopy (FEM) images.

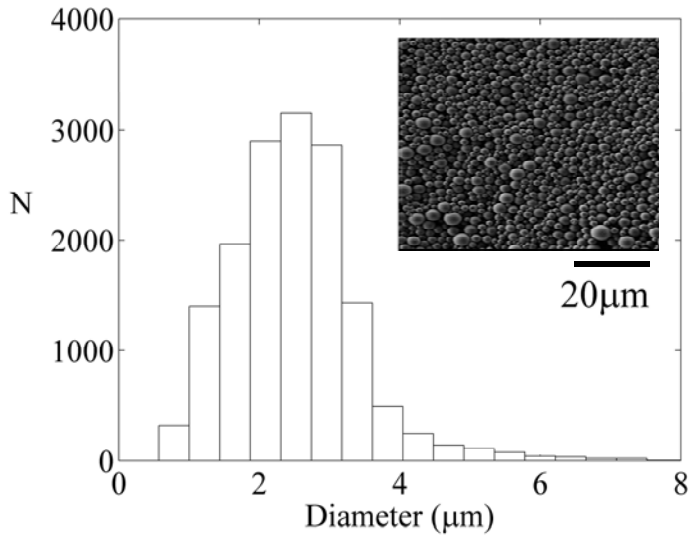

Figure 31: Size distribution of the colloidal suspension, mean diameter = 2.5μm, inset: FEM colloidal suspension image

The suspension dynamics studied in this work are limited to a colloidal volume fraction of ϕ = 0.15. To arrive at a precise volume fraction the unprocessed suspension was centrifuged (Sorvall, Inc.) at 8,000 rpm and 15,000 rpm for 10 minutes each. The resulting concentrated phase was then re-suspended to the desired volume fraction. To measure a precise volume fraction capillary tubes filled with the suspension were centrifuged (IEC, Inc.) and the resulting relative heights of the concentrated phases were used to quantify a precise volume fraction.

Results and Discussion

Spatially Resolved Velocity Images

Spatially resolved maps of the flow-direction velocity were measured for both pure water and the colloidal suspension, see Figure 32. Figure 32 a) & b) were obtained under identical mean flow speeds and experimental parameters. The colloidal suspension velocity image was

obtained following approximately 12 hours of continuous pumping. The chemical shift of the colloidal suspension due to the presence or oil and water created a read-direction artifact in Figure 32a). The artifact is visible in the shifted edge on the right-hand side of Figure 32a). The velocities of the colloidal suspension image are therefore partially weighted by a spatial correlation with neighboring pixels. As a result of the artifact the distribution of flow velocities in the colloidal suspension image appears to narrow.

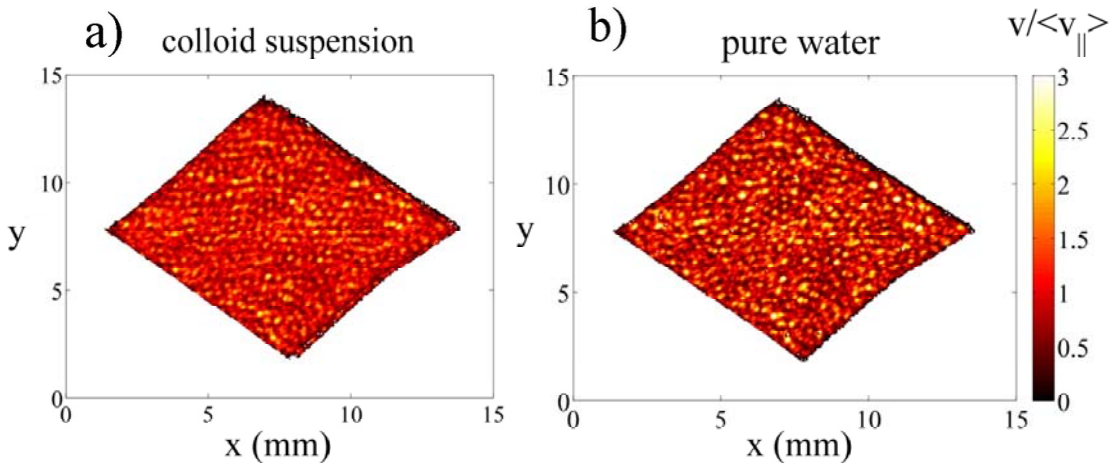

Figure 32: Spatially resolved images of the flow direction velocity within the foam sample for pure water (left) and 15% colloid suspension (right), image resolution is 60x60x1000µm/pixel, $\langle v_{||} \rangle$ = 250µm/s, acquisition time was 30min, the colloidal suspension image is weighted by a chemical shift artifact

Neglecting the image artifact, the colloidal suspension and pure water images of Figure 32 have qualitative similarities. Regions of high velocity in the pure water image are also regions of fast velocity in the colloidal solution. Measurements on an AR-G2 rheometer (AR Instruments, Inc) demonstrate the 15% colloidal suspension behaves as a Newtonian fluid over a wide range of shear rates. Therefore, neglecting any structural changes due to particle deposition one would expect the flow profile of the colloidal suspension and pure water to be equivalent. The

qualitative similarity of Figure 32 suggests that any changes in the pore structure from particle deposition occur at a local pore scale in contrast to regional or macro-scale changes.

Displacement Propagator Dynamics

The temporal evolution of the displacement propagator, $\overline{P(\mathbf{R},\Delta)}$, was measured as a function of observation time for both pure water and the colloidal suspension. The propagator for each phase of the colloidal suspension was obtained by integrating the spectral dimension of the two dimensional Fourier transformed signal over the water and oil peaks thus providing the propagator for the suspended particle solid phase (oil) and the suspending liquid phase (water). The phase resolved axial and transverse displacement propagators of the colloidal suspension are compared in Figure 33 for a mean flow velocity of 1.0 mm/s at several displacement observation times. The data in Figure 33 was obtained following 6 hours of continuous suspension flow.

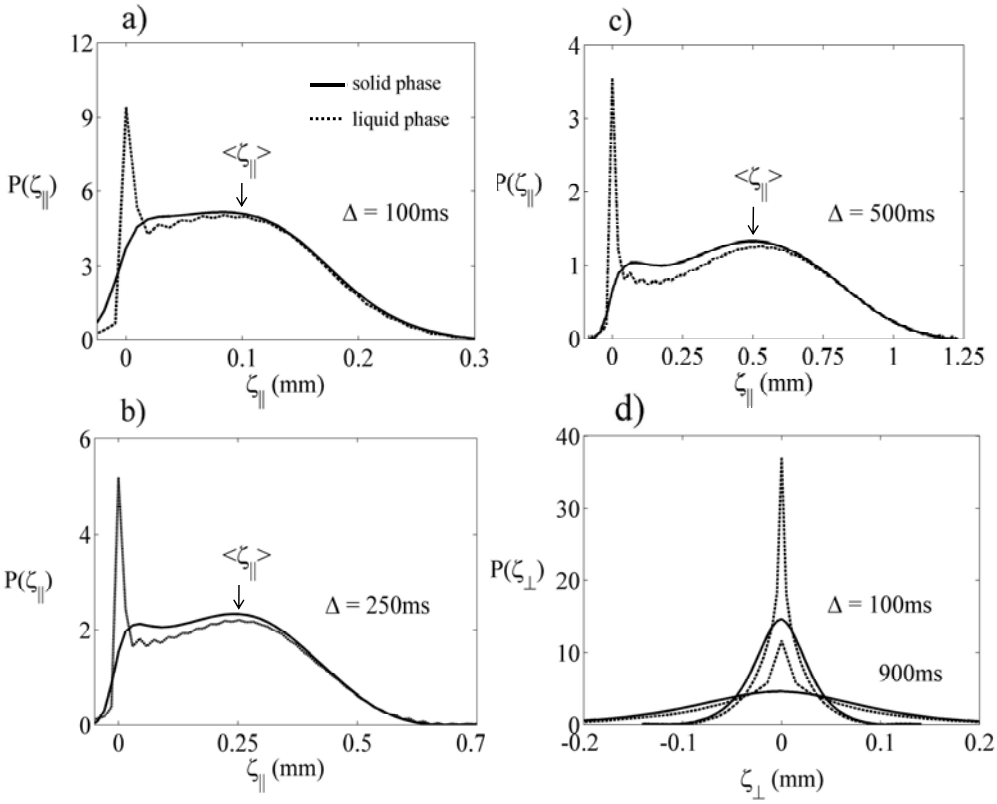

Figure 33: Average propagator temporal evolution of the water liquid phase (solid line) and oil particle solid phase (dashed line) of the colloidal suspension at a mean flow velocity of 1 mm/s; a)-c) axial propagators, d) transverse propagators

The axial propagator of the colloidal suspension solid-phase, Figure 33a)-c), contain a significant portion of the population near $\zeta_{\parallel} = 0$, indicating hold-up of colloidal particles. The large displacement behavior of the solid-phase propagators appear similar to the liquid-phase however there is a difference in the liquid and solid phase axial displacement propagators at moderate displacements, between $\zeta_{\parallel} = 0$ and the mean displacement ($<\zeta_{\parallel}>$). The transverse displacement propagator of the solid-phase, Figure 33d), contains a significant portion of the population near $\zeta_{\perp} = 0$ while the liquid-phase appears nearly Gaussian over the range of displacements. Despite hold-up of colloidal particles the mean flow velocity of the colloidal

suspension solid and liquid-phase are equivalent over a broad range of mean flow speeds, see Figure 34. The flow speed is calculated from $\langle v_{\|} \rangle = \langle \zeta_{\|} \rangle / \Delta$.

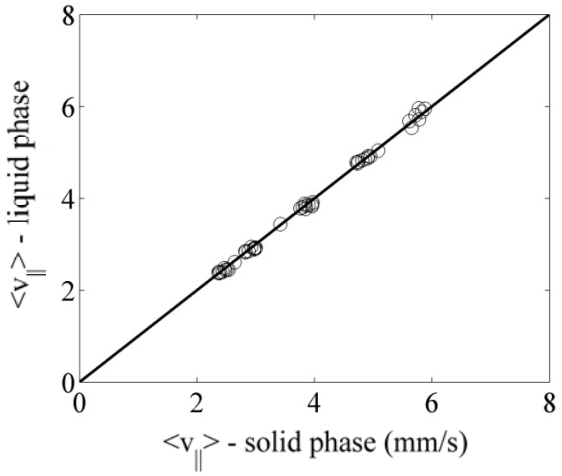

Figure 34: Relative flow velocities of the colloidal suspension solid and liquid-phase

Shown in Figure 35 is a comparison of the colloidal suspension liquid-phase and pure water axial propagators at a mean flow velocity of 1mm/s. Also shown in Figure 35b) is a comparison of the colloidal suspension axial propagator at a fixed observation time following 6 and 24 hours of continuous flow. The equivalence of the axial propagators in Figure 35b) suggests the dynamics of the colloidal suspension to be steady state, *e.g.* invariant to the beginning of time.

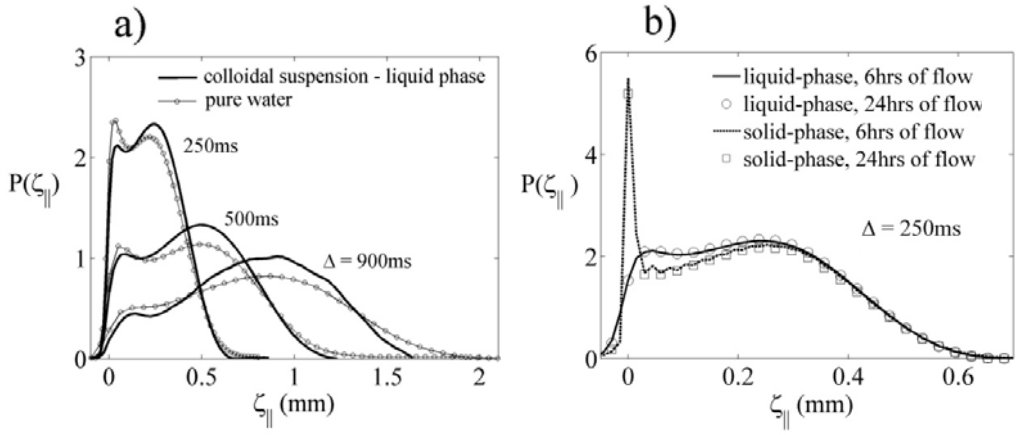

Figure 35: Axial propagator temporal evolution of the phase resolved colloidal suspension and pure water at a mean flow velocity of 1 mm/s a) single-phase water and colloidal suspension liquid-phase axial propagator b) colloidal suspension axial propagator following 6 and 24 hours of continuous flow

The axial propagators of pure water, see Figure 35a), are characterized by a fast moving bulk population and smaller population of slow flowing molecules near $\zeta_{\|} = 0$. In comparison, the axial propagator of the colloidal suspension liquid-phase contains a greater portion of the population near the mean displacement and the pure water propagator contains a significantly larger high displacement tail at longer displacement times.

Agreement of the solid and liquid-phase axial displacement propagators in Figure 33a)-c) at large displacements, $\zeta_{\|} > \langle\zeta_{\|}\rangle$, suggests similar streamlines of the two phases in regions of high velocity. The difference in the propagators for $\zeta_{\|} < \langle\zeta_{\|}\rangle$ leading up to $\zeta_{\|} = 0$, suggests the existence of a low particle concentration boundary layer near the solid structure consistent with shear induced particle migration [66, 109]. Analogous to flow in a straight tube, the local incoherent motion of colloids is governed not only by Brownian motion but also the complex interparticle hydrodynamic interactions of neighboring colloids and their interaction with the

solid structure. Within a porous media the sequence of interparticle interactions is further confounded by the separation of advective streamlines by mechanical mixing. An intuitive product of the mechanical dispersion dynamics is that particles on adjacent streamlines can only interact for a time period proportional to the time that two streamlines remain adjacent, i.e. $\tau \alpha l/\langle v_{||} \rangle$, where l is the characteristic length of the media and τ is the characteristic relaxation time of the advective dynamics. Furthermore a time varying flow direction and speed along a given streamline introduces the possibility of inertial effects impacting colloid movement. Relative to the liquid-phase, colloids moving at high speed would respond less quickly to abrupt changes in the flow direction. Further work is required to fully isolate and understand the various mechanisms of active colloid transport in the complex advective flow fields within porous media.

The axial propagator disparity between pure water and the colloidal suspension liquid-phase, seen in Figure 35a), suggests dissimilar advective velocity distributions due to dissimilar pore structure. Transformation of the pore structure is the result of colloidal deposition on and near the solid structure. The hold-up of colloidal particles near the solid pore structure introduces an additional suspension dispersion mechanism to the intrinsic dispersion of the pore structure. A fraction of the colloidal particle population must wait a time period before continuing advective transport through the structure. The hold-up mechanism will contribute to the asymptotic solid-phase dispersion coefficient like $Pe\ln(Pe)$[58, 101]. The process of exchange between the flowing and stagnant colloids can be quantified through the stagnant fraction of the solid-phase population. The immobile fraction of the solid-phase population can be determined from the $q = 0$ intercept of a linear fit to a Stejskal-Tanner plot, $\ln|S|$ vs. $4\pi^2 q^2(\Delta$-

δ/3), of the PGSE signal at high *q*, Figure 36a). The immobile fraction can also be estimated from the cumulative distribution function of the axial displacement propagator; i.e. the area underneath the hold-up peak [118]. Figure 36b) shows the stagnant fraction of the solid-phase population as a function of observation time for a mean flow velocity of 1 mm/s estimated from the high *q* behavior of the Stejskal-Tanner plot and the cumulative distribution function of the axial propagator evaluated to a displacement of $\zeta_{||} = 0.04$mm.

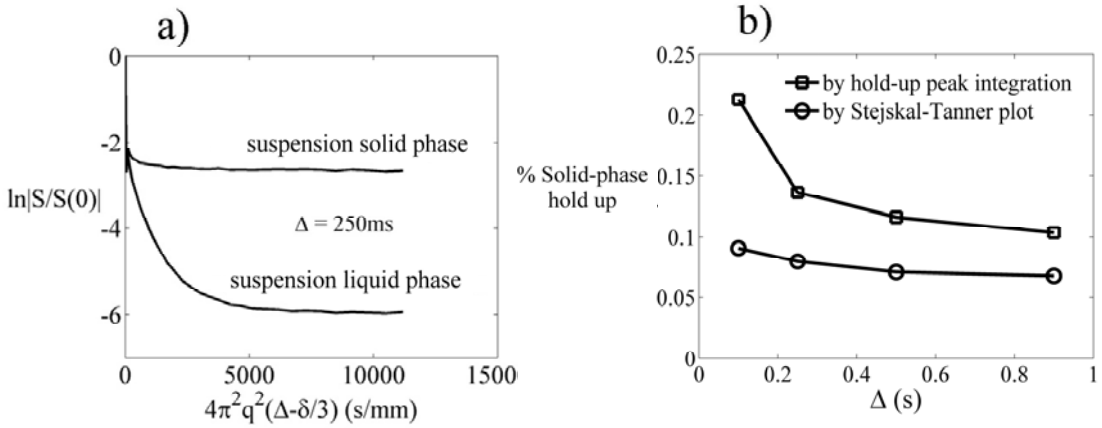

Figure 36: Colloidal suspension axial dynamics for $\langle v_{||} \rangle$ = 1mm/s a) phase-resolved Stejskal-Tanner plot of the PGSE signal amplitude for Δ = 250ms b) immobile fraction of the solid-phase as a function Δ, estimated by integrating the propagator under the hold-up peak and also from the high *q* behavior of the Stejskal-Tanner plots as in a)

The initial, Δ < 0.4s, rapid decline of the solid-phase immobile fraction in Figure 36b) suggests a portion of stagnant colloids undergo fast exchange with the flowing population, *e.g.* colloids very near the stagnant fluid surface. The slow decline of the stagnant solid-phase population for Δ > 0.4s indicates a slow exchange population, *e.g.* colloids trapped within stagnant or recirculation volumes or fixed to a surface. The scaling of the data in Figure 36b) is therefore an indication of the various mechanisms responsible for solid-phase deposition and therefore the functional form of the stagnant population wait time.

Time Dependent Dispersion Dynamics

The following discussion will now focus upon the time dependent dispersion of the colloidal solution. The variance or second moment, σ^2, of the displacement propagator can be determined from a low q fit to the PGSE signal amplitude. A time dependent dispersion coefficient is defined as the variance divided by the observation time, $D = \sigma^2/(\Delta-\delta/3)$. The two quantities share the same information content but in different form. The time dependent phase-resolved variance and dispersion coefficient are shown in Figure 37 for the transverse and axial direction. Images a) & c) contain the axial dispersion dynamics as a function of mean displacement and images b) & d) contain the transverse dynamics. The data shown in Figure 37 was obtained following at least 6 hours of continuous flow.

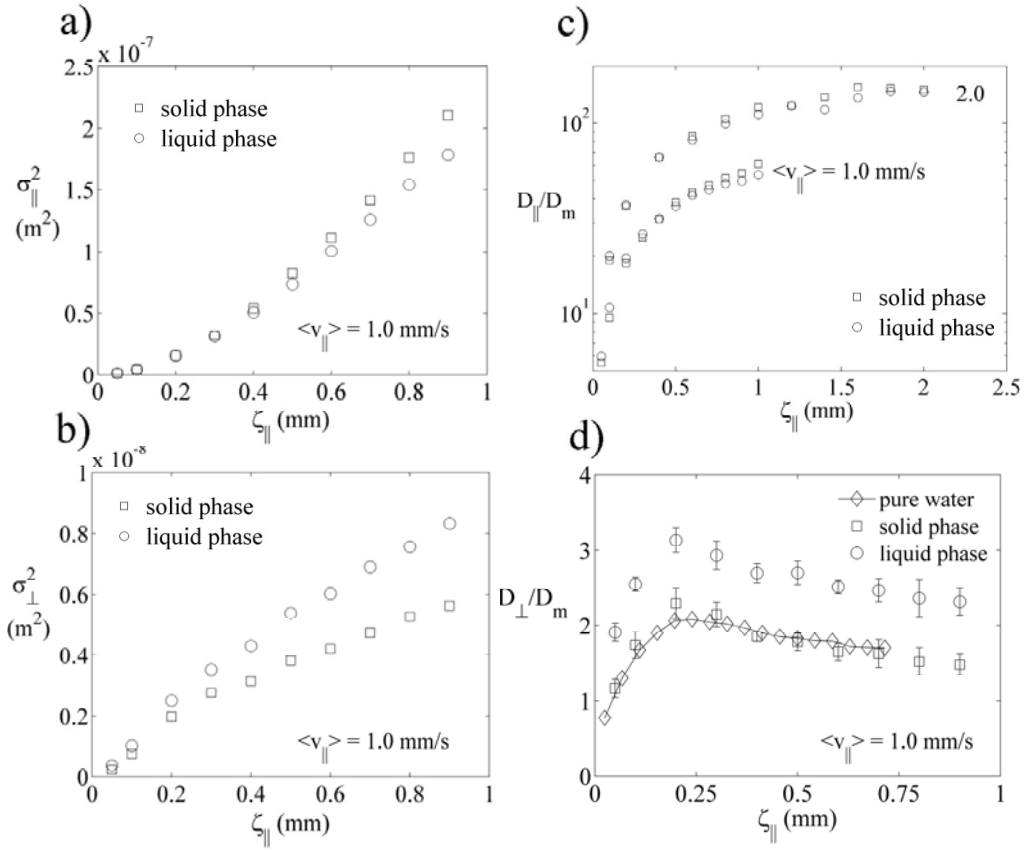

Figure 37: Phase resolved axial and transverse dispersion dynamics of the colloidal suspension within the foam pore structure, a) & b) axial and transverse displacement variance as a function of mean displacement for a mean flow velocity of 1mm/s, c) & d) axial and transverse effective dispersion coefficient as a function of mean displacement, $D_m = 2\text{x}10^{-9}$ m^2/s, also shown in d) are the dynamics of pure water at a mean flow velocity of 1mm/s

The linear growth of the axial and transverse variance, see images a) & b), at high observation time, $\zeta_{\|} > 0.6$mm, suggests the existence of a unique asymptotic dispersion coefficient for both phases. To our knowledge these are the first measurements directly demonstrating this behavior of a colloidal suspension in a porous media. At long times the axial variance of the colloidal suspension solid-phase grows faster than the liquid-phase variance. This is plausible considering the additional hold-up mechanism impacting the solid-phase dynamics. There is a transition

point in the axial dynamics before which the liquid-phase axial dispersion is greater than the solid-phase, see image c). This short time difference is the result of a number of potential factors including the significantly greater molecular mobility of the liquid-phase and also perhaps a greater scattering of the liquid-phase throughout the advective velocity field. In contrast the liquid-phase transverse dispersion is consistently greater than the solid-phase dispersion. The *backscattering* effect seen in the transverse dispersion dynamics of both phases, see image d), is the result of oscillatory streamlines within the structure. Within the backscattering dynamics there exists a "fingerprint" of the solid pore structure, see chapter 6. For pure water, at high Peclet number, the maximum of the transverse dispersion curves occur at a fixed mean displacement of l = 250μm; a number which is on the order of the half wavelength of the axial oscillations of streamlines within the pore space. This fixed displacement is a characteristic length of the structure[119] and will be used in the Peclet number definition later in the text.

The colloidal solution transverse dispersion dynamics are qualitatively similar to the pure water dynamics. However the liquid-phase transverse dispersion magnitude is significantly enhanced relative to the solid-phase and pure water dispersion, see image d). The enhanced transverse dispersion of the liquid-phase relative to the solid-phase is the result of a number factors including the greater molecular mobility of the liquid-phase, hold-up of solid-phase near $\zeta_{\perp} = 0$ and possibly migration of flowing colloids into less mechanically driven regions (e.g. away from the solid pore structure). The enhanced transverse dispersion of the liquid-phase relative to pure water however is an indication of the change in pore structure and the resultant effects on the advective flow profile. In general the comparison made in image d) indicates the liquid-phase experiences enhanced mechanical mixing relative to the solid-phase and pure water.

Asymptotic Dispersion Dynamics

The amalgamation of effects stemming from deposition of colloids on the pore structure and particle-particle, particle-structure interactions, and inertia are manifested in the asymptotic dispersion coefficients of the colloidal solution. The phase-resolved axial and transverse asymptotic dispersion coefficients are plotted in Figure 38 as function of Peclet number. The Peclet number was varied by adjusting the mean flow velocity. In the advection dominated regime, i.e. Pe>100, classical dispersion theory predicts a power law scaling of the asymptotic axial dispersion coefficient with Pe[120]. Power law fits to the axial asymptotic dispersion coefficients are therefore also shown in image a). For purely Taylor dispersion the asymptotic axial dispersion coefficient scales like Pe^2 while for purely mechanical mixing the coefficient scales like Pe and hold-up dispersion contributes like $Pe\ln(Pe)$. The asymptotic coefficients shown in Figure 38 were determined from the long time behavior of D as a function of time, similar to the so-called effective dispersitivity[121], rather than fitting a linear curve to the long time behavior of the variance. Therefore the asymptotic coefficients shown in Figure 38 retain pre-asymptotic information such that the axial coefficients are underestimated while the transverse coefficients are overestimated.

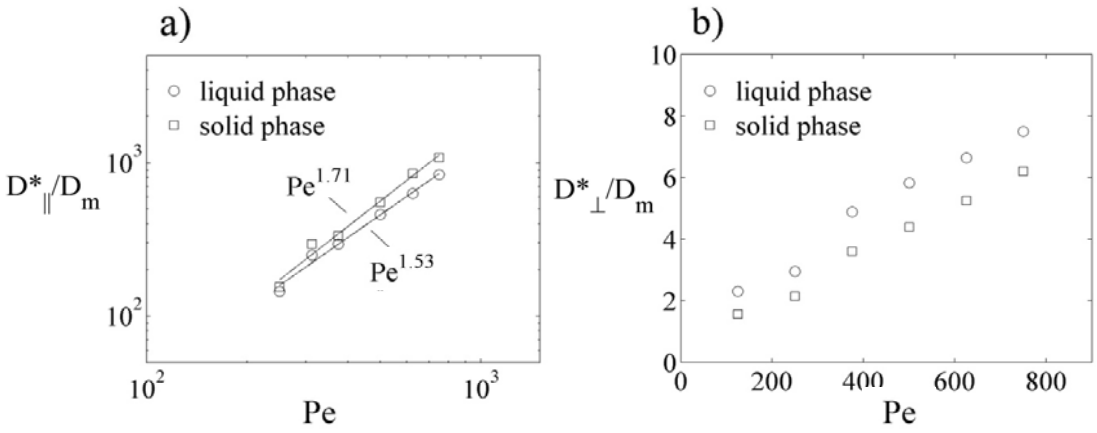

Figure 38: Phase resolved axial and transverse asymptotic dispersion coefficients of the colloidal suspension as a function of mean flow velocity (non-dimensionalized in the Peclet number), $D_m = 2\text{x}10^{-9}$ m^2/s

The asymptotic axial dispersion coefficient of the colloidal solution solid-phase was found to scale like $Pe^{1.71}$ while the liquid-phase was found to scale like $Pe^{1.53}$; for pure water the coefficient scales like $Pe^{1.81}$ (determined from a linear fit to the long time variance). Therefore, as mentioned in the earlier transverse dispersion discussion, the dynamics of the colloidal solution liquid-phase are more significantly driven by mechanical effects then either the solid-phase or pure water dynamics. The solid-phase dynamics however appear more like Taylor dispersion. From an earlier analysis of the axial propagators one is able to conclude that the solid-phase experiences the mechanical effects which govern the liquid-phase dynamics; however these effects are offset by the hold-up mechanism and possible particle migration. As a result the solid-phase coefficients in Figure 38 appear more similar to Taylor dispersion then the liquid-phase.

Conclusion

The active transport of a colloidal suspension within cellular foam was probed using nuclear magnetic resonance. The dynamics of both the liquid and solid-phase of the suspension were presented over a range of observation times and mean flow velocities. The deposition of colloidal particles onto the solid pore structure were shown to cause a transformation of the solid pore structure which in turn alters the macro-scale dynamics of both phases relative to single phase transport. The modeling of colloid transport in porous media should therefore consider the pore structure transformation effects of colloid deposition and the resultant variation in the macro-scale dynamics. The various phenomenon presented in this work are limited to a specific structure and surface chemistry and should therefore cautiously be interpreted when considering the dynamics within other media. The mechanisms of colloid deposition in high porosity polymer cellular foam are not the mechanisms one would expect in a lower porosity granular media exhibiting different physical and chemical surface characteristics. However the results in this work mark an important first step. The advantageous capabilities that NMR provides in regard to the study of colloid transport in porous media will surely be valuable in the ongoing process of model development and experimental verification.

MAGNETIC RESONANCE MICROSCOPY ANALYSIS OF TRANSPORT IN A NOVEL TAPE CAST POROUS CERAMIC

Introduction

Recent advances in ceramic processing technology have introduced the ability to produce spatially evolving pore structures in which the pore dimensions exhibit one dimensional affine characteristics [122]. These complex pore structures suggest the opportunity to design ceramics with unique transport properties for many industrial applications including fuel cells, filtration, and catalyst supports. However, the detailed nature of these pore structures including inter-pore connectivity has yet to be established. This experimental study utilizes nuclear magnetic resonance (NMR) transport measurements to probe the characteristics of the freeze tape cast ceramic pore structure and induced transport phenomena defining this new class of ceramics with engineered porosity.

Nuclear magnetic resonance microscopy is well suited to the study of opaque porous structures because of the ability to easily obtain information concerning the dynamic behavior of a fluid or gas occupying the pore structure [123, 124]. The magnetic basis of information transmission in an NMR experiment overcomes the material opacity constraint of many optically based methods historically used to study porous materials. Furthermore, NMR methods offer the ability to spatially resolve data. The spatial resolution capability is particularly attractive to this study because the ceramic samples exhibit spatial scaling of the pore structure as mentioned above.

The majority of literature relating to NMR based studies of ceramic materials focus upon either solid state type measurements [125] or image intensity based measurements [126-129]. In parallel with these efforts an array of NMR methodologies, *e.g.* gas diffusion and fluid transport techniques, have been developed which can be used to study porous materials[102, 110, 123, 124, 130, 131]. These NMR techniques and others have emerged as powerful tools used in the study of structural and transport characteristics of classic porous media, *e.g.* mono-disperse bead packs [32, 131-133]. This article expands the application of these NMR transport techniques to the structural characterization of the novel ceramics with heterogeneous pore structures.

This chapter will overview the manufacturing process of freeze tape cast ceramic structures and the experimental NMR methodologies in section one. Section two reports the experimental results involving a range of spatially resolved and bulk NMR measurement and the resultant analysis of the data to determine both structural pore information and transport dynamics. Section three provides concluding remarks focusing on the potential to design pore structures for controlled dynamics.

Freeze-Tape-Cast Ceramic Pore Manufacture and Experimental Methods

The porous structures of interest to this study are manufactured using a novel freeze tape casting procedure [122]. The ceramic material selected is yttria stabilized zirconium oxide (YSZ). Traditional tape cast pore-forming techniques used in the manufacture of ceramics utilize homogeneously dispersed packing of thermal fugitive compounds [134] (polystyrene, carbon, etc.). The ability to control the pore structure of these traditional tape cast ceramics is governed by the morphology of the pore former (*i.e.* spherical, acicular, etc.) and the orientation

and distribution of the thermal fugitives in a suspension, thereby limiting the precision and complexity of the pore structures that can be obtained. In addition, the drying process limits the tape thickness due to settling and drying stresses yielding cambered substrates and undesirable density gradients. Freeze casting methods have been recognized as a methodology to produce ceramic pore structures not possible with traditional casting methods [135-137], including graded and columnar pore morphologies in a single processing step. However due to the complex nature of the casting dies and freezing baths, freeze casting methods are generally considered commercially unviable. The tape casting process used in conjunction with freeze casting methods has been shown to retain the pore-forming control mechanisms of freeze casting methods while expanding the technology to commercially viable casting volumes [122], see **Figure 39**. Freeze tape casting yields long range pore alignment from a controlled nucleation front allowing large area ceramic fabrication with a common pore orientation.

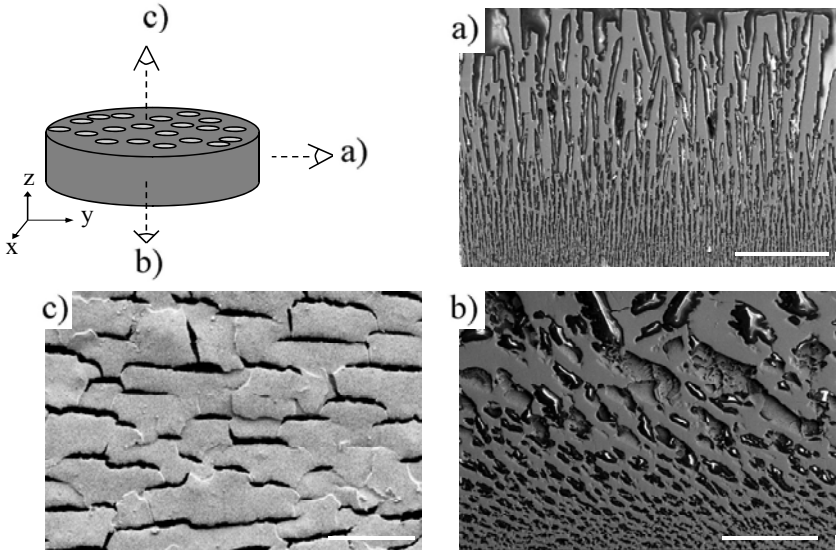

Figure 39: Typical freeze tape cast ceramic pore structure as viewed using SEM microscopy, bar = 400 μm

The SEM images of Figure 39 provide high resolution two dimensional pore scale detail on a limited region of the ceramic. The imaging method requires destructive sampling. Non-destructive magnetic resonance imaging (MRI), though at lower resolution, is not limited by the opaque nature of the ceramic structure. Furthermore, dynamic MRI measurements permit the measurement of transport dynamics within the pore structure, thereby sampling inter-pore connectivity. Magnetic resonance imaging of pore structure is accomplished by measurement of a saturating liquid or gas spin density $\rho(\mathbf{r})$. The resultant image is a pixel intensity map where a given pixel is weighted by the local spin density.

All NMR experiments were conducted on a Bruker Avance DRX spectrometer system with a Bruker Micro5 probe and gradient amplifiers interfaced with a 250 MHz superconducting magnet. A custom designed sample holder was used to rigidly fix cylindrical ceramic samples within a 10 mm birdcage rf. coil for the flow and diffusion measurements. The sample holder was designed to allow flow through a ceramic disk while preventing flow at the disk outer edge. The imaging was conducted on samples in a 10 mm birdcage coil. Several individual ceramic samples were used to generate the experimental data however all ceramic samples were manufactured using YSZ ceramic and an equivalent manufacturing process. The ceramic sample thicknesses varied from 1.0 to 2.5 mm. A Pharmacia P500 syringe pump created the steady laminar flow of octane through the ceramic samples. Octane was chosen because of air desaturation in the ceramic pore structure when using other fluids. The orientation of the ceramic samples was such that Octane flow was always in the direction of divergent pore growth.

Experimental Results and Discussion

Magnetic Resonance Imaging of Freeze Tape Cast Ceramic and PGSE Diffusion Probe of the Pore Structure

The one dimensional affine spatial scaling of the freeze tape cast ceramic pore dimensions is highly visible from magnetic resonance imaging of a Magnevist© doped water saturated ceramic disk, as shown in Figure 40. The images are each a slice of 200 μm thickness from the top Figure 40a) to bottom Figure 40c) of the sample as shown. The in-plane image resolution at each depth is 26 μm by 26 μm. Note the impact of the varying pore size on the water density image. In the large pores near the upper surface, Figure 40a), regions of no signal in the ceramic and strong signal in the pores indicate the spatial averaging scale of 26 μm is smaller than the pore size. Elongation of the pores in a preferred direction at approximately 45º to horizontal is evident. The image clearly indicates the connectivity of the pores in the image plane; information not available from SEM. As the imaged plane is moved down the thickness a blurring of the image results from the partial voluming of the pore water signal and solid ceramic within the 26 μm spatial dimension due to the decreasing pore dimension.

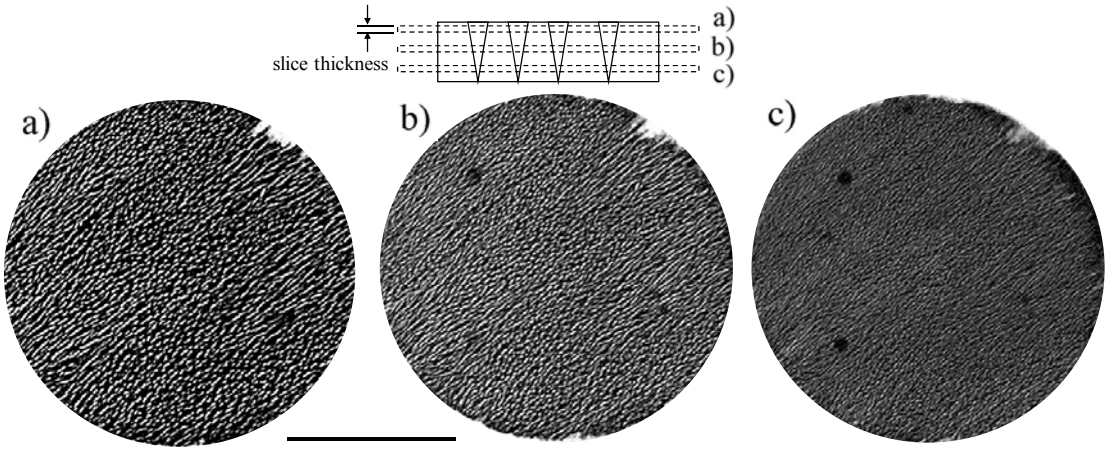

Figure 40: Magnetic resonance imaging of a water saturated YSZ freeze tape cast ceramic disk showing the transition of pore dimensions, slice thickness = 200 μm, 26 x 26 μm/pixel, bar = 2.0 mm

Diffusive spin behavior has been recognized as another method to obtain pore scale information in porous media [124]. Attenuation of the PGSE NMR signal of a saturated porous media under no-flow conditions (assuming weak magnetic susceptibility induced internal magnetic field distortions) is a result of molecular diffusion during the observation time Δ. For a porous media a comparative reduction in the non-restricted diffusion signal attenuation occurs because at sufficient observation times the pore structure restricts the diffusive movement of saturating molecules and therefore reduces the PGSE NMR signal attenuation [6, 35, 123, 124].

Using the one dimensional spatially resolved PGSE sequence a data set quantifying transverse restricted diffusion (perpendicular to the direction of pore growth) in a freeze tape cast ceramic structure was obtained by angular adjustment of a transverse gradient vector, see Figure 41.

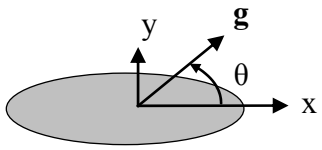

Figure 41: Orientation of the applied gradient vector relative to the transverse pore shape for the single pulse PGSE experiment, plane shown is perpendicular to the main $\mathbf{B_0}$ field and direction of pore growth

The characteristic diffusion time required for spins to sample a pore restriction is given by a^2/D_m **,** where a is the characteristic pore size and D_m is the molecular self diffusion coefficient. The characteristic diffusion length scales with the square root of the observation time $l_d \propto \sqrt{D_m \Delta}$, so smaller pores will have a larger reduction in signal attenuation when compared to larger pores because more spins will have experienced the pore wall restriction. Therefore, for a fixed observation time smaller pore dimensions will result in a lower effective diffusion coefficient. Shown in Figure 42 is the effective diffusion coefficient within a freeze tape cast ceramic from a single pulse PGSE experiment with both angular and one dimensional (parallel to pore growth direction) spatial resolution. Diffusion in the longitudinal direction over the observation time Δ coarsens the spatial resolution in the longitudinal direction. Therefore a relatively short observation time (as compared to the expected transverse diffusive time scales of the structure) of Δ = 30 ms was chosen to minimize spins longitudinal movement while allocating their dynamics to a particular longitudinal location.

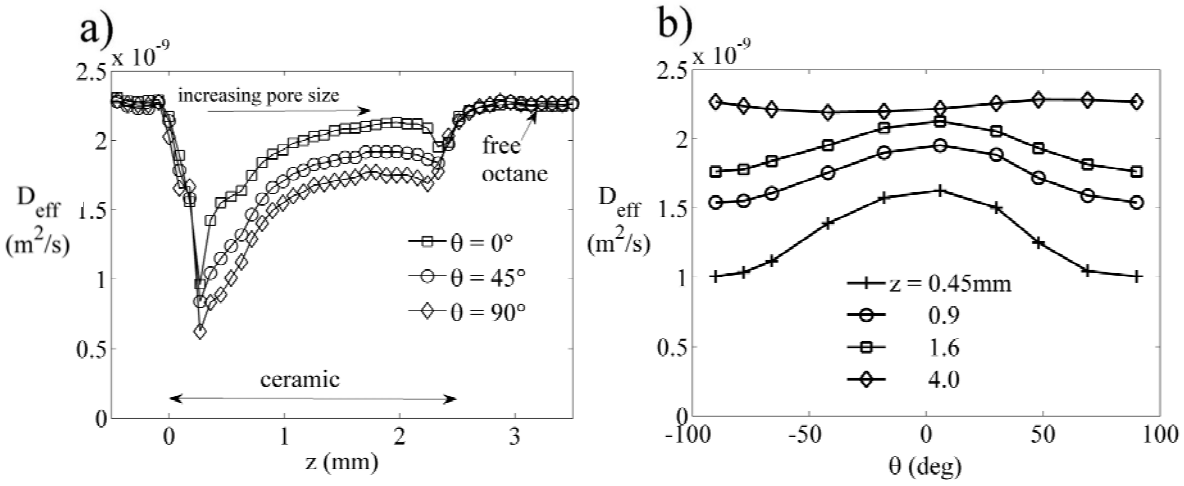

Figure 42: Effective diffusion coefficient from the single pulse PGSE experiment as a function of longitudinal position and transverse gradient vector orientation within a YSZ freeze tape cast ceramic, $\Delta = 30$ ms

The data clearly indicates depth and in plane angular orientation of the average pore structure. Figure 42a) indicates the growth in the average pore size from the small pore region, $z = 0$ mm, to larger pores up to $z = 2.25$ mm. In all three in plane orientations there is a strong restriction of motion (small pore region) at $z = 0.25$ mm with a fairly rapid decay in the z-dimension until a depth of $z = 1.0$ mm, indicating a rapid increase in pore size over this region. For $z > 1.5$ mm the effective diffusion coefficient asymptotes to in plane orientation values below the free molecular diffusion coefficient signaling that pore growth has nearly diminished. Outside of the ceramic structure the effective diffusion coefficient asymptotes to the room temperature self diffusion coefficient of octane 2.35e-9 m^2/s. In Figure 42b) the pore size variation with in plane angular orientation at four depths is shown through the variation of D_{eff}. The depth and angular dependence of Figure 42b) is evident and clearly a strong elongation of the pores can be seen in the three profiles within the ceramic. In the isotropic fluid outside of the ceramic the profile is independent of the gradient orientation as seen in uppermost profile of Figure 42b). The ceramic

is thus heterogeneous in both the depth and radial dimensions. This determination using NMR techniques is non-destructive and describes only the connected open pore structure accessible by liquid penetration.

Spatially Resolved PGSE NMR of Steady Pressure Driven Flow Through Freeze Tape Cast Ceramic Pore Structures

Pulsed gradient spin echo NMR techniques were used to measure velocity weighted two dimensional images of pressure driven octane flowing through a freeze tape cast ceramic disk, see Figure 43. Flow direction is from the small to the large pore region by a pressure drop applied across the ceramic. The images of Figure 43 are weighted by the longitudinal component of the voxel average spin velocity vector in the *z*-axis flow direction through the disk thickness.

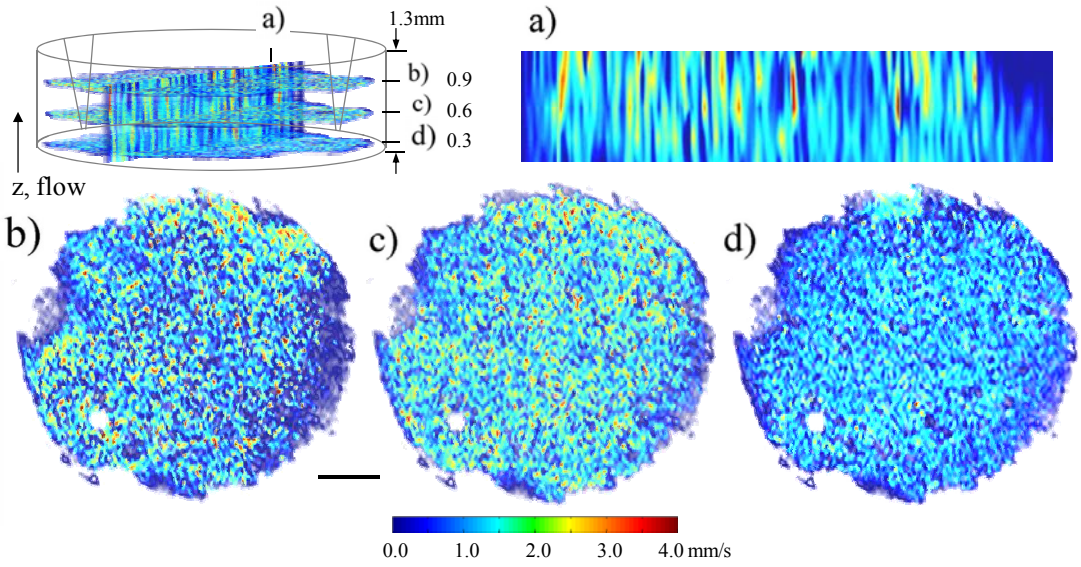

Figure 43: Depth resolved two dimensional longitudinal velocity images of steady pressure driven octane flowing though a YSZ freeze tape cast ceramic disk, bar = 1.00 mm, 40 x 80 µm/pixel, slice thickness = 300 µm, Δ = 5 ms, flow is parallel to direction of pore growth

Figure 43A is determined through interpolation of the transverse velocity planes. From a visual interpretation of Figure 43 the velocity distribution is narrower for the small pore region. This is a result of the transverse image resolution significantly exceeding the local pore dimensions, leading to a measurement of the regional average velocity as opposed to a velocity measurement near the pore scale as seen in Figure 43B. Due to the inclined nature of the pore structure, see Figure 39B, the local enhancement of the velocity present in Figure 43b) & c) could indicate transitions between individual pores as the streamlines must reorient themselves upward to transition between the individual pores.

A velocity probability distribution or histogram of velocities, calculated from the spatially resolved velocity images of Figure 43 represents the statistical distribution of coarse grained velocities averaged over the voxel dimensions of the image and the observation time Δ. A distribution of displacements over time Δ weighted by spin density, *i.e.* average propagator [6, 138], is measured using the one dimensional spatially resolved PGSE sequence. The longitudinal spin velocity probability distribution can then be calculated by dividing the longitudinal displacement $\mathbf{R}\cdot\hat{\mathbf{z}}$ by the observation time Δ. The velocity distribution of the one dimensional spatially resolved PGSE experiment thus reflects the dynamics of spins without the spatial coarse graining inherent in the two dimensional velocity image. Hence different spin density weighting is present in the velocity probability distribution calculated from the two dimensional velocity images. Differences between velocity probability distributions determined from the entire spin ensemble and the spatially coarse grained images reflect the nature of the variation between the distributions of non-spatially averaged and spatially averaged dynamics. Figure 44 shows the longitudinal velocity probability distribution from the PGSE sequence at

several longitudinal positions for the steady flow of octane through a freeze tape cast ceramic. Overlaid on the data is the velocity distribution resulting from the spatially resolved velocity imaging sequence. The flow direction is from the small to large pore region.

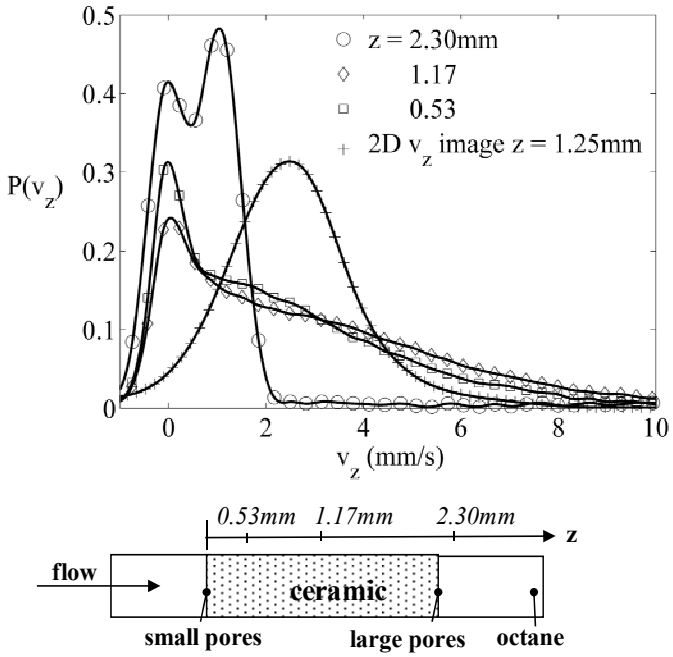

Figure 44: Velocity probability distributions of steady pressure driven octane from the PGSE propagator sequence for several z-axis locations in a YSZ freeze tape cast ceramic, Δ = 30 ms, flow is parallel to direction of pore growth

In a short porous media with evolving pore structure the concept of asymptotic dynamics is not relevant and pre-asymptotic dynamics or evolving dynamics must be considered. The measured velocity probabilities reflect the stationary dynamics at each depth z over a displacement observation time of Δ = 30 ms. At z = 0.53 mm there is clear evidence of a strong peak at zero velocity and a small peak near the average velocity of 2.0 mm/s with decreasing probability of higher velocity. This behavior indicates two populations of spin dynamics,

restricted and backbone, which undergo limited exchange in $\Delta = 30$ ms[118, 139]. As the pore size increases with increasing z, at $z = 1.17$ mm depth the propagator takes a form resembling data in model bead packs for which the displacement observation time Δ allows only a pore length displacement [140, 141]. Based on the structural images this seems to indicate spin motion within channels in which mixing is limited, *i.e.* dynamics are distributed continuously between spins in the low velocity pore wall regions to the fastest spins in the pore tube center, with no mechanical or diffusive Taylor dispersion mixing in time $\Delta = 30$ ms. It should be noted that entrance effects can impact the dynamics at the upper and lower ceramic boundaries. This is indicated by a dual population of octane present downstream of the ceramic boundaries. This behavior indicates the jetting of fluid from the porous ceramic with slow flow regions between pores and a discrete volume of stagnant fluid at the outer edge of the ceramic disk. The spatial depth variation of the average porosity (fluid volume fraction) can be estimated using the two dimensional velocity images and spatially resolved propagator data. Porosity estimations from the two dimensional velocity images rely upon overestimation of the volumetric flow rate due to image pixel dimensions exceeding the local pore dimensions. Porosity estimations from the PGSE propagator data utilize the planar average fluid velocity. The average spin velocity from the single pulse PGSE data can be calculated from the first moment of the displacement distribution

$$\langle v_z \rangle = \frac{1}{\Delta} \int_{-\infty}^{\infty} \mathbf{R} \bullet \hat{\mathbf{z}}\, P(z, \mathbf{R}, \Delta)\, d\mathbf{R} \qquad (1).$$

The longitudinal dependence of the transverse porosity is then

$$\varepsilon_{xy} = \frac{\dot{V}_{act}}{A_t \langle v_z \rangle} \qquad (2).$$

Where ε_{xy} is the transverse porosity, $\dot{V}_{act}$ is the known volumetric flow rate, A_t is the total (fluid and ceramic) transverse area. The transverse area, A_t, in Eqn. (2) can be found using either the imaging data from Figure 43 or Figure 40. Figure 45 shows the longitudinal distribution of the average transverse porosity estimated using the single pulse propagator data and spatially resolved velocity images. Also shown in Figure 45 is the bulk porosity for a similar freeze tape cast ceramic sample estimated from an Archimedes porosity experiment.

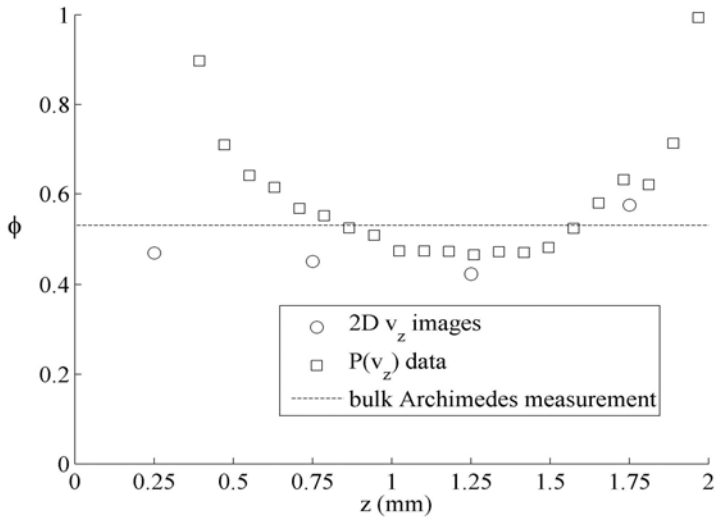

Figure 45: Transverse porosity of a YSZ freeze tape cast ceramic as a function of longitudinal position from the single pulse propagator data and spatially resolved velocity images

The calculated porosity from the NMR data exhibits a minimum in porosity at the ceramic depth of 1.25 mm. The porosity calculations from P(v_z) data are weighted by magnetic susceptibility effects very near the ceramic edges, i.e. ±0.5 mm, resulting in unrealistic values of the porosity.

Experiments were conducted on a freeze tape cast ceramic sample using the spatially resolved repeated and refocused experiments to determine the spatial dependence of the effective axial dispersion coefficient D^*_{zz}. Shown in Figure 46 are the spatially resolved effective axial dispersion coefficients from the velocity sensitive repeated PGSE and velocity compensated PGSE pulse sequences[142, 143].

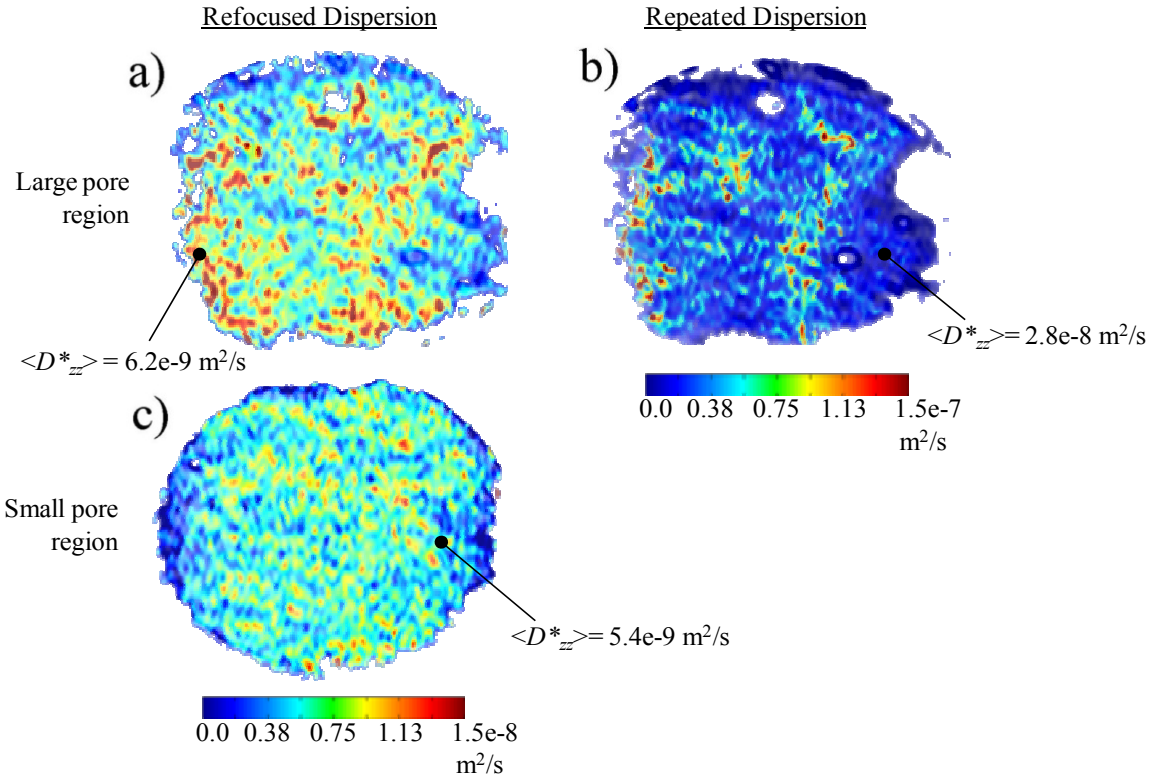

Figure 46: Spatially resolved effective axial dispersion coefficient of steady pressure driven octane flow in a YSZ freeze tape cast ceramic for the repeated and refocused echo sequences, 80 x 160 μm/pixel, slice thickness = 300 μm, 2Δ = 10 ms, τ = 5 ms

The refocused and repeated sequences vary in that the repeated sequence contains echo attenuation due to the distribution of coherent motion over the displacement time 2Δ as well as diffusive or random motion. In contrast, the refocused sequence refocuses magnetization

dephasing due to the spatial distribution of coherent motion and therefore echo attenuation is due to incoherent motion generated by free diffusion and mechanical dispersion only. This is achieved by reversing the effective polarity of the 2nd gradient pair in the refocused double PGSE experiment, see **Figure 10**. A comparison between Figure 46a) and Figure 46b) indicates that longitudinal motion of octane remains largely refocus-able for the time scale 2Δ = 10 ms probed. This is a consequence of the pore structure forcing the octane to maintain a relatively constant average velocity and limiting the amount of mechanical dispersion over the observation time 2Δ = 10ms. Figure 43A supports the limited role of mechanical dispersion by the backbone flow behavior appearing in the image.

Using the Stejskal -Tanner approximation the longitudinal dependence of the average axial effective dispersion coefficient was estimated from a one dimensional single pulse PGSE experiment, the results are shown in Figure 47. The choice of observation time Δ resulted in $\Delta << a^2/D_m$; so that molecular diffusion induced Taylor dispersion is small relative to mechanical and boundary layer dispersion mechanisms.

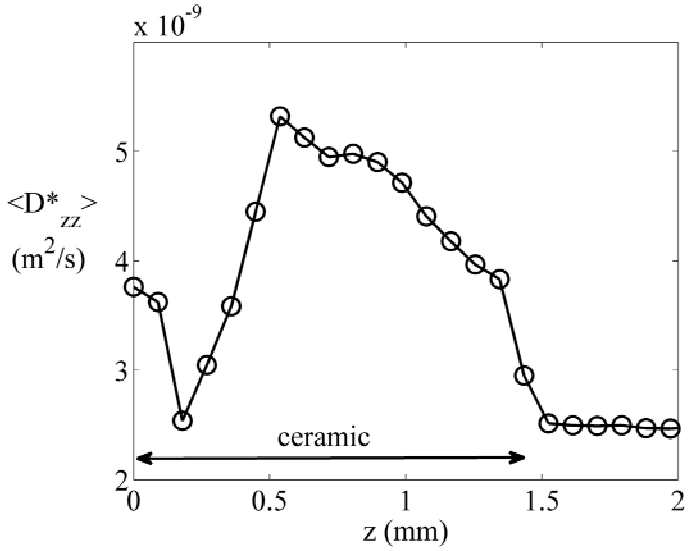

Figure 47: Average effective axial dispersion coefficient of steady octane flow within a YSZ freeze tape cast ceramic, $\Delta = 30$ ms

Outside of the ceramic a measurement near the room temperature self diffusion coefficient of octane was found. The distribution of the effective axial dispersion coefficient is a result of coupled variation in the pore dimensions and inter-pore connectivity. Figure 47 highlights the opportunity of these controllable pore structures to produce custom tailored transport dynamics.

Conclusion

A range of NMR techniques were used to characterize the pore structure of freeze tape cast ceramics and the pore structure impact on transport dynamics. Freeze tape cast ceramic pore structures prepared by a uni-directional solidification process are a complicated network of interconnected pores in which the average pore dimensions grow as a function of depth. Yttria stabilized zirconium oxide was found to agree well with the NMR experiment constraint that the sample material should induce only weak distortions in the applied magnetic fields. Spatially resolved NMR measurements were found to provide valuable, non-destructive, non-invasive,

information regarding the three dimensional variable freeze tape cast pore structure. The ability to resolve both the transport and pore structure information is a valuable asset to the study of these, and other, opaque structures. Further work is needed to probe the impact of variation in freeze tape casting manufacture parameters, *e.g.* casting bed temperature, on the ceramic pore structure and its effect on transport dynamics. However the data presented here outlines some of the opportunities of these structures to produce unique, custom tailored transport dynamics.

PORE SCALE HYDRODYNAMICS NEAR A ROUGH POROUS SURFACE OF MODEL SPHERE PACKS

Introduction

The hydrodynamic boundary layer near a porous surface is a phenomomenon of significant importance in many natural and industrial systems. In aquatic environments the water-porous hydrodynamic interface has important influence over the bio-geochemical cycle. In fuels cells the membrane-gas interface plays an important role in the chemical cycle and device operation. These and other examples have motivated extensive inquiry into the correct form of the hydrodynamic boundary conditions near a porous interface, see chapter 4. The most widely adopted condition is that proposed by Beavers and Joseph. Recent work has shown the assumption of Beavers and Joseph in which the boundary layer thickness is assumed to be on the order of $\sqrt{K}$, where K is the porous media permeability, underestimates actual boundary layer thicknesses by at least an order of magnitude [144, 145]. Furthermore it has been recognized that α, a property originally believed to be dependent on the interfacial structure, is dependent on the location of the macroscopic interface and hence not an intrinsic property of the interface [146]. The Beavers and Joseph and majority of other conditions are linear boundary conditions in which the gradient of velocity scales linearly with flow speed. It is unknown what if any role nonlinear inertial effects play in interfacial hydrodynamics. The purpose of this work is to explore the nature of interfacial hydrodynamics for a model porous media with the specific intent of addressing the question of inertia effects. Both NMR experiments and three dimensional LB simulations are used.

Materials and Methods

The model porous media used in the NMR experiments and LB simulations are monodisperse sphere packs. A square channel was partially filled with the packed array for the NMR experiments, see Figure 48.

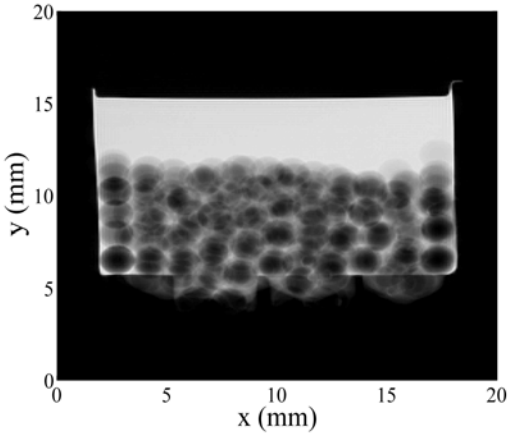

Figure 48: MRI cross section of the interfacial sample used in the NMR experiments

The packed bed shown in **Figure 48** is composed of monodisperse polymer spheres of diameter 1.5mm. The bed is treated with a chloroform solvent to lightly bond the polymer spheres together and thus forming a rigid bed. The bed has porosity of approximately 0.45. The open channel has a width of approximately 15mm and a height from the average upper layer sphere mid point of 4.75mm or 3.17 sphere diameters. The lower surface was drilled with randomly chosen hole sites to make the surface of the packed bed facing the channel appear "random". The resulting distribution of *y*-axis sphere locations is shown in Figure 49.

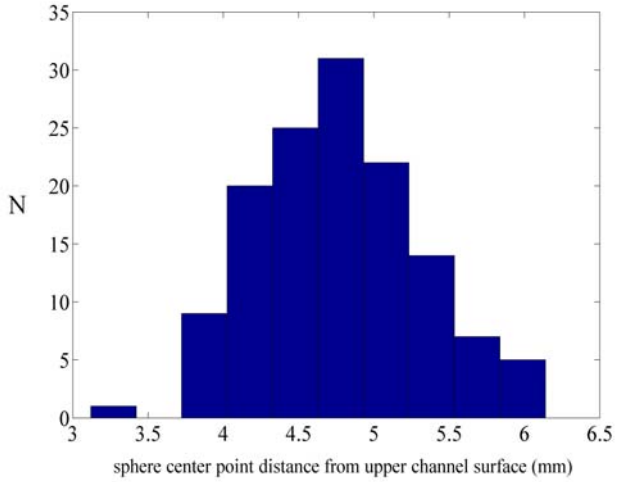

Figure 49: Distribution of sphere locations from the upper channel surface for the experimental sample

For the LB simulations three numerical samples of varying channel height were used, see Table 3.

Table 3: Parameters of the LB interfacial domain

Series	Channel height (*spheres*)	Bed porosity
I	5.0	0.44
II	7.5	0.44
III	10.0	0.44

The porous packed bed has a porosity of 0.44, the channel heights are H = 5, 7.5, and 10 sphere diameters. The channel height is defined from the upper surface to the mean center point of the upper sphere layer, see Figure 50.

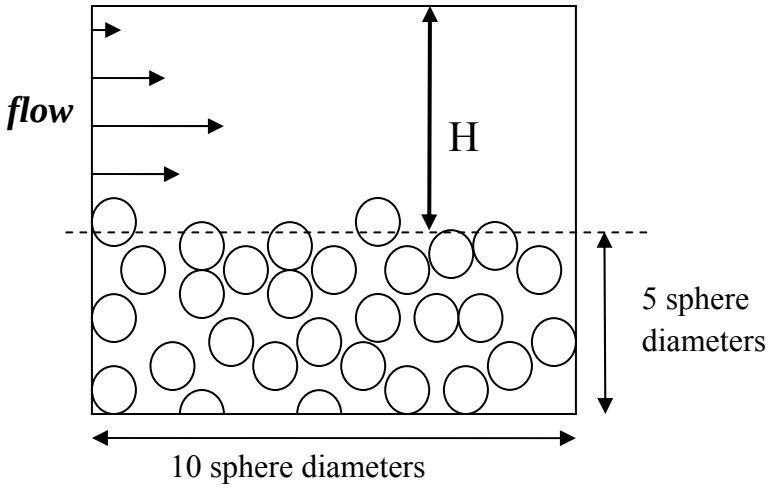

Figure 50: Schematic of the LB simulation interfacial domain

Identical sphere packing and hence interfacial surface are used in all three domains. The channel height is defined from the upper surface to the mean center point of the upper sphere layer. The square three dimensional domains of 10x10 sphere diameter cross section have periodic boundary conditions applied on the open faces and no flow conditions applied on the upper and lower walls. Numerical resolution is 51 grid points per sphere. The porosity profile through the numerical interface is shown in Figure 51.

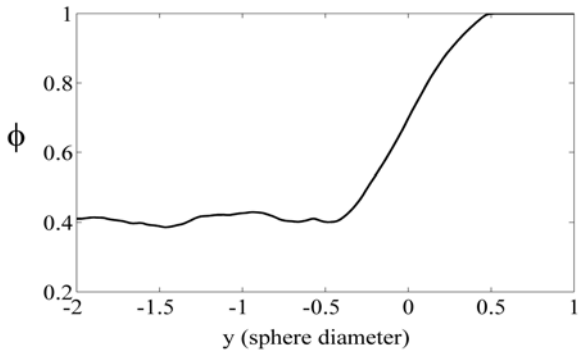

Figure 51: Porosity profile through the numerical interface

Results and Discussion

Lattice Boltzmann Simulations

The convective profile was solved for a range of pressure gradients and channel heights. The average planar velocity across the interface is plotted in **Figure 52** for the low Reynolds number limit and three channel heights.

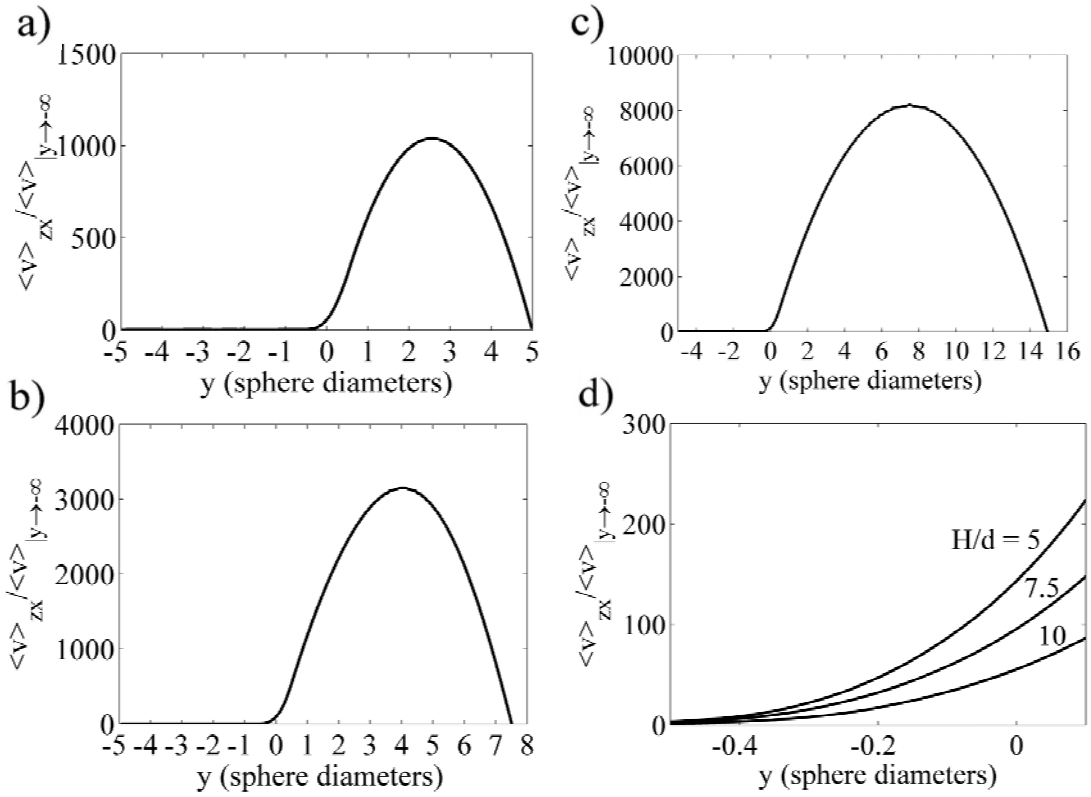

Figure 52: Low Reynolds number mean planar velocity profiles from LB simulation a) H/d=5 b) H/d=7.5 c) H/d=10 d) close up at the interface of the free fluid channel and porous media

The boundary layer in Figure 52 at the porous interface is apparent in the transition to the mean flow velocity in the porous media. It is not clear from the plots in **Figure 52** what defines the interface, however the boundary layer thickness is on the order of a sphere diameter and agrees

well with the observations of Goharzadeh *et al*. For a monodisperse packed bed of porosity 0.45 the Brinkmann screening length ($\sqrt{K}$) is on the order 0.04 sphere diameter; obviously an inaccurate estimation of the boundary layer thickness in Figure 52. The flow profile near the interface is complicated by the high rate of shear and relatively fast velocities. Images of the flow direction velocity are shown Figure 53 for the low Reynolds number limit.

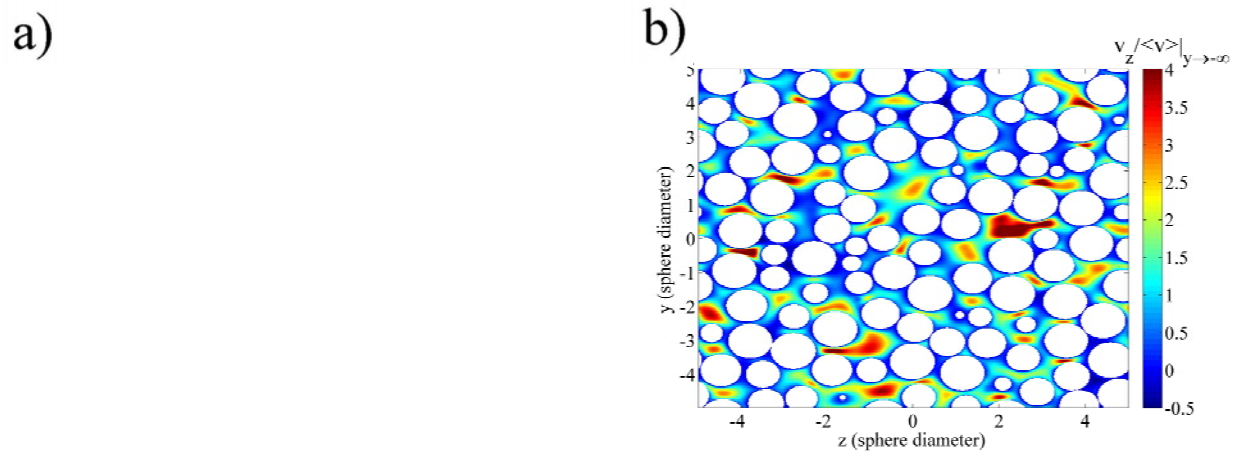

Figure 53: Examples of the flow direction velocity profile for the domain H/d=5 a) cross section at x = 0 b) interfacial cross section at y = -0.5d

A small amount of recirculation or negative flow is apparent in image a) of Figure 53, suggesting a complex interfacial flow profile. As the pressure gradient increases the convective profile near the interface changes from a Stokesian profile to one that includes inertial effects. This change is demonstrated in Figure 54 which shows the flow velocity PDF at the interface (±0.5d) for H/d=5.0 and several channel Reynolds numbers; defined as $Re_c = H\langle v_c \rangle/\eta$. As the channel Reynolds number increases the distribution becomes wider to include greater negative and positive velocities.

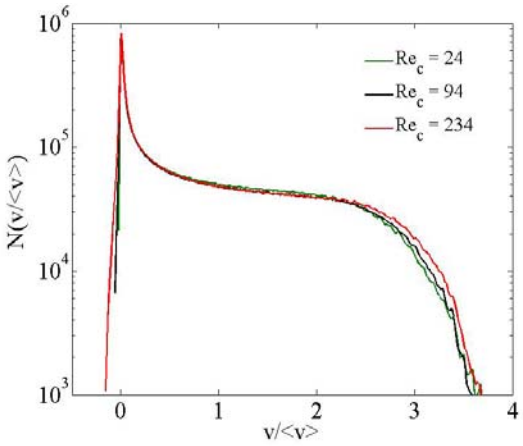

Figure 54: Flow direction velocity PDF at the interface for several channel Reynolds numbers and H/d = 5

The convective patterns near the model interface can be complex. Shown in Figure 55 are examples of the streamlines near the interface for H/d = 5.0 and channel Reynolds numbers of 230.

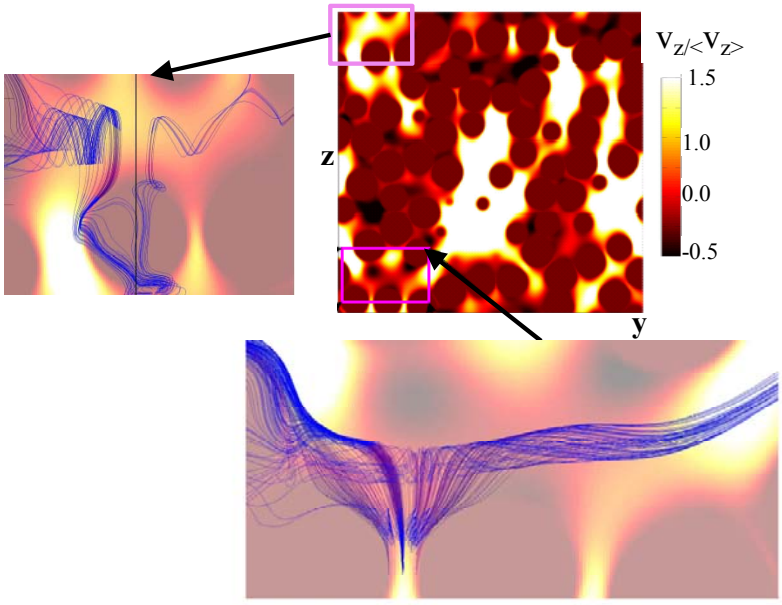

Figure 55: Examples of the flow streamlines at the interface (x = 0) and channel Reynolds number of Re_c = 230, field of view is the yz-plane

The streamline examples shown in Figure 55 are flow structures. The type of flow structures in Figure 55 occur throughout the interface and can thus be thought of as a general high Reynolds number feature of the hydrodynamic transition between the free fluid and porous media for a monodisperse packed bed. The open streamline flow structures in Figure 55 are visually similar to the horseshoe vortex [147]. The features suggest the importance of inertia at the interface at sufficiently high channel Reynolds number. The effect of inertia is demonstrated by plotting the interface Reynolds number as a function of the channel Reynolds number in Figure 56.

a) b)

Figure 56: Interface and channel Reynolds number as a function of porous media Reynolds number for various values of H/d a) interface b) channel

Over the entire range of Reynolds number in Figure 56b) the channel Reynolds number scales linearly with porous media Reynolds number. However the interfacial Reynolds number scales nonlinearly with the porous media Reynolds number at sufficiently high porous media Reynolds number. For H/d =5.0 this departure occurs at a channel Reynolds number of approximately 50 and with H/d=10 this departure occurs at a similar channel Reynolds number and interfacial Reynolds number. The interfacial Reynolds number scaling with porous media Reynolds number is sub-linear at sufficient porous media Reynolds number. This is expected because

inertial effects are an additional mechanism for pressure loss. Figure 56 demonstrates that inertial effects can be important in the interfacial hydrodynamics and hence boundary conditions. However the channel hydrodynamics remain linear over the range of porous media Reynolds number and hence the nonlinearity of the interfacial hydrodynamics would not be detected in a pressure drop measurements such as the *Beavers and Joseph* experiment. The velocity profile through the interface is plotted in Figure 57 for H/d = 5.0 and several channel Reynolds numbers.

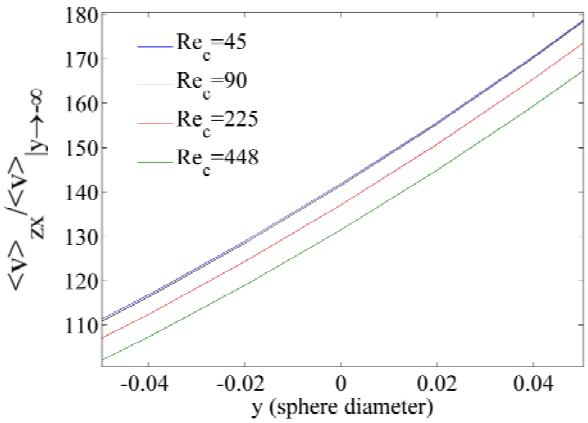

Figure 57: Velocity profile through the interface for H/d=10 and several channel Reynolds numbers

The mean velocity gradient profile is plotted in Figure 58 as a function of the channel Reynolds number and H/d=10.

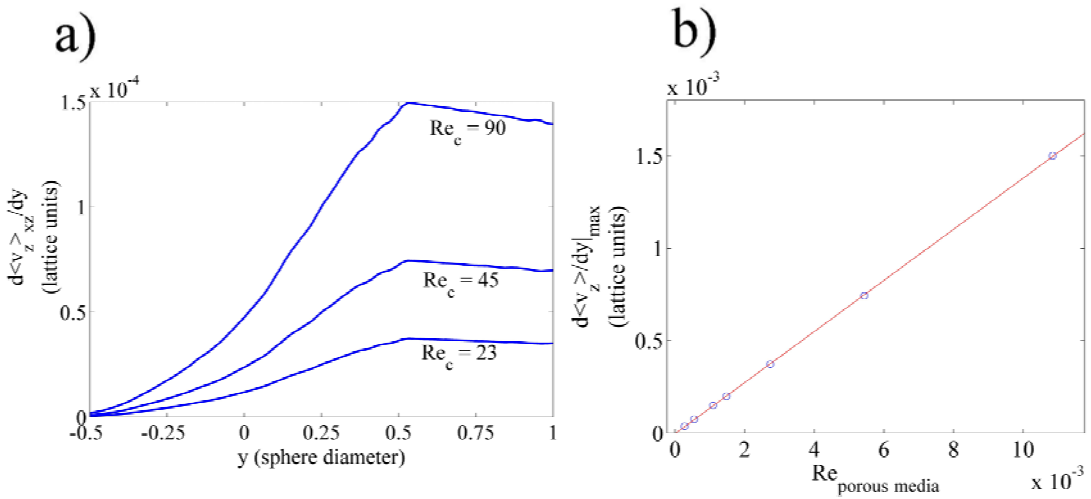

Figure 58: Interfacial mean planar velocity gradient as a function of Reynolds number with H/d=10 a) profile of velocity gradient as a function of Re_c b) maximum of velocity gradient as a function of porous media Reynolds number

In Figure 58 there is a discontinuity in the velocity gradient which occurs at a point in the domain where the porosity transitions from one to less than one. To the right of the discontinuity (in the free fluid domain) the planar velocity gradient scales linearly with direction while to the left of the discontinuity a nonlinear boundary layer is present in the transition to zero. Arguably, the interface can be defined at the *discontinuity point* or *point of porosity one* because it represents a point in which the functional form of the mean planar shear stress is discontinuous. To the author's knowledge this point has not yet been observed or mentioned explicitly in literature. The maximum velocity gradient in Figure 58 scales linearly with the porous media Reynolds number over the entire range even though the mean velocity at the interface scales nonlinearly with porous media Reynolds number at the higher Reynolds number values. That is to say that a boundary condition based upon the velocity gradient or shear at the interface will inaccurately capture inertial effects at the interface. This argues that the boundary

condition should be based upon the interfacial flow speed rather than the interfacial velocity gradient.

Lagrangian Particle Tracking: This section presents a brief survey of lagrangian particle tracking statistics near the interface. Shown in Figure 59 is the coordinate dispersion coefficient ($\mathbf{D}=\boldsymbol{\sigma}^2/\Delta$) as a function depth in the porous media and nondimensional time in the porous media ($t^*=\langle v\rangle|_{y\to\infty}\Delta/d$). The Reynolds number in the channel is sufficiently low so that the Stokes regime applies and the Peclet number in the porous media is 10. The initial thickness of the particle tracking volume was $\pm 0.1d$.

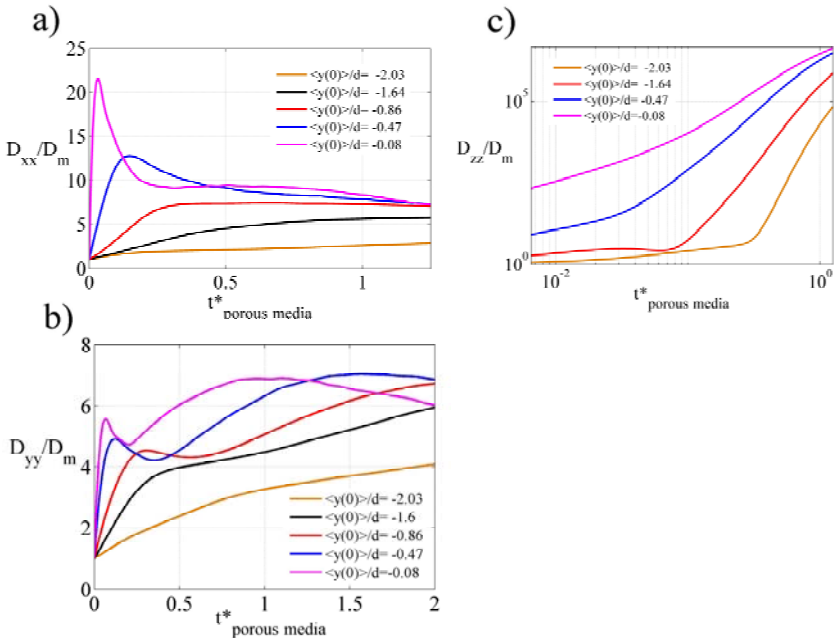

Figure 59: Effective dispersion coefficient as a function of particle tracking volume location and nondimensional porous media time

The curves shown in Figure 59 are complex. Starting with Figure 59b), the effective dispersion coefficient along the x-axis or perpendicular to the interface. Far into the porous media the

dynamics reflect well known low Peclet number dynamics with an asymptotically increasing effective dispersion coefficient. Near the interface however the mean flow velocity increases and the hydrodynamics begin to encounter complex vertical flow as seen in Figure 55. This has the effect of introducing a second time scale in the dynamics. The first high point of the effective dispersion coefficient is the result of pore scale vortices and the second much broader peak is the result of fluid motion around the structure. The first peak is much narrower then the second broad peak, reflecting the much shorter time scale of the vortices motion. Similar behavior is present in Figure 59a), the effective dispersion coefficient in the *y*-direction. However in this case the first peak has a significantly higher magnitude then the second peak. The first and second peaks occur on a similar time scale as those in Figure 59. In Figure 59c) the longitudinal effective dispersion coefficient is shown. Similar to the transverse curves in a) and b) the longitudinal curve contains an initial peak near the interface. The first peak only occurs in a limited area near the interface, unlike the transverse curves where the initial peaks occur over seemingly the entire interfacial zone. In the longitudinal curve there is only an initial curve and a continuously increasing effective dispersion coefficient. Indeed all three coordinates direction effective dispersion coefficients are anomalous (non-asymptotic) in the long time limit. This is to be expected considering the very different dispersion mechanisms and difference in flow velocities occurring in the two domains. Accurate modeling of transport near the interface must therefore use a nonlocal approach.

Magnetic Resonance Microscopy Data

Nuclear magnetic resonance was used to measure the flow direction velocity at the interface for water flow through the sample shown in Figure 48. The sample has a channel

height of 4.5 sphere diameters. Shown in Figure 60 is a flow direction velocity map at the sample interface for $Re_{interface} = 1.0$. Slice thickness is 1.5 sphere diameter and the center of the slice is located at the upper sphere layer midpoint. Flow direction is left to right across the page. The numerical and experimental sample differ in that the experimental sample is a channel, unlike the numerical sample which has periodic boundary conditions applied at all faces.

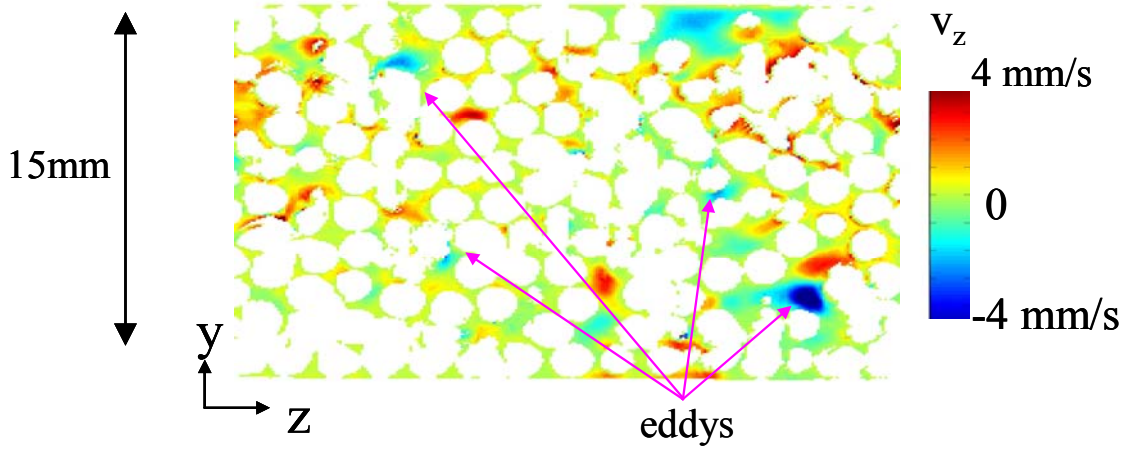

Figure 60: NMR measured flow direction velocity map at the interface, slice thickness is ½ sphere diameter

Significant regions of reverse flow can be seen in Figure 60. These flow domains are qualitatively similar to those seen in Figure 55. From this image is can be concluded that inertial hydrodynamic mechanisms are present at the hydrodynamic interface supporting the observations made in the numerical simulations above. An image of the flow direction velocity field is also shown in Figure 61.

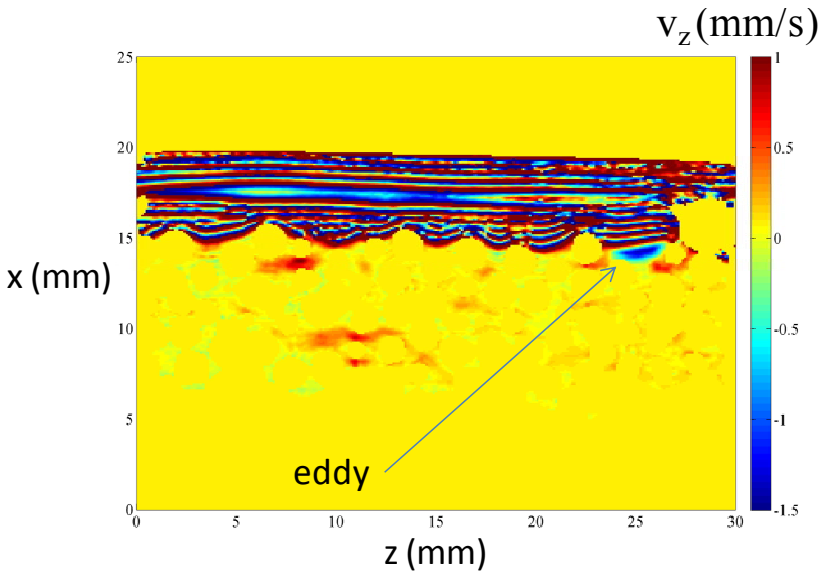

Figure 61: NMR measured flow direction velocity map through the interface, slice thickness is ½ sphere diameter

The velocity rainbow pattern in the channel of Figure 61 is the result of phase wrapping due to high velocities in the channel. Interfacial flow eddies are apparent in the image. A flow direction velocity map averaged in the flow direction was measured for the flow plane as shown in Figure 62, also shown in the average velocity profile through the interface of the inner one third of the channel.

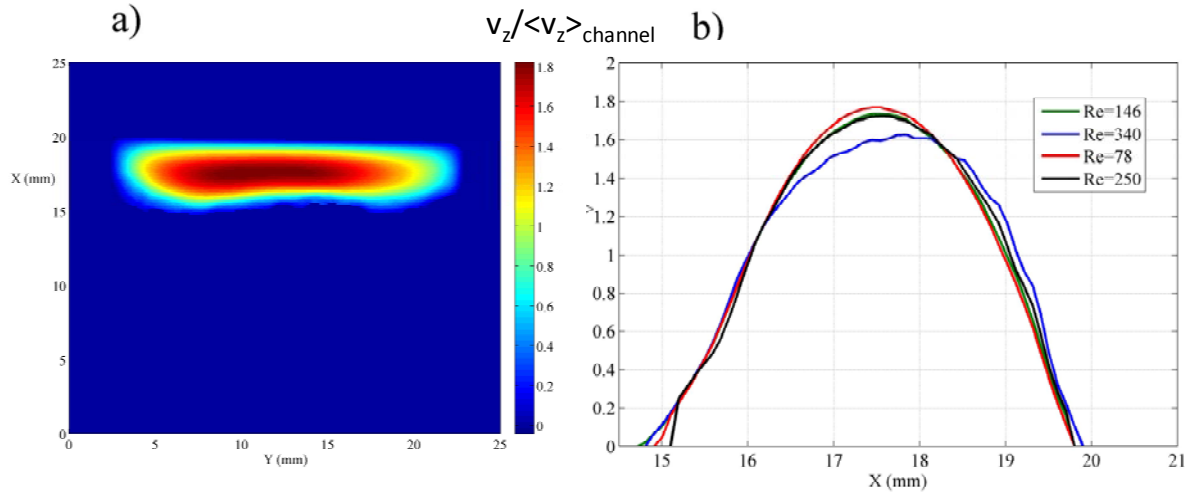

Figure 62: NMR measured flow direction velocity data a) average flow direction in plane low Reynolds number velocity map b) average velocity profile through the interface, at x=15mm, for several channel Reynolds numbers

The boundary layer through the interface is apparent in the curved velocity profile near the interface (*e.g.* x = 15mm) in image b). At high channel Reynolds (*e.g.* $Re_{channel}$>300) number the average velocity profile begins to blunt and the maximum of the profile approaches the upper (flat) boundary. This is suggestive of unsteady flow within the channel.

The complex velocity field in Figure 60 results in a relatively high rate of dispersion at the interface. Shown in Figure 63 is the NMR measured distribution of dispersion rates from a two dimensional image at the interface compared to the dispersion rates in the porous media.

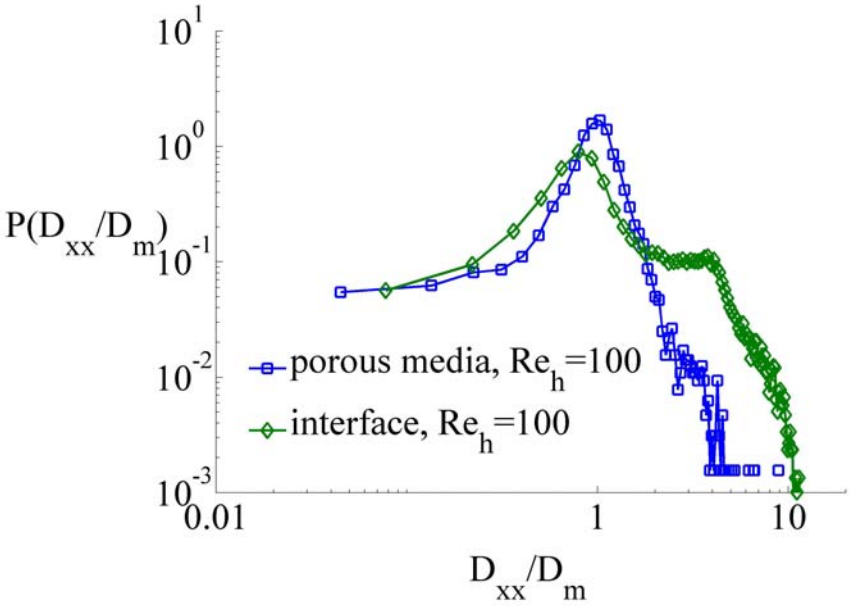

Figure 63: NMR measured dispersion coefficient distributions from two dimensional images at the interface and within the porous media, slice thickness is ½ sphere diameter and image resolution is 5 pixels per sphere, channel Reynolds number is 100, observation time is 10ms

The interfacial dispersion rates are significantly greater than the rates within the porous media, suggesting a wide range of velocities with the pixels at the interface. The dispersion rates within the porous media are similar to molecular diffusion because of the low Peclet number within the porous media. The interface contains a wide distribution of dispersion rates suggesting a wide range of velocities at the interface.

Conclusion

Hydrodynamics near the interface of a channel and porous media of monodisperse spheres were studied using three dimensional lattice Boltzmann simulations and nuclear magnetic resonance. Unique horseshoe like vortices were found at sufficiently high Reynolds

numbers. Inertial effects at the porous interface were found to become important at a channel Reynolds number of approximately 50. The eddies which occur at the porous interface were found to introduce a second mixing time scale at the interface. An important discontinuity in the mean planar velocity gradient was found to occur at the transition point to porosity one at the interface. At this point the functional form of the mean planar velocity gradient changes from linear to nonlinear in the porous media boundary layer. This point is the likely choice for the location of the interface because it is the point of obvious discontinuity. It was argued that the interfacial boundary condition should be based upon the interfacial velocity rather than the velocity gradient to capture interfacial inertial effects.

REFERENCES CITED

1. Abragam, A., *The principles of nuclear magnetism*. International series of monographs on physics. 1961, Oxford: Clarendon Press. xvi, 599 p.

2. Slichter, C.P., *Principles of magnetic resonance, with examples from solid state physics*. Harper's physics series. 1963, New York: Harper & Row. 246 p.

3. Ernst, R.R., G. Bodenhausen, and A. Wokaun, *Principles of nuclear magnetic resonance in one and two dimensions*. 1987, Oxford [Oxfordshire] New York: Clarendon Press ; Oxford University Press. xxiv, 610 p.

4. Mansfield, P. and P.G. Morris, *Nmr Imaging in Biomedicine.* Advances in Magnetic Resonance, 1982: p. 1-343.

5. Stejskal, E.O. and J.E. Tanner, *Spin Diffusion Measurements - Spin Echoes in Presence of a Time-Dependent Field Gradient.* Journal of Chemical Physics, 1965. **42**(1): p. 288-&.

6. Callaghan, P.T., *Principles of nuclear magnetic resonance microscopy*. 1991, Oxford [England] New York: Clarendon Press; Oxford University Press. xvii, 492 p.

7. Dirac, P.A.M., *The principles of quantum mechanics*. 4th ed. 1967, Oxford,: Clarendon Press. xii, 314 p.

8. Fukushima, E. and S.B.W. Roeder, *Experimental pulse NMR : a nuts and bolts approach*. 1981, Reading, Mass.: Addison-Wesley Pub. Co., Advanced Book Program. xiii, 539 p.

9. Bloch, F., W.W. Hansen, and M. Packard, *Nuclear Induction.* Physical Review, 1946. **69**(3-4): p. 127-127.

10. Torrey, H.C., *Bloch Equations with Diffusion Terms.* Physical Review, 1956. **104**(3): p. 563-565.

11. Lin, Y.Y., et al., *Resurrection of crushed magnetization and chaotic dynamics in solution NMR spectroscopy.* Science, 2000. **290**(5489): p. 118-121.

12. Mitra, P.P. and P.N. Sen, *Effects of Microgeometry and Surface Relaxation on Nmr Pulsed-Field-Gradient Experiments - Simple Pore Geometries.* Physical Review B, 1992. **45**(1): p. 143-156.

13. Kubo, R., *A Stochastic-Theory of Spin Relaxation.* Hyperfine Interactions, 1981. **8**(4-6): p. 731-738.

14. Bloembergen, N., E.M. Purcell, and R.V. Pound, *Relaxation Effects in Nuclear Magnetic Resonance Absorption.* Physical Review, 1948. **73**(7): p. 679-712.

15. Wolf, D., *Spin-temperature and nuclear-spin relaxation in matter : basic principles and applications*. 1979, Oxford New York: Clarendon Press; Oxford University Press. xviii, 462 p.

16. Hebel, L.C. and C.P. Slichter, *Nuclear Spin Relaxation in Normal and Superconducting Aluminum.* Physical Review, 1959. **113**(6): p. 1504-1519.

17. Hahn, E.L., *Spin Echoes.* Physical Review, 1950. **80**(4): p. 580-594.

18. Frahm, J., et al., *Stimulated Echo Imaging.* Journal of Magnetic Resonance, 1985. **64**(1): p. 81-93.

19. Mansfield, P., *Multi-Planar Image-Formation Using Nmr Spin Echoes.* Journal of Physics C-Solid State Physics, 1977. **10**(3): p. L55-L58.

20. Bailes, D.R. and D.J. Bryant, *Nmr Imaging.* Contemporary Physics, 1984. **25**(5): p. 441-475.

21. Hoult, D.I., *Solution of the Bloch Equations in the Presence of a Varying B1 Field - Approach to Selective Pulse Analysis.* Journal of Magnetic Resonance, 1979. **35**(1): p. 69-86.

22. Mansfiel.P and P.K. Grannell, *Nmr Diffraction in Solids.* Journal of Physics C-Solid State Physics, 1973. **6**(22): p. L422-L426.

23. Mansfield, P. and P.K. Grannell, *Diffraction and Microscopy in Solids and Liquids by Nmr.* Physical Review B, 1975. **12**(9): p. 3618-3634.

24. Edelstein, W.A., et al., *Spin Warp Nmr Imaging and Applications to Human Whole-Body Imaging.* Physics in Medicine and Biology, 1980. **25**(4): p. 751-756.

25. Doddrell, D.M., et al., *Water Signal Elimination Invivo, Using Suppression by Mistimed Echo and Repetitive Gradient Episodes.* Journal of Magnetic Resonance, 1986. **70**(1): p. 176-180.

26. Vold, R.L., et al., *Measurement of Spin Relaxation in Complex Systems.* Journal of Chemical Physics, 1968. **48**(8): p. 3831-&.

27. Carr, H.Y. and E.M. Purcell, *Effects of Diffusion on Free Precession in Nuclear Magnetic Resonance Experiments.* Physical Review, 1954. **94**(3): p. 630-638.

28. Callaghan, P.T., et al., *Recent Fourier and Laplace perspectives for multidimensional NMR in porous media.* Magnetic Resonance Imaging, 2007. **25**(4): p. 441-444.

29. Hunter, M.W. and P.T. Callaghan, *NMR measurement of nonlocal dispersion in complex flows.* Physical Review Letters, 2007. **99**(21): p. -.

30. Vanhove, L., *Correlations in Space and Time and Born Approximation Scattering in Systems of Interacting Particles.* Physical Review, 1954. **95**(1): p. 249-262.

31. Kampen, N.G.v., *Stochastic processes in physics and chemistry*. 1981, Amsterdam ; New York New York: North-Holland; sole distributors for the USA and Canada, Elsevier North-Holland. xiv, 419 p.

32. Scheven, U.M. and P.N. Sen, *Spatial and temporal coarse graining for dispersion in randomly packed spheres.* Physical Review Letters, 2002. **89**(25): p. -.

33. Scheven, U.M., et al., *Quantitative nuclear magnetic resonance measurements of preasymptotic dispersion in flow through porous media.* Physics of Fluids, 2005. **17**(11): p. -.

34. Stilbs, P., *Fourier transform pulsed-gradient spin-echo studies of molecular diffusion.* Progress in Nuclear Magnetic Resonance Spectroscopy, 1987. **19**: p. 1-45.

35. Callaghan, P.T., S.L. Codd, and J.D. Seymour, *Spatial coherence phenomena arising from translational spin motion in gradient spin echo experiments.* Concepts in Magnetic Resonance, 1999. **11**(4): p. 181-202.

36. Khrapitchev, A.A. and P.T. Callaghan, *Spatial dependence of dispersion.* Magnetic Resonance Imaging, 2003. **21**(3-4): p. 373-375.

37. Black, H.S., *Modulation theory*. Bell Telephone Laboratories series. 1953, New York,: Van Nostrand. xi, 363 p.

38. Cooley, J.W. and J.W. Tukey, *An Algorithm for Machine Calculation of Complex Fourier Series.* Mathematics of Computation, 1965. **19**(90): p. 297-&.

39. Chen, S. and G.D. Doolen, *Lattice Boltzmann method for fluid flows.* Annual Review of Fluid Mechanics, 1998. **30**: p. 329-364.

40. Qian, Y.H., D. Dhumieres, and P. Lallemand, *Lattice Bgk Models for Navier-Stokes Equation.* Europhysics Letters, 1992. **17**(6bis): p. 479-484.

41. Maier, R.S., R.S. Bernard, and D.W. Grunau, *Boundary conditions for the lattice Boltzmann method.* Physics of Fluids, 1996. **8**(7): p. 1788-1801.

42. Panton, R.L., *Incompressible flow*. 2nd ed. 1996, New York: Wiley. xvii, 837 p.

43. Whitaker, S., *Flow in Porous-Media .1. A Theoretical Derivation of Darcys-Law.* Transport in Porous Media, 1986. **1**(1): p. 3-25.

44. Bear, J., *Dynamics of fluids in porous media*. Dover books on physics and chemistry. 1988, New York: Dover. xvii, 764 p.

45. Whitaker, S., *The Forchheimer equation: A theoretical development.* Transport in Porous Media, 1996. **25**(1): p. 27-61.

46. Whitaker, S., *Flow in Porous-Media .2. The Governing Equations for Immiscible, 2-Phase Flow.* Transport in Porous Media, 1986. **1**(2): p. 105-125.

47. Vafai, K. and S.J. Kim, *On the Limitations of the Brinkman-Forchheimer Extended Darcy Equation.* International Journal of Heat and Fluid Flow, 1995. **16**(1): p. 11-15.

48. Nield, D.A., *The Limitations of the Brinkman-Forchheimer Equation in Modeling Flow in a Saturated Porous-Medium and at an Interface.* International Journal of Heat and Fluid Flow, 1991. **12**(3): p. 269-272.

49. Sahraoui, M. and M. Kaviany, *Slip and No-Slip Velocity Boundary-Conditions at Interface of Porous, Plain Media.* International Journal of Heat and Mass Transfer, 1992. **35**(4): p. 927-943.

50. Beavers, G.S. and D.D. Joseph, *Boundary Conditions at a Naturally Permeable Wall.* Journal of Fluid Mechanics, 1967. **30**: p. 197-&.

51. Alazmi, B. and K. Vafai, *Analysis of fluid flow and heat transfer interfacial conditions between a porous medium and a fluid layer.* International Journal of Heat and Mass Transfer, 2001. **44**(9): p. 1735-1749.

52. Ochoatapia, J.A. and S. Whitaker, *Momentum-Transfer at the Boundary between a Porous-Medium and a Homogeneous Fluid .1. Theoretical Development.* International Journal of Heat and Mass Transfer, 1995. **38**(14): p. 2635-2646.

53. Ochoatapia, J.A. and S. Whitaker, *Momentum-Transfer at the Boundary between a Porous-Medium and a Homogeneous Fluid .2. Comparison with Experiment.* International Journal of Heat and Mass Transfer, 1995. **38**(14): p. 2647-2655.

54. Ochoa-Tapia, J.A. and S. Whitaker, *Momentum jump condition at the boundary between a porous medium and a homogeneous fluid: Inertial effects.* Journal of Porous Media, 1998. **1**(3): p. 201-217.

55. Whitaker, S., *Diffusion and Dispersion in Porous Media.* Aiche Journal, 1967. **13**(3): p. 420-&.

56. Whitaker, S., *The method of volume averaging*. 1999, Dordrecht ; Boston: Kluwer Academic. xvi, 219.

57. Koch, D.L. and J.F. Brady, *A Nonlocal Description of Advection Diffusion with Application to Dispersion in Porous-Media.* Journal of Fluid Mechanics, 1987. **180**: p. 387-403.

58. Sahimi, M., *Flow and transport in porous media and fractured rock : from classical methods to modern approaches*. 1995, Weinheim ; New York: VCH. xiv, 482 p.

59. Zwanzig, R., *Nonequilibrium statistical mechanics*. 2001, Oxford ; New York: Oxford University Press. ix, 222 p.

60. Mori, H., *A Continued-Fraction Representation of Time-Correlation Functions.* Progress of Theoretical Physics, 1965. **34**(3): p. 399-&.

61. Boon, J.-P. and S. Yip, *Molecular hydrodynamics*. 1980, New York: McGraw-Hill. xvii, 417 p.

62. Pelley, A.J. and N. Tufenkji, *Effect of particle size and natural organic matter on the migration of nano- and microscale latex particles in saturated porous media.* Journal of Colloid and Interface Science, 2008. **321**(1): p. 74-83.

63. Elimelech, M. and C.R. Omelia, *Kinetics of Deposition of Colloidal Particles in Porous-Media.* Environmental Science & Technology, 1990. **24**(10): p. 1528-1536.

64. Ko, C.H., S. Bhattacharjee, and M. Elimelech, *Coupled influence of colloidal and hydrodynamic interactions on the RSA dynamic blocking function for particle deposition onto packed spherical collectors.* Journal of Colloid and Interface Science, 2000. **229**(2): p. 554-567.

65. Scheibe, T.D. and B.D. Wood, *A particle-based model of size or anion exclusion with application to microbial transport in porous media.* Water Resources Research, 2003. **39**(4): p. -.

66. Brown, J.R., et al., *Nuclear magnetic resonance measurement of shear-induced particle migration in Brownian suspensions.* Physics of Fluids, 2009. **21**(9): p. -.

67. Gibson, L.J. and M.F. Ashby, *Cellular solids : structure and properties*. 2nd ed. Cambridge solid state science series. 1997, Cambridge ; New York: Cambridge University Press. xviii, 510 p.

68. Vogel, S., *Life in moving fluids : the physical biology of flow*. 2nd ed. 1994, Princeton, N.J.: Princeton University Press. xiii, 467 p.

69. Twigg, M.V. and J.T. Richardson, *Fundamentals and applications of structured ceramic foam catalysts.* Industrial & Engineering Chemistry Research, 2007. **46**(12): p. 4166-4177.

70. Banhart, J., *Manufacture, characterisation and application of cellular metals and metal foams.* Progress in Materials Science, 2001. **46**(6): p. 559-U3.

71. Richardson, J.T., D. Remue, and J.K. Hung, *Properties of ceramic foam catalyst supports: mass and heat transfer.* Applied Catalysis a-General, 2003. **250**(2): p. 319-329.

72. Montminy, M.D., A.R. Tannenbaum, and C.W. Macosko, *The 3D structure of real polymer foams.* Journal of Colloid and Interface Science, 2004. **280**(1): p. 202-211.

73. Sahimi, M., *Heterogeneous Materials I: Linear Transport and Optical Properties*. Interdisciplinary Applied Mathematics, ed. L. Sirovich. Vol. 22. 2003, New York: Springer-Verlag. 691.

74. Johnson, D.L., J. Koplik, and L.M. Schwartz, *New pore size parameter characterizing transport in porous media.* Physical Review Letters, 1986. **57**(20): p. 2564-2567.

75. Roberts, A.P. and M.A. Knackstedt, *Structure-property correlations in model composite materials.* Physical Review E, 1996. **54**(3): p. 2313-2328.

76. Callaghan, P.T., et al., *Diffraction-like effects in NMR diffusion studies of fluids in porous solids.* Nature, 1991. **351**: p. 467-469.

77. Mitra, P.P., P.N. Sen, and L.M. Schwartz, *Short time behavior of the diffusion coefficient as a geometrical probe of porous media.* Physical Review B: Condensed Matter, 1993. **47**(14): p. 8565-8574.

78. Seymour, J.D. and P.T. Callaghan, *"Flow-Diffraction" structural characterization and measurement of hydrodynamic dispersion in porous media by PGSE NMR.* Journal of Magnetic Resonance. Series A, 1996. **122**: p. 90-93.

79. Seymour, J.D. and P.T. Callaghan, *Generalized approach to NMR analysis of flow and dispersion in porous medium.* AIChE Journal, 1997. **43**: p. 2096-2111.

80. Kandhai, D., et al., *Influence of stagnant zones on transient and asymptotic dispersion in macroscopically homogeneous porous media.* Physical Review Letters, 2002. **88**(23).

81. Scheven, U.M. and P.N. Sen, *Spatial and temporal coarse graining for dispersion in randomly packed spheres.* Physical Review Letters, 2002. **89**(25): p. 254501.

82. Scheven, U.M., R. Harris, and M.L. Johns, *Intrinsic dispersivity of randomly packed monodisperse spheres.* Physical Review Letters, 2007. **99**: p. 054502.

83. Callaghan, P.T. and S.L. Codd, *Flow coherence in a bead pack observed using Frequency Domain Modulated Gradient NMR.* Physics of Fluids, 2001. **13**: p. 412-427.

84. Seymour, J.D., et al., *Anomalous fluid transport in porous media induced by biofilm growth.* Physical Review Letters, 2004. **93**(19): p. 198103.

85. Khrapitchev, A.A. and P.T. Callaghan, *Reversible and irreversible dispersion in a porous medium* Physics of Fluids, 2003. **15**(9): p. 2649-2660.

86. Maier, R.S., et al., *Pore-scale simulation of dispersion.* Physics of Fluids, 2000. **12**: p. 2065-2079.

87. Berne, B.J., J.P. Boon, and S.A. Rice, *On the calculation of autocorrelation functions of dynamical variables.* Journal of Chemical Physics, 1966. **45**(4): p. 1086-1096.

88. Boon, J.P. and S. Yip, *Molecular Hydrodynamics*. 1991, New York: Dover Publications.

89. Cushman, J.H., B.X. Hu, and T.R. Ginn, *Nonequilibrium statistical mechanics of preasymptotic dispersion.* Journal of Statistical Physics, 1994. **75**: p. 859-878.

90. von der Schulenburg, D.A.G., et al., *Flow through an evolving porous media-compressed foam.* Journal of Materials Science, 2007. **42**(16): p. 6541-6548.

91. Perrot, C., R. Panneton, and X. Olny, *Periodic unit cell reconstruction of porous media: Application to open-cell aluminum foams.* Journal of Applied Physics, 2007. **101**(11): p. -

92. Kwon, Y.W., R.E. Cooke, and C. Park, *Representative unit-cell models for open-cell metal foams with or without elastic filler.* Materials Science and Engineering a-Structural Materials Properties Microstructure and Processing, 2003. **343**(1-2): p. 63-70.

93. Olurin, O.B., et al., *The investigation of morphometric parameters of aluminium foams using micro-computed tomography.* Materials Science and Engineering a-Structural Materials Properties Microstructure and Processing, 2002. **328**(1-2): p. 334-343.

94. Bhattacharya, A., V.V. Calmidi, and R.L. Mahajan, *Thermophysical properties of high porosity metal foams.* International Journal of Heat and Mass Transfer, 2002. **45**(5): p. 1017-1031.

95. Fourie, J.G. and J.P. Du Plessis, *Pressure drop modelling in cellular metallic foams.* Chemical Engineering Science, 2002. **57**(14): p. 2781-2789.

96. Giani, L., G. Groppi, and E. Tronconi, *Mass-transfer characterization of metallic foams as supports for structured catalysts.* Industrial & Engineering Chemistry Research, 2005. **44**(14): p. 4993-5002.

97. Richardson, J.T., Y. Peng, and D. Remue, *Properties of ceramic foam catalyst supports: pressure drop.* Applied Catalysis a-General, 2000. **204**(1): p. 19-32.

98. Maier, R.S., et al., *Pore-scale simulation of dispersion.* Physics of Fluids, 2000. **12**(8): p. 2065-2079.

99. Quintard, M. and S. Whitaker, *Transport in Ordered and Disordered Porous-Media - Volume-Averaged Equations, Closure Problems, and Comparison with Experiment.* Chemical Engineering Science, 1993. **48**(14): p. 2537-2564.

100. Berne, B.J. and R. Pecora, *Dynamic light scattering : with applications to chemistry, biology, and physics*. 1976, New York: Wiley. vii, 376 p.

101. Koch, D.L. and J.F. Brady, *Dispersion in Fixed-Beds.* Journal of Fluid Mechanics, 1985. **154**(May): p. 399-427.

102. Stapf, S., et al., *Spatial correlations and dispersion for fluid transport through packed glass beads studied by pulsed field-gradient NMR.* Physical Review E, 1998. **58**(5): p. 6206-6221.

103. Callaghan, P.T. and S.L. Codd, *Flow coherence in a bead pack observed using frequency domain modulated gradient nuclear magnetic resonance.* Physics of Fluids, 2001. **13**(2): p. 421-427.

104. Callaghan, P.T. and J. Stepisnik, *Frequency-Domain Analysis of Spin Motion Using Modulated-Gradient Nmr.* Journal of Magnetic Resonance Series A, 1995. **117**(1): p. 118-122.

105. Ginn, T.R., et al., *Processes in microbial transport in the natural subsurface.* Advances in Water Resources, 2002. **25**(8-12): p. 1017-1042.

106. Ryan, J.N. and M. Elimelech, *Colloid mobilization and transport in groundwater.* Colloids and Surfaces a-Physicochemical and Engineering Aspects, 1996. **107**: p. 1-56.

107. Kersting, A.B., et al., *Migration of plutonium in ground water at the Nevada Test Site.* Nature, 1999. **397**(6714): p. 56-59.

108. Li, X.Q., T.D. Scheibe, and W.P. Johnson, *Apparent decreases in colloid deposition rate coefficients with distance of transport under unfavorable deposition conditions: A general phenomenon.* Environmental Science & Technology, 2004. **38**(21): p. 5616-5625.

109. Brown, J.R., et al., *Dynamics of the solid and liquid phases in dilute sheared Brownian suspensions: Irreversibility and particle migration.* Physical Review Letters, 2007. **99**(24): p. -.

110. Seymour, J.D. and P.T. Callaghan, *Generalized approach to NMR analysis of flow and dispersion in porous media.* Aiche Journal, 1997. **43**(8): p. 2096-2111.

111. Loxley, A. and B. Vincent, *Preparation of poly(methylmethacrylate) microcapsules with liquid cores.* Journal of Colloid and Interface Science, 1998. **208**(1): p. 49-62.

112. Wassenius, H., M. Nyden, and B. Vincent, *NMR diffusion studies of translational properties of oil inside core-shell latex particles.* Journal of Colloid and Interface Science, 2003. **264**(2): p. 538-547.

113. Elimelech, M. and Knovel (Firm). *Particle deposition and aggregationmeasurement, modelling, and simulation*. [Online book] 1998 [cited; Pbk.:[xv, 441 p.]. Available from: http://www.knovel.com/knovel2/Toc.jsp?BookID=437

114. Hiemenz, P.C. and R. Rajagopalan, *Principles of colloid and surface chemistry*. 3rd ed. 1997, New York: Marcel Dekker. xix, 650 p.

115. Frank, M., et al., *Particle migration in pressure-driven flow of a Brownian suspension.* Journal of Fluid Mechanics, 2003. **493**: p. 363-378.

116. Pine, D.J., et al., *Chaos and threshold for irreversibility in sheared suspensions.* Nature, 2005. **438**(7070): p. 997-1000.

117. Wassenius, H., M. Nyden, and B. Vincent, *NMR diffusion studies of translational properties of oil inside core-shell latex particles.* Journal of Colloid and Interface Science, 2003. **264**: p. 538-547.

118. Kandhai, D., et al., *Influence of stagnant zones on transient and asymptotic dispersion in macroscopically homogeneous porous media.* Physical Review Letters, 2002. **88**(23): p. -.

119. T.R., B., et al., *Dynamic Length Scale Characterization and Nonequilibrium Statistical Mechanics of Transport in Open Cell Foams.* physical Review Letters, 2009(in press).

120. Salles, J., et al., *Taylor Dispersion in Porous-Media - Determination of the Dispersion Tensor.* Physics of Fluids a-Fluid Dynamics, 1993. **5**(10): p. 2348-2376.

121. Scheven, U.M., R. Harris, and M.L. Johns, *Intrinsic dispersivity of randomly packed monodisperse spheres.* Physical Review Letters, 2007. **99**(5): p. -.

122. Sofie, S.W., *Fabrication of functionally graded and aligned porosity in thin ceramic substrates with the novel freeze-tape-casting process.* Journal of the American Ceramic Society, 2007. **90**(7): p. 2024-2031.

123. Callaghan, P.T., et al., *Diffraction-Like Effects in Nmr Diffusion Studies of Fluids in Porous Solids.* Nature, 1991. **351**(6326): p. 467-469.

124. Mitra, P.P., P.N. Sen, and L.M. Schwartz, *Short-Time Behavior of the Diffusion-Coefficient as a Geometrical Probe of Porous-Media.* Physical Review B, 1993. **47**(14): p. 8565-8574.

125. Hatfield, G.R. and K.R. Carduner, *Solid-State Nmr - Applications in High-Performance Ceramics.* Journal of Materials Science, 1989. **24**(12): p. 4209-4219.

126. Beyea, S.D., et al., *Spatially resolved adsorption isotherms of thermally polarized perfluorinated gases in yttria-stabilized tetragonal-zirconia polycrystal ceramic materials with NMR imaging.* Applied Magnetic Resonance, 2002. **22**(2): p. 175-186.

127. Beyea, S.D., et al., *Nondestructive characterization of nanopore microstructure: Spatially resolved Brunauer-Emmett-Teller isotherms using nuclear magnetic resonance imaging.* Journal of Applied Physics, 2003. **94**(2): p. 935-941.

128. Hayashi, K., et al., *Nmr Imaging of Advanced Ceramics during the Slip Casting Process.* Journal of Physics D-Applied Physics, 1988. **21**(6): p. 1037-1039.

129. Lizak, M.J., M.S. Conradi, and C.G. Fry, *Nmr Imaging of Gas Imbibed into Porous Ceramic.* Journal of Magnetic Resonance, 1991. **95**(3): p. 548-557.

130. Mair, R.W., et al., *Probing porous media with gas diffusion NMR.* Physical Review Letters, 1999. **83**(16): p. 3324-3327.

131. Codd, S.L. and S.A. Altobelli, *A PGSE study of propane gas flow through model porous bead packs.* Journal of Magnetic Resonance, 2003. **163**(1): p. 16-22.

132. Manz, B., P. Alexander, and L.F. Gladden, *Correlations between dispersion and structure in porous media probed by nuclear magnetic resonance.* Physics of Fluids, 1999. **11**(2): p. 259-267.

133. Khrapitchev, A.A. and P.T. Callaghan, *Reversible and irreversible dispersion in a porous medium.* Physics of Fluids, 2003. **15**(9): p. 2649-2660.

134. Boaro, M., J.M. Vohs, and R.J. Gorte, *Synthesis of highly porous yttria-stabilized zirconia by tape-casting methods.* Journal of the American Ceramic Society, 2003. **86**(3): p. 395-400.

135. Koch, D., et al., *Evolution of porosity by freeze casting and sintering of sol-gel derived ceramics.* Journal of Sol-Gel Science and Technology, 2003. **26**(1-3): p. 149-152.

136. Moon, J.W., et al., *Preparation of dense thin-flm solid electrolyte on novel porous structure with parallel pore channel.* Journal of the Ceramic Society of Japan, 2002. **110**(5): p. 479-484.

137. Fukasawa, T., et al., *Pore structure of porous ceramics synthesized from water-based slurry by freeze-dry process.* Journal of Materials Science, 2001. **36**(10): p. 2523-2527.

138. Stejskal, E.O., *Use of Spin Echoes in a Pulsed Magnetic-Field Gradient to Study Anisotropic Restricted Diffusion and Flow.* Journal of Chemical Physics, 1965. **43**(10P1): p. 3597-&.

139. Tallarek, U., et al., *Study of transport phenomena in chromatographic columns by pulsed field gradient NMR.* Journal of Physical Chemistry B, 1998. **102**(18): p. 3486-3497.

140. Lebon, L., et al., *Pulsed field gradient NMR measurements of probability distribution of displacement under flow in sphere packings.* Magnetic Resonance Imaging, 1996. **14**(7-8): p. 989-991.

141. Maier, R.S., et al., *Simulation of flow through bead packs using the lattice Boltzmann method.* Physics of Fluids, 1998. **10**(1): p. 60-74.

142. Caprihan, A. and J.D. Seymour, *Correlation time and diffusion coefficient imaging: Application to a granular flow system.* Journal of Magnetic Resonance, 2000. **144**(1): p. 96-107.

143. Seymour, J.D., et al., *Pulsed gradient spin echo nuclear magnetic resonance imaging of diffusion in granular flow.* Physical Review Letters, 2000. **84**(2): p. 266-269.

144. Goharzadeh, A., A. Khalili, and B.B. Jorgensen, *Transition layer thickness at a fluid-porous interface.* Physics of Fluids, 2005. **17**(5): p. -.

145. Gupte, S.K. and S.G. Advani, *Flow near the permeable boundary of a porous medium: An experimental investigation using LDA.* Experiments in Fluids, 1997. **22**(5): p. 408-422.

146. Jamet, D. and M. Chandesris, *On the intrinsic nature of jump coefficients at the interface between a porous medium and a free fluid region.* International Journal of Heat and Mass Transfer, 2009. **52**(1-2): p. 289-300.

147. Baker, C.J., *Laminar Horseshoe Vortex.* Journal of Fluid Mechanics, 1979. **95**(Nov): p. 347-&.

APPENDIX A

MEASURING THE MEAN STRUT LENGTH OF RANDOMLY ORIENTATED FOAMS USING TWO DIMENSIONAL IMAGES

The following discussion summarizes a technique which can be applied to two dimensional images of a randomly oriented strut population to determine the mean length of the population. The mean length of large population of struts can be written as the first moment of the probability distribution of strut lengths:

$$\langle l \rangle = \int_0^\infty l\, P(l)\, dl \qquad \text{(A1)}$$

Where $\langle l \rangle$ is the mean strut length and $P(l)$ is the probability distribution of strut lengths l. For a large population of randomly oriented struts in three dimensional space the distribution $P(l)$ is invariant to angular orientation. In other words the functional form of the strut length probability distribution oriented parallel with a unit vector, $\hat{\mathbf{r}}$, is invariant to the orientation of $\hat{\mathbf{r}}$. With this assumption the mean length of the strut population in any Cartesian direction, $\langle l_i \rangle$, can be written as the average of strut lengths in phase space:

$$\langle l_i \rangle = \frac{\int_0^{\pi/2}\int_0^{\pi/2} \langle l \rangle \sin\theta \cos\phi \; d\theta d\phi}{\int_0^{\pi/2}\int_0^{\pi/2} d\theta d\phi} \qquad \text{(A2)}$$

Integrating yields:

$$\langle l \rangle = \frac{\pi^2}{4} \langle l_i \rangle \qquad \text{(A3)}$$

Equation A3 expresses the mean strut length of a randomly oriented strut population in terms of the mean length of the population along a Cartesian direction. The mean Cartesian length, $\langle l_i \rangle$, can be determined from two dimensional images of the structure. To demonstrate Eqn. (A3) a MATLAB routine was written to measure the mean ligament length of a randomly orientated

single length population, $P(l) = \delta(l - L)$, along a coordinate direction as a function of the number of struts, see Figure 64.

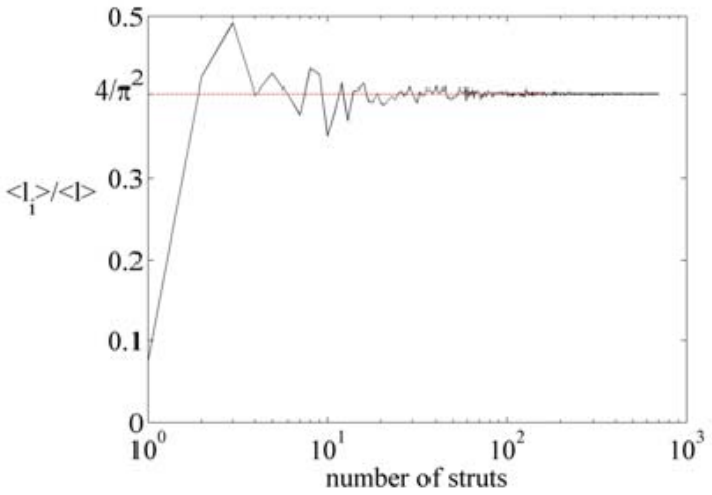

Figure 64: Mean strut length of a single length strut population along a coordinate axis as a function of the number of struts, $\langle l \rangle = L$

With approximately a 100 strut population the mean strut length relative to the mean length along a coordinate direction asymptotes to Eqn. A3. The mean strut length of a three dimensional randomly orientated strut population can thus be measured by sampling the mean orthogonal direction strut length from two dimensional images of the population.

APPENDIX B

MATLAB CODE OF SINGLE WAVELENGTH AND FLOW SPEED TOY MODEL

```
%The following MATLAB code generates the average time correlation function
%for particles moving along a sinusoid at a single tangential flow speed, y
%is the wave height direction.  VACF is the orthogonal velocity
%autocorrelation function % and sigma is the variance of y-displacements.

clear all
close all
N=400                           ; % # of discrete points along wave
L=1                             ; % wave length
H=0.375                         ; % wave height
x=(0:N-1)*L/N                   ;
y=H*sin(2*pi*x/L)               ;
V=2                             ; % tangential flow speed
a=2*pi/L                        ;
S=sqrt((H*a*cos(a.*x)).^2+1)    ;
So=trapz(x,S)                   ;
dS=So/N                         ;
dS=0:dS:So                      ;

for j=1:length(dS)
xe=.001                         ;
S2=0                                                    ;
while S2<dS(j)
xe=xe+.001                                              ;
xx=0:xe/100:xe                                          ;
SS=sqrt(1+(H*a*cos(xx*2*pi/L)).^2)                      ;
S2=trapz(xx,SS)                                         ;
end
xend(j)=xe                                              ;
end

yend=H*sin(2*pi*xend/L)                                 ;
    x  = xend                                           ;
    y  = yend                                           ;
    dt = 0.0005                                         ;
    vxo=sqrt(V^2./(1+((H*2*pi/L)*cos(2*pi*x/L)).^2))    ;
    vyo=vxo.*(H*2*pi/L).*cos(2*pi*x/L)                  ;
    vacfx(1)=sum(vxo.*vxo)                              ;
    vacfy(1)=sum(vyo.*vyo)                              ;

    xo = x                                              ;
    yo = y                                              ;
    sigma(1)=0                                          ;
    meanv=mean(vxo)                                     ;
    sigma(1)=0                                          ;
    tt(1)=0;
    t=0;
while meanv*t<1
        tt(end+1)=tt(end)+dt;
        t=tt(end);

 vx=sqrt(V^2./(1+((H*2*pi/L)*cos(2*pi*x/L)).^2))        ;
 vy=vx.*(H*2*pi/L).*cos(2*pi*x/L)                       ;
```

```
 dx = vx.*dt                                                ;
 dy = vy.*dt                                                ;
 x  = x+dx                                                  ;
 y  = y+dy                                                  ;
 vx=sqrt(V^2./(1+((H*2*pi/L)*cos(2*pi*x/L)).^2))            ;
 vy=vx.*(H*2*pi/L).*cos(2*pi*x/L)                           ;
vacfx(end+1)=sum(vxo.*vx)/vacfx(1)                          ;
vacfy(end+1)=sum(vyo.*vy)/vacfy(1)                          ;
sigma(end+1)=mean((y-yo).^2)                                ;
end
vacfx(1)=1                                                  ;
vacfy(1)=1                                                  ;

l=sqrt((xend(1:end-1)-xend(2:end)).^2+(yend(1:end-1)-yend(2:end)).^2);

figure, plot(tt.*meanv,sigma./tt)                           ;
figure, plot(tt.*meanv,sigma)                               ;
figure, plot(tt.*meanv,vacfy)                               ;
```